Design Optimization of Variable-Stiffness Composite Panels under Thermomechanical Loads

H.J. van Loo

Delft University of Technology

TU Delft

AIRBUS

Design Optimization of Variable-Stiffness Composite Panels under Thermomechanical Loads

Master Thesis Report

by

H.J. van Loo

To obtain the degree of Master of Science
at the Delft University of Technology,
to be defended on Wednesday June 21, 2017 at 10:00 AM.

Student Name:	Hendrik Jan van Loo	
Student Number:	4052234	
Supervisors:	Dr. MSc. J. Fatemi,	TU Delft and Airbus Defence and Space
	Dr. ir. D.M.J. Peeters,	University of Limerick (Former TU Delft)
	Dr. MSc. M.M. Abdalla,	American University of Cairo
Assessment Committee:	Dr. S.R. Turteltaub	TU Delft
	Dr. MSc. J. Fatemi,	TU Delft and Airbus Defence and Space
	Dr. ir. O.K. Bergsam	TU Delft
	Dr. ir. D.M.J. Peeters,	University of Limerick

This thesis is confidential and cannot be made public until June 21, 2022.

After the embargo expires an electronic version of this thesis is available at:
`http://repository.tudelft.nl`.

Acknowledgements

This report presents the research and work that is performed to complete the master track Aerospace Structures and Materials at TU Delft to obtain the degree of Master of Science.

I would like to thank everybody that contributed to this work. Firstly I would like to thank Javad Fatemi, despite his full agenda he found time to supervise and lead the project. He formed the bridge with Airbus Defence and Space and made the project more exciting by providing an industrial level application to work with. Furthermore I would like to thank Mostafa Abdalla for his supervision, especially his knowledge during the analytical phase was valuable. I would also like to thank the members of the assessment committee, Sergio Turteltaub and Otto Bergsma, for evaluating this work.

Special thanks goes to Daniel Peeters, he was always available to provide invaluable information about the optimization framework. After he obtained his doctorate and left to Ireland he was still concerned with the project and available to answer questions that arose during the conclusion of the project. His continuous supervision and proof reading of this report are really appreciated.

Above all I would like to thank my parents, family and girlfriend for their support through all these years. With this thesis my studies in Delft comes to a conclusion. At last I would like to thank my former housemates from the Van Embdenstraat, they made my stay in Delft one with great memories.

Rick van Loo
June 13, 2017

Summary

Over the last few decades the aerospace industry adopted carbon fiber reinforced polymers for lightweight design of primary structures. Striving to improve structural efficiency the aerospace industry shows increasing interest in variable-stiffness composite laminates. Advanced fiber placement is a hybrid manufacturing technique that offers the flexibility of both filament winding and automated tape laying. With the development of this novel system curved tows can be placed and a spatially variable-stiffness laminate can be designed with continuous changing stiffness from point to point. The capability to produce variable-stiffness composites is very promising and allows for sophisticated designs.

The increased design freedom to tailor a structure by in-plane stiffness variation leads to a challenging design optimization problem. A multi-step framework is developed by the aerospace structures and materials department at TU Delft to optimize variable-stiffness laminates. First the stiffness variation is optimized in lamination parameter space, a parameterization that yields beneficial optimization properties. After the optimal lamination parameters are obtained the corresponding fiber angle distribution is retrieved. This retrieval step proves to be a challenging exercise, especially when manufacturing constraints are included. An extension to the framework includes sub-approximations in fiber angle space to assess retrieval. By additional optimization iterations in fiber angle space a true optimal fiber angle distribution is obtained.

Variable-stiffness laminate design can potentially save weight of structural components if the increment in tailoring freedom leads to a significant performance boost. Based on this premise Airbus Defence and Space wants to investigate how such design could improve the structural performance of an engine thrust frame, a structural application that transfers the thrust loads from the rocket engine to the rest of the launch system. The engine thrust frame is subject to cryogenic thermal loads, something not incorporated in the available optimization framework. The goal of this work is to add thermal loads to the laminate analysis routine and to adjust the optimization routine to incorporate thermal influences.

The optimization routine is based on sequential local approximations, these are re-evaluated to include thermal influences. The approximations are gradient based and the thermomechanical governing equations are used to perform sensitivity analyses to build the updated local approximations. For the strength and buckling responses the thermomechanical sensitivities are derived using an adjoint displacement approach. Implementation of the thermal analysis is verified by a design study of a simply supported rectangular plate under uniform end shortening subject to thermomechanical loads. Results from the updated optimization routine show similar design patterns as the reference papers. A stiffness variation that distributes loads towards the restrained edges and away from the prone to buckling center area proved to be optimal. This design study shows that variable-stiffness laminates have the design freedom to effectively optimize local properties and global load distribution.

With the thermomechanical optimization framework in place the engine thrust frame is modeled. Conceptual design optimization of the variable-stiffness laminate of the engine thrust frame under thermomechanical loads is performed to increase buckling resistance. Three models are studied to research the thermomechanical effects, namely a constant thickness, tapered thickness and stiffened tapered thickness design. The first two models are axisymmetric nullifying load redistribution to improve buckling performance. Gains of 10-20% in buckling performance are established by adjusting local resistance to the critical buckling modes.

The stiffened design has stiffened areas and load can be redistributed in circumferential direction, this adds more freedom to tailor the design. The optimal variable-stiffness laminate distributes compressive stresses towards the stiffened areas for the pure mechanical load case. A mismatch in the coefficient of thermal expansion is used by the optimal variable-stiffness design for the thermomechanical load case. The stiffened areas contract less than the bay regions, thus a stabilizing tensile stress is induced in the prone to buckling bay regions. For both design cases improvements around 45% are obtained. Although this is significant it should be interpreted with care. Multiple simplifications regarding geometry and loads are applied and the conceptual design study is bounded to research the potential of a variable-stiffness laminate design for the engine thrust frame.

Contents

List of Figures

List of Tables

Nomenclature

Latin Symbols

A	Membrane stiffness matrix	N/m
A_e	Element area	m^2
B	bending-stretching coupling stiffness matrix	N
B	Strain displacement matrix	m^{-1}
C	Compliance	Nm
D	Bending stiffness matrix	Nm
E	Axial stiffness	Pa
F	Force	N
G	Shear stiffness	Pa
H	Hessian	-
K	Thermal material invariants	Pa
K_m	Material stiffness matrix	Pa
K_g	Geometric stiffness matrix	Pa
L	Linking matrices	-
L	Lagrangian	-
L_c	Falk's dual Lagrangian	-
M	Moment resultant	N
M^{Th}	Equivalent thermal moment	N
N	Stress resultant	N/m
N^{Th}	Equivalent thermal load	N/m
Q	Stiffness terms	Pa
T	Temperature	K
T_0	Fiber angle at the plate center	deg
T_1	Fiber angle at the plate edge	deg
U	Material invariants	Pa
$V^{A,B,D}$	Lamination parameters	-
a	Buckling mode shape	-
a	Panel length	m
d	Half panel length	m
f	Failure index	-
f	Function value	-
f_A	Approximation function	-
f_D	Damping function	-
f_C	Convex approximation	-
g	Constraint	-
g	Gradient	-
h	Laminate thickness	m
r	Response function	-
r_{lim}	Minimum steering radius	m
t	Ply thickness	m
u	Displacement vector	m
v	Adjoint displacement vector	m
w	Weight value	-
x	Design variable	-
z	Through-thickness coordinate	m

Greek Symbols

Γ	Material invariant matrices	Pa
Ω	Domain	-
α	Coefficient of thermal expansion	K^{-1}
γ	Shear strain	-
γ	Damping bounds	-
δ	Conservative hybrid selecting parameter	-
ε	Normal strain	-
ζ	Damping factor	-
η^m	Thermal membrane sensitivity	m/N
θ	Ply and fiber angle orientation	deg
κ	Curvature	m^{-1}
λ	Load multiplier	-
μ	Dual variables	-
ξ	Steering limit	m^{-1}
ρ	Density	kg/m^3
ρ	Ply density	-
σ	Normal stress	Pa
τ	Shear stress	Pa
ν	Poisson's ratio	-
ϕ	Direction of linear fiber angle variation	deg
ϕ^m	Reciprocal membrane sensitivity	N/m
ϕ^b	Reciprocal bending sensitivity	Nm
ψ	Streamline	-
ψ^m	Linear membrane sensitivity	m/N
ψ^b	Linear bending sensitivity	$(Nm)^{-1}$

Abbreviations

AFP	Automated Fiber Placement
ATL	Automated Tape Laying
CCR	Cut Clamp and Restart
CCSA	Conservative Convex Separable Approximation
CFRP	Carbon Fiber Reinforced Polymer
CTE	Coefficient of Thermal Expansion
DOF	Degrees of Freedom
ETF	Engine Thrust Frame
FEA	Finite element analysis
GFRP	Glass Fiber Reinforced Polymer
LP	Lamination Parameters
OLGA	Optimization of Laminates using Genetic Algorithm
QI	Quasi-isotropic
STAGS	Structural Analysis of General Shells
VS	Variable-Stiffness

1

Introduction

Nowadays carbon fiber reinforced polymers are an integral part of many aerospace applications. They are often used for lightweight design of primary structures. For a long time only conventional laminates were used, but with increasing knowledge and experience more and more non-conventional laminates are investigated and applied. Striving to improve structural efficiency the aerospace industry developed the advanced fiber placement production technique. With this technique it is possible to place curvilinear tows, enabling the production of variable-stiffness laminates. The design of such laminates is a challenge and over the last decade an optimization framework is developed by the aerospace structures and materials department at TU Delft. Airbus Defence and Space proposed to use this framework to create a conceptual design of a variable-stiffness engine thrust frame. Due to the design and thermomechanical load conditions of the engine thrust frame the optimization framework needs additional functionalities before it can be used.

This chapter will start with a short motivation why lightweight design is so important in the aerospace industry in section 1.1. This is followed by a brief overview why carbon fiber reinforced polymers are one of the main load bearing materials in section 1.2. Section 1.3 introduces variable-stiffness laminates and section 1.4 will state the project objective. At last an overview of the report structure is provided in section 1.5.

1.1. Motivation for Lightweight Design

According to the U.S. Department of Transportation fuel consumption accounted for 28.1% of operative cost for American airliners in 2014 [1]. A way to reduce fuel consumption and cost is to strive for lightweight design. By vertical force equilibrium lighter aircraft require less lift to maintain altitude. A reduction in lift reduces wing surface and this lowers the loads imposed on the structure, most specifically the root bending moment. This will lead to weight saving of structural components for well designed aircraft. Furthermore the corresponding reduced drag requires less thrust by horizontal force equilibrium. This relates to higher fuel efficiency, that is more distance can be traveled per amount of fuel. The weight saving of structural components and fuel lead to another weight saving iteration. This is known as the 'snowball effect' and emphasizes the importance of lightweight driven design for aircraft. Lee et al estimated that a reduction of 1% of the gross weight of an aircraft reduces fuel consumption by approximately 0.75% [2].

Spacecraft is, similar to aircraft design, also driven by weight. For launchers evaluating the well-known Tsiolkovsky rocket equation clearly shows that a high mass ratio is advantageous in relation to the delta-V budget. To launch a lighter rocket less propellant is required and a snowball effect similar to aircraft design can be initiated to reduce the space bus size to account for the reduced propellant requirements. Alternatively a higher payload fraction could be applied.

1.2. The Road to Carbon Fiber Reinforced Polymers

Many engineering solutions are copied or derived from nature. Looking for load bearing structures in nature our bones and skeleton comes to mind. Cortical bone tissue is a fiber-composite where collagen protein fibers are dispersed in a mineral apatite matrix. The collagen fibrils add strenght, fracture thoughness and elasticity to the bones. Due to the fibrous nature the material properties are anisotropic and our body uses this to improve the mechanical properties of the bone based on the load conditions. For regions supporting tensile loads the fiber orientations grow in longitudinal direction and compressive loading results in transversely oriented fibrils [3].

Similarly wood is also a fiber-composite. Wood is made from hollow elongated organic cells and the load bearing capabilities stem from the cell wall. The walls are made from cellulose polymer microfibrils in a lignin matrix. Wood yields anisotropic material properties, since the fiber orientation and cell elongation are primarily in the load direction [4].

In the beginning of the 20th century a material with low density and relatively high stiffness and strength properties was sought for by aircraft pioneers. Due to the small dimensions and low speeds of early aircraft wood and fabrics were perfect and cheap solutions to build the frame and wings respectively. The anisotropic properties of wood were used to its advantage in wired braced frameworks. The maturing of aircraft design came with an increment in weight and speed and the specific properties of wood could not meet the new requirements. During the 30s the industry started to implement aluminum alloys that showed superior specific properties. Different alloys have been developed and the aerospace industry has been dominated by isotropic material design to the end of the 20th century.

Table 1.1: General material properties of an aluminum alloy, GFRP and CFRP [5].

Property	Unit	Aluminum	GFRP	CFRP
Density	kg/m^3	2700	1800	1600
Stiffness	GPa	69	39	181
Ultimate Tensile Strength	MPa	276	1062	150

The use of anisotropic materials by load bearing structures in nature shows that isotropic material design is not the most efficient. With increasing flight speeds and the start of the space age even better material properties were demanded. Anisotropic glass fiber reinforced polymers (GFRP) have been available since the 30s and showed increased design flexibility and great strength, but the accompanied low stiffness made it not suitable for mass adoption. A better fiber bed was researched and in the 50s graphite fibers were applied with excellent properties. It took another decade before high performance continuous carbon fiber reinforced polymers (CFRP) were manufactured using rayon as the starting compound. General material properties of aluminum, GFRP and CFRP are given in Table 1.1. Due to the better material efficiency of CFRP aluminum alloys are slowly being replaced in the aerospace industry to increase the structural efficiency of air- and spacecraft, this trend is supported by Figure 1.1.

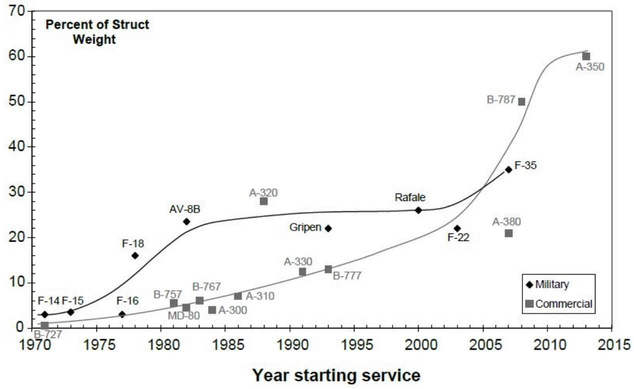

Figure 1.1: Implementation of composite structures in aircraft is illustrated by an incremental trend. From Kassapoglou (2010) [6].

1.3. Variable-Stiffness Composite Laminates

A CFRP laminate is build from multiple plies that are stacked together, this is illustrated in Figure 1.2. Initially only conventional ply orientations of 0, ±45 and 90 degrees were used due to manufacturing constraints. A conventional quasi-isotropic laminate is often used as a reference design. Even though quasi-isotropic laminates already benefit over aluminum by a higher specific strength and stiffness, it can be further improved by tailoring the laminate design to take advantage of the anisotropic ply properties and to increase material efficiency. Tailored correctly this results in an increased structural performance, allowing a capable design with less material and reduced weight.

With the development of automated tape laying (ATL) machinery manufacturers show more interest in non-conventional laminate production. A wider range of fiber angle orientations can be considered for laminate design and a larger design space is addressed. To further increase the design space the aerospace industry shows interest in variable-stiffness laminate design.

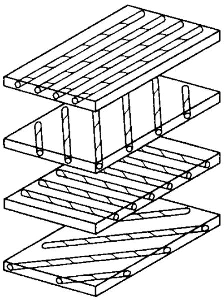

Figure 1.2: Laminate constructed from multiple plies with different orientations. From Jones (1980) [7].

Varying the laminate thickness is the most straight-forward mean to vary the stiffness of a laminate and to further tailor the design. Local thickening by additional plies can alter the stiffness at these regions, the same holds for ply drops. Another way to design a variable-stiffness laminate is by intra-ply stiffness variation.

A feasible way to manufacture intra-ply variable-stiffness for conventional laminate design is to create discrete patches with independent fiber orientations, this is illustrated in Figure 1.3 (left). The result is a discrete variable-stiffness laminate. Taking the limit of this approach with infinitesimal patches results in continuous variable fiber paths, also illustrated in Figure 1.3 (right). With this method a spatially variable-stiffness laminate can be designed with continuous changing stiffness from point to point [8, 9]. This approach holds more design freedom and avoids stress concentrations between patches.

Production techniques were not capable to produce such designs for a long time. Unlike filament winding that can change the tow orientation on the go, ATL is limited to straight fiber paths. Advanced Fiber Placement (AFP) is a hybrid that offers the flexibility of both filament winding and ATL. AFP is a relatively new production technique with only 20 operational machines in 1999 [10]. With the development of this novel system curvilinear fiber paths can be placed, thus it is feasible to manufacture intra-ply variable stiffness panels nowadays [11–13]. Potentially this can save weight of structural components if the increment in tailoring freedom leads to a significant performance boost. Theoretically it is possible to reduce stress concentrations by designing the fiber paths in a way that stresses are distributed to less loaded areas [14–17].

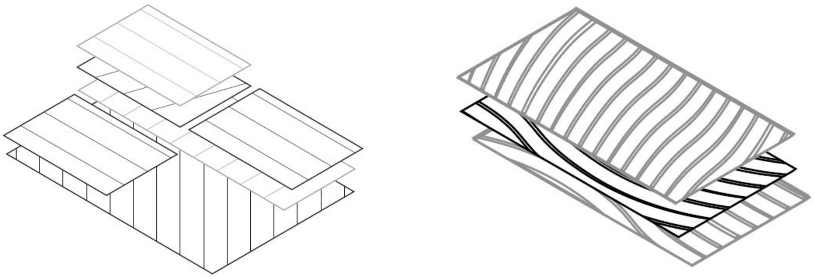

Figure 1.3: Discrete patches of material (left) and continuous variable fiber paths (right). Two ways to create variable-stiffness laminates. From IJsselmuiden (2011) [18].

1.4. Research Objective

The capability to produce variable-stiffness composites is very promising and allows for sophisticated designs. Airbus Defence and Space is interested in variable-stiffness laminates and wants to investigate how such design could improve the structural performance of an engine thrust frame (ETF). An optimization framework is developed by the aerospace structures and materials department at TU Delft to optimize variable-stiffness laminates. The engine thrust frame is subject to thermal loads, something not incorporated in the available optimization framework. Before a design study can be executed thermal loads should be implemented in the laminate analysis routine and the optimization framework. Therefore the research is split into two research objectives:

1. Implementation of thermal loads in the laminate analysis routine and incorporation of the corresponding influences in the optimization framework.
2. Modeling and conceptual design optimization of the variable-stiffness laminate of the engine thrust frame under thermomechanical loads.

The first objective is to include thermal analysis in the existing framework. The existing framework also includes thickness optimization. Ply densities will be included in the thermal laminate and optimization analysis to prepare the framework for thickness optimization in future work. However, thickness optimization is outside the research scope and will not be used for the design application in this project. After the existing framework is updated to work with thermomechanical load conditions the newly obtained routine will be verified.

Only then the conceptual design optimization of the ETF is executed. The design problem is split in three design cases and complexity is added to the model by every design iteration. First a constant thickness design is considered, followed by a tapered thickness design. Finally stiffeners will be added to model a stiffened tapered design.

1.5. Report Structure

First a state-of-the-art background is given in chapter 2. This includes a brief explanation of the AFP production technique and its characteristics, followed by a historic overview of variable-stiffness optimization based on different parameterizations. Composite laminate analysis is treated in chapter 3, including thermal analysis. The implementation in the linear finite element and buckling analysis is also discussed. The optimization framework is discussed in chapter 4 and the influence of thermal loads is explained. After the framework is updated the optimization routine is verified in chapter 5. The conceptual design results of the ETF are thoroughly discussed in chapter 6. After the results are discussed a conclusion of the project is drawn in chapter 7 and finally recommendations for future work are given in chapter 8.

2

State-of-the-Art Background

Relevant background information about variable-stiffness panels will be discussed in this chapter. The Automated Fiber Placement (AFP) machine will be addressed in section 2.1 to describe its working principle and how the characteristics influence fiber steering. Over the past two decades many studies have been performed to research variable-stiffness panels by fiber steering. Different parameterizations are used to describe the design. The optimization problem is influenced by the chosen parameterization, therefore the different parameterizations will be discussed in section 2.2.

2.1. The Automated Fiber Placement Machine

Nowadays most companies involved with composite manufacturing adapted Automated Fiber Placement technologies. Although all machines will be different they are all based on the same working principles [19]. All machines have a creel; a storage chamber to store tows or slittape on bobbins. The creel has controlled conditions and come with tension regulated bobbin unwinding systems. A tow feeding system feeds the tows to the placement head with regulated tension. A schematic of a general placement head is given in Figure 2.1.

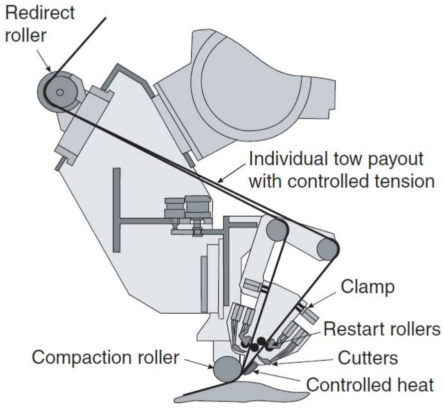

Figure 2.1: A schematic of a placement head for automated fiber placement machines. From Evans (2001) [19], adjusted by Lopes *et al* (2008) [20].

The most notorious improvements during its maturing are the switch from soaked to prepreg systems and development of cut, clamp and restart (CCR) technology. The former improves the quality of the resin fiber bed and the latter gives the possibility to cut and restart tows on the fly [10]. The head is capable to feed individual tows with controlled tension by the tenstion regulated unwinding system. This differentail pay out is one of the key features and important to allow different tows to conform the shape of the mold individually. The CCR technique allows to control the width of the fiber band by adjusting the amount of tows that are placed. After the CCR system the tows are flattened and fed as a collimated fiber band which will be heated before the compaction rollers presses the band firmly on the mold and previous layers [19]. Depending on the type of polymer the heating is normally done by infra-red or laser heating devices for thermosets and thermoplastics respectively [21]. Multi-axial range of motion allows the head to follow complex band paths which are given as an input to the placement machine.

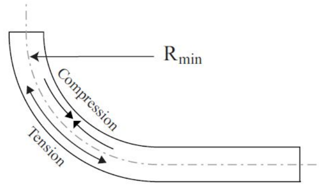

Figure 2.2: Curved tows have compression on the inside and tension on the outside. This limits the minimum curvature of a fiber to avoid local buckling. From IJsselmuiden (2011) [18].

2.1.1. Characteristics

The fiber placement technique has characteristics directly related to the design of composite structures. It is important to know what these limitations are since they influence the feasible design region. The most important characteristics are listed:

- **Curvature:** This is a geometric constraint on the design by the tows rather than the machine itself. A tow is curved by in-plane bending and local compression and tension are present at the curve, this is illustrated in Figure 2.2. Alternatively in-plane angle variation by shearing is researched [22].

  The smaller the turn radius the higher the compression becomes and local buckling can occur [19, 23, 24]. Although it might be possible for the placement head to turn with a small radius this could cause excessive local buckling of the tows which reduces the local load bearing capabilities of the structure. A minimum curvature constraint is introduced on the design to avoid this. The minimum curvature is affected by the tow size, smaller tow width can follow smaller radii but will slow down the manufacturing process. For an 3.2mm tow or slit tape a minimum turn radius of 625mm is suggested in literature [19, 24].

- **Minimum cut length:** This is a geometric constraint by the machine. With the CCR technology fiber placement machines can cut and place tows on the go. The minimum cut length determines the shortest tow the machine is able to place. The minimum cut length depends on the design of the machine and is given by the distance between the cutting mechanism and the compaction roller [19]. In the design this limitation has to be accounted for that every tow in the design can be placed. If tow lengths smaller than the minimum cut length are present in the design the machine is not able to place and a resin rich pocket without fiber content is produced instead.

- **Mold size and shape:** This is a geometric constraint by the machine. The mold and placement machine should not collide and this influences suitable mold sizes and shapes. This is important to consider for concave designs since chances of collision are inherently more present. Fiber bridging should be considered if the turn radius of the mold becomes steep [19]. Tackiness helps to avoid fiber bridging. Since Thermoplastic resin systems have less tackiness it is essential to lower the tension forces of the bobbins to avoid fiber bridging [25].

- **Deposition Rate:** This is a capacity and productivity constraint by the machine. Deposite rate depends on the fiber band size and the speed of the placement head. The band size is determined by the amount of tows and the tow width. More and larger tows results in a larger surface area covered by one iteration. However this limits steering and consequently diminishes the advantage of AFP.

2.1.2. Future Development: In-situ Consolidation

Traditionally epoxy is used in the aerospace industry, however a shift is noticable towards thermoplastic polymers due to their better toughness, fracture resistance and low cost production cycles [25, 26]. Curing and consolidation takes place in an autoclave, but the usage of autoclaves results in costly and slow production cycles and is considered to be a bottleneck for AFP [25]. New in the field are the new generation AFP machines that are able to use thermoplastic polymers with similar production speeds as thermoset polymers [21].

For a long time in-situ consolidation with AFP was thought to be unfeasible. This idea was based on classical reptation theory introduced by Gennes. One of the assumptions in raptation theory is that it takes time to establish proper diffusion of polymer chains. In-situ consolidation comes with quick application of pressure causing shear thinning. This enhances diffusing significantly, thereby ultrasonic vibrations can be used to further improve diffusion [25]. Another aspect of reptation theory is that pressure is important to ensure intimate contact. However, the influence of pressure on bond strength is proven to be limited [27], although pressure is still important to reduce the inter and intra-laminate void content [28].

Development of diode laser heating devices result in very short and effective heating times with a narrow affected heating zone [21]. Polymer degradation due to repeatedly high temperature heating by in-situ consolidation is overstated due to this short heating time and small heat affected zone [25].

Although thermoplastic in-situ consolidation AFP machines are commercially available the quality is still sub-par compared to autoclave post-processing of both thermoset and thermoplastic composite structures [25]. Accudyne systems, NASA, and the university of Delaware performed a series of studies to research the most important parameters to get in-situ consolidation to a next level [29–31]. The void content after in-situ consolidation was too high to compete with autoclave quality. The supplied tows need better surface roughness and resin rich tow surfaces to reduce interlaminar void content to create full layer to layer weld strength. A new experimental placement grade tow shows improvement in strength of 7% compared to commercial available tows and slittape. This is promising and could close the gap with autoclave processes.

2.1.3. Parallel and Shifted Fiber Bands

The main design decision regarding manufacturing of variable-stiffness laminates is how the fiber courses are given as input to the placement machine. For varying fiber paths in one spatial direction the first technique is to apply parallel courses [32]. Adjacent courses follow the trajectory of the reference course, this is illustrated in Figure 2.3 (left). The advantage is that adjacent fiber bands are perfectly aligned and no gaps or overlaps are present. The disadvantage is that the courses deviate from the optimum reference course. Furthermore the steering constraints can be voided.

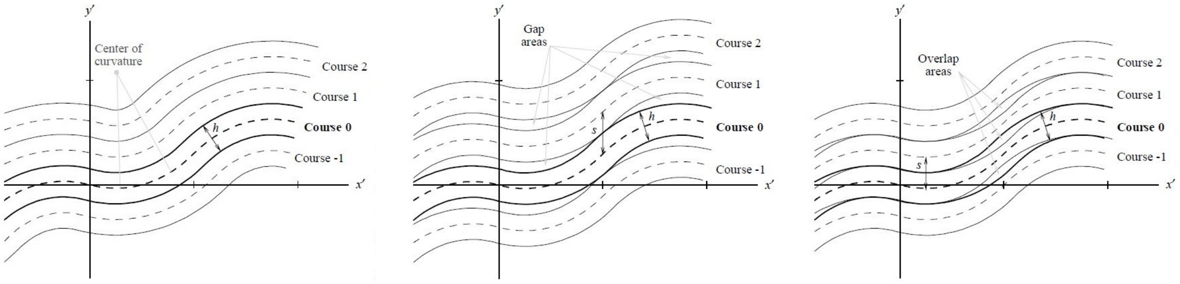

Figure 2.3: Parallel fiber courses (left). Shifted fiber courses with gaps (middle). Shifted fiber courses with overlap (right). From Gurdal and Tatting (2006) [32].

Another technique is to shift the reference course, illustrated in Figure 2.3 (middle). In contrast to the parallel technique the curvatures of the optimum reference path are contained, however resin filled gaps are now present. These gaps have no fiber content and reduce the mechanical properties of the structure. Alternatively adjacent courses can overlap to elminate resin filled gaps, this is given in Figure 2.3 (right). Although this yields favorable properties more material is added by local thickening and the weight of the structure increases. To prevent thickening accumulation and evenly distribute the properties over the panel ply staggering is applied [12].

Tow-Drop and Overlap Techniques

The AFP machine comes with differential control of tows and the control of the bandwidth by the CCR technique. It is therefore possible to prevent overlap of shifted fiber bands by dropping tows one by one at the boundary of adjacent band courses. This is referred to as the tow-drop method and is illustrated in Figure 2.4 (left). As a reference the tow courses for the overlap method without tow-drops are given in Figure 2.4 (right).

With the tow-drop method it is important to indicate the coverage of the tows [33]. The percentage of coverage indicates how much the tows overlap previous placed fiber courses at the boundary curve before they

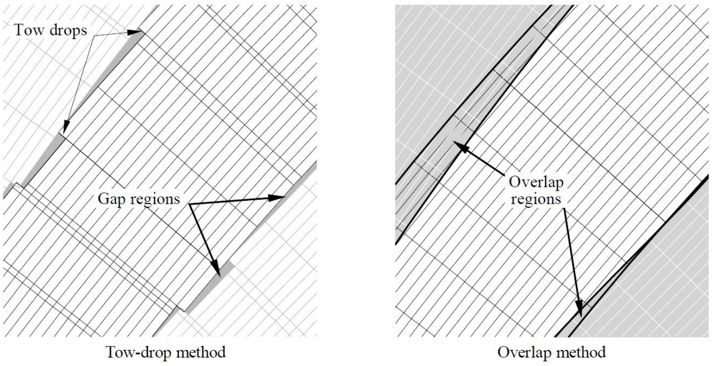

Figure 2.4: Manufacturing with tow-drops to prevent overlap (left) and without tow-drops with full overlap and local thickening (rigth). From Gurdal and Tatting (2005) [33].

are cut. A coverage of 0% indicates that the tow is cut once the leading edge reaches the boundary curve. The result is that there is zero overlap and small resin rich gaps are present. A coverage of 100% indicates cutting once the trailing edge reaches the boundary curve. The result is full coverage and no gaps but small overlaps are present. The coverage is illustrated in Figure 2.5 for 0, 50 and 100% coverage. Note that there is some local thickening of tow-drop with 100% coverage, but limited compared to a fully overlap manufacturing method where tows are not dropped.

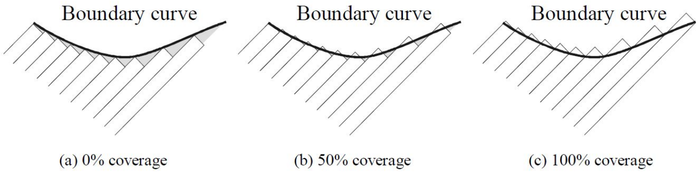

(a) 0% coverage (b) 50% coverage (c) 100% coverage

Figure 2.5: Coverage percentage for the tow-drop production technique. From Gurdal and Tatting (2005) [33].

Croft *et al* performed coupon and laminate tests to show the influence of gap and overlap defects on the ultimate strength [34]. Overlap placement show minor improvements in tensile and compression strength, whereas tow-drop techniques show improvements in shear strength.

2.2. History and Parameterization of Variable-Stiffness Laminates

Intra-ply stiffness variation can be established by spatially varying the material properties within a ply. There are multiple ways to optimize a laminate with spatially varying fiber orientations. Suitable optimization alghorithms to design variable-stiffness laminates depend on the choice of parameterization. Three parameterization methods can be distinguished, namely discrete stiffness represenation, functional representation of fiber paths and the direct stiffness approach [18].

2.2.1. Discrete Stiffness Representation

This parameterization approach uses design variables related to the stacking sequence, that is the fiber orientation of each ply or subsets of plies. This is directly related to the stiffness properties of the laminate by classical laminate plate theory. This approach is intuitive, since it is a bottom-up design process commonly applied to design traditional composite panels.

One of the first propositions to design variable-stiffness panels is based on discrete stiffness representation. In 1989 Hyer and Charette researched curved fibers around a center hole to improve the mechanical properties of a panel under tensile loads [8]. To obtain a spatially varying fiber path the structure is discretized into a mesh grid. For all elements the fiber angles were aligned with the local principle stress directions and improved in-plane behavior was obtained. In a follow-up study Hyer and Lee modelled the same quarter plate and used a gradient search optimization routine to maximise the buckling load for uniform end shortening [9]. To limit the amount of design variables every element is represented by a $(\pm 45|\theta_6)_s$ stacking sequence. A radial mesh of 6 elements and a mesh that refines each radial element in 3 elements are modeled. The optimal fiber orientations are given in Figure 2.6. Compared to a quasi-isotropic design the buckling resistance was improved by a factor of 1.85 and 2.96 for both mesh grids respectively. Nagendra *et al* implemented constraints to ensure continuity and smoothness of the fiber angle orientations. The buckling improvement factor was reduced to 1.72 for the 6 element mesh grid [35].

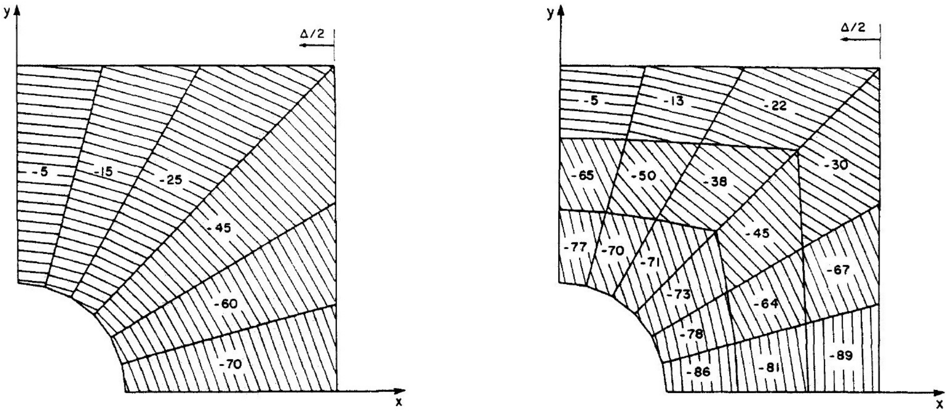

Figure 2.6: Discretization of a quarter plate into 6 radial elements (left) and 18 elements (right). For the given fiber orientations a buckling resistance improvement of 1.85 and 2.96 compared to an isotropic design was found respectively. From Hyer and Lee (1991) [9].

In 1991 Pedersen applied optimallity criteria based on strain energy to optimize for both thickness and fiber orientations [36]. Thickness optimization results in a uniform strain energy distribtution and orientation optimization improves the stiffness by strain minimization. In 2004 the work was extended to include manufacturing considerations into the thickness optimization. With a black and white formulation plies are either fully present or not at all [37].

In 2003 Setoodeh and Gurdal optimized a plate with a center hole under tension and shear loading by Cellular Automata [38]. To get a smoother variation of fiber orientations the design variables are defined at the nodes instead of the elements. To get the stiffness at the elements the nodal results are simply averaged. This approach is used before in topology optimization using cellular automata to avoid checkerboard results [39]. Pattern matching is applied is applied to generate smoother designs. Improvements of 50% and 72% in compliance was obtained for shear and tensile loads respectively. In a follow-up study the previous study was extended to include topology optimization [40].

Defining the stacking sequence at discretized locations the number of design variables increase rapidly with increasing mesh densities. To ensure a manageable design space the degree of discretization is limited. Structural responses are related to the stiffness matrices of the laminate. The stiffness properties have a non-linear relation with the fiber angle orientation. Therefore most structural responses behave in a non-convex way in the fiber angle design space and the design result can be a local optimum [9, 41, 42].

2.2.2. Functional Representation of Fiber Paths

The disadvantages encountered with discrete stiffness representations led to functional representation of fiber paths. Parameterization is related to the fiber paths. At discrete points the stacking sequence can be derived as a function of the fiber paths and the stiffness matrix can be computed.

Linearly Varying Fiber Orientations

Inspired by the idea of variable-stiffness laminates Gurdal and Olmedo were the first to introduce a parameterization based on a curvilinear fiber paths in 1992 [14, 15]. A simple parameterization that only linearly varies the orientation along one spatial direction was introduced due to limitations of processing techniques and in an effort to use realistic manufacturable fiber paths. The general form of the spatially varying fiber angle is given by Equation 2.1 and illustrated in Figure 2.7. Corresponding fiber paths are denoted as $<\phi,(T_0 \mid T_1)>$, where ϕ indicates the direction of linear variation and T_0 and T_1 represent the fiber orientations at the center and edges of the panel respectively.

In the same year Gurdal and Olmedo evaluated the buckling response of variable-stiffness panels with curvilinear fiber paths [16, 17]. For a simply supported rectangular plate under uniform end shortening with

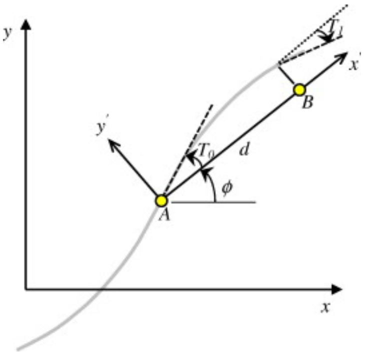

Figure 2.7: Fiber path by linearly varying the fiber orientation. The fiber paths is defined by parameters ϕ, T_0 and T_1. From Gurdal et al (2007) [16].

straight transverse edges it is shown that load is distributed from the middle towards the edges. The edges are more restrained from buckling by the boundary conditions than the middle region, hence the critical buckling load is increased. This study proves that redistributing load by global design can be more beneficial than local optimization for bending stiffness. Improvements up to 80% over straight fiber laminates were found for panels without adding weight. This effect increases for larger aspect ratios.

$$\theta\left(x'\right) = \phi + \frac{(T_1 - T_0)}{d} x' + T_0 \tag{2.1}$$

In the previous studies manufacturing constraints on curvature imposed by the tow placement machines were not included. However, this introduced parameterization allows for easy implementation of manufacturing constraints and consequently this was done by Waldhart et al [43]. Results for the same buckling application now only yield 44% improvement over the optimal straight fiber design. Thereby an updated formulation of the fiber paths allows for truly parallel fiber paths within a ply, causing the stiffness also to vary in y-direction for $< 0, (T_0|T_1) >$. The parallel fiber paths do not distribute the stresses to the transverse edges as effective as the shifted fiber paths do, therefore reducing the critical buckling load.

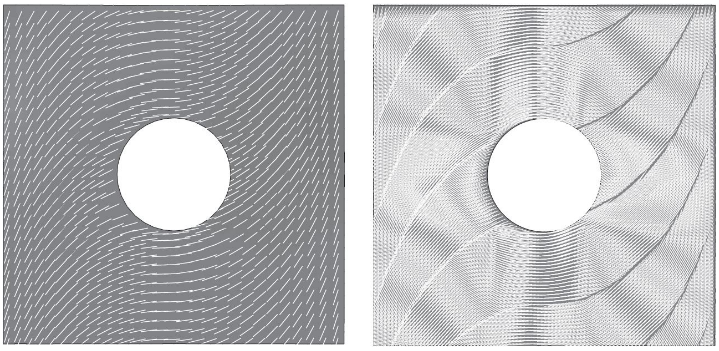

Figure 2.8: Ideal design (left) vs a design with tow drop and staggering corrections (right) for $< 0, (0|80) >$. From Lopes *et al* (2010) [44]

In 2007 Lopes *et al* studied the buckling and first ply failure of panels with linearly varying fiber orientations by finite element analysis (FEA) [20]. They used the LaRC0# failure criteria developed by Langley Research Center for fiber reinforced laminates. This failure criterion is able to assess different failure modes and is suitable for computational analysis [45]. The loads corresponding to first ply failure increased by 34% and 25% for tow-drop and overlap tow placement respectively. In a follow-up study a rectangular plate with a center hole was optimized for first ply failure [44]. An improvement of 20% for an optimal variable-stiffness design was obtained over the optimal straight fiber baseline panel. Applying manufacturing corrections to account for tow-drop and staggering yields and improvement of roughly 13%. The differences between the ideal and manufacturable design are illustrated in Figure 2.8.

Blom *et al* investigated the influence of the tow-drop technique on the strength and stiffness of variable-stiffness panels [46]. By FEA and the LaRC0# failure criteria the influence of tow-drops, staggering, tow-width and laminate thickness are investigated. In most cases damage is initiated at tow-drop areas. Reducing the tow width to reduce gaps and using a staggered design improves the strength.

Experimental Results

Wu *et al* manufactured two panels based on the optimal design found by Waldhard with tow-drop and overlap techniques with the Viper Fiber Placement System from Cincinnati Machines [11]. The result of both techniques are given in Figure 2.9, note that the overlap regions caused a weight increment of 20%. For uniform end shortening an excellent correlation between experimental data and analysis was found for linear pre-buckling. Larger differences were found for non-linear post-buckling. Including thermal pre-stresses caused by curing in the analysis improved the buckling and failure prediction. Compared to a conventional baseline design of $\pm 45^o$ an improvement of 28% was measured for the failure load of a panel with overlaps and 8% for a panel with ply drops. These values are corrected for weight differences, however local thickening stemming from the overlap technique functions as a stiffened design which improves the load carrying capability of the panel.

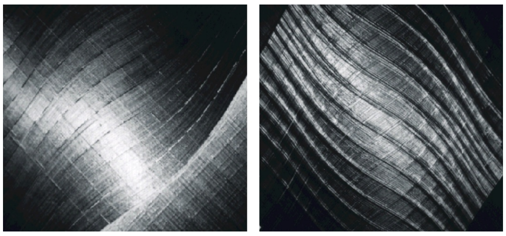

Figure 2.9: Panels manufactured with the tow-drop (left) and overlap technique (right). From Gurdal and Tatting (2002) [47]

In two follow-up studies the commercial FEA routine STAGS (Structural Analysis of General Shells) from Lockheed Martin and the OLGA (Optimization of Laminates using Genetic Algorithm) optimization routine from ADOPTECH were integrated [32, 47]. The obtained automated analysis routine is used to determine the optimal linear variation of fiber orientations to increase the buckling resistance of a plate with a center hole under compressive and shear loads. Jegley *et al* conducted experiments and reasonable agreement with the numerical results was found [12, 13]. Improvements of 10% and 30% were predicted and improvements of 10% and 90% were found by the experiments for panels with the tow-drop and overlap techniques respectively. Thermal pre-stresses are not included in the numerical analysis and could be a possible cause for the deviation.

Weaver *et al* researched post-buckling effects [48]. Experiments concluded that for an optimized variable-stiffness panel the post-buckling stiffness was still 92% of the pre-buckling stiffness, whereas for a quasi-isotropic baseline design the post-buckling stiffness dropped to 72%. Additionally the critical buckling load was 30% higher.

Conical and Cylindrical Surfaces

Blom *et al* derived path definitions for conical and cylindrical geometries to apply linearly varying fiber orientations [49, 50]. Fiber angles are measured in polar coordinates with respect to the projected center line, this is illustrated in Figure 2.11 on a flattened cone. The reference system coincides with the principal axes of the structure [33]. In-plane steering curvature and out of plane geometric curvature are split, and only the former is used for the steering constraint imposed on the design optimization. Due to the decreasing circumference overlap is inherent, for a two layer laminate this is illustrated in Figure 2.10. The tow drop technique becomes essential to produce constant thickness plies, even if no steering is present.

The path defenitions are used by the same authors to maximize the fundamental eigenfrequency of a conical structure [51]. For larger dimensions the fundamental frequency was increased up to 20%. The work was extended by a design study of a cylinder under a bending moment. The optimization objective is to maximize the buckling load subject to manufacturing, strength and stiffness constraints [52]. Multiple segments are used in circumferential direction to increase the design flexibility and the complete fiber path is formulated by five parameters. The structural responses behave non-convex in the design space due to the dependence on the fiber angle design parameters. A design of experiments is conducted to sample the design space. A surrogate model is build to approximate the structural responses and its derivatives to reduce

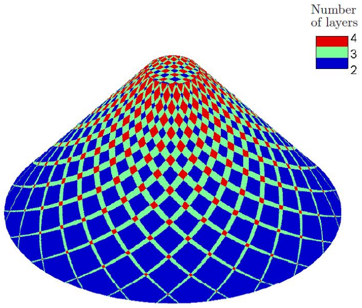

Figure 2.10: Overlap is inherent for conical surface if tow-drops are not applied. From Blom *et al* (2006) [49].

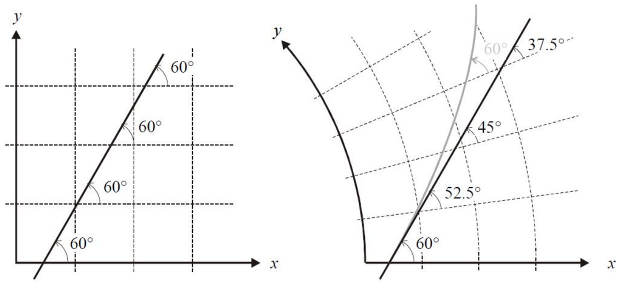

a) Rectangular coordinates b) Polar coordinates

Figure 2.11: Rectangular and polar coordinates for annular surfaces. Polar coordinates are more convenient to describe the fiber orientation in principal directions. From Gurdal *et al* (2005) [33].

the number of finite element evaluations. Improvements up to 17% were found compared to a traditionally optimized baseline design.

Other Fiber Path Parameterizations

Blom *et al* applied multiple segments to increase design flexibility. For this reason other paths representations are also researched. For example Lobatto-Legendre polynomials are introduced by Alhajahmad *et al* to add non-linear variation in fiber orientation [53]. With the gain in design freedom larger improvement steps were found.

In general the limited amount of design variables makes functional representation of fiber paths an excellent parameterization for early research of variable-stiffness design applications. However it primarily focuses on global design and does not use the complete tailoring flexibility offered by the AFP production technique.

2.2.3. Direct Stiffness Approach

The limited design flexibility from the functional representation of fiber paths resulted in the need for a parameterization that offers more design freedom. While the discrete stiffness representation offers this the structural responses show a non-convex behavior in the fiber angle design space. The direct stiffness parameterization uses a top-down approach a design parameters are directly related to the stiffness matrices. Although this may not be as intuitive the advantage is that this approach is independent of the amount of layers, reducing the design space significantly for thicker laminates.

Lamination Parameters

Laminate analysis by classical laminate plate theory is discussed in chapter 3. The stiffness properties of a laminate plate are represented by the ABD-matrix, which contains 18 unique entries. The entries themselve could be used as paramterization, but more convenient parameterization methods are introduced over time to reduce the amount of design variables. The most common parameterization is the use of lamination parameters, introduced by Tsai and Pagano in 1980 [54]. Lamination parameters are functionals of the through thickness distribution of fiber orientations. Laminate analysis by lamination parameters is elaborated in chapter 3. In the most general case 12 lamination parameters are required to describe the stiffness matrices, but for balanced symmetric stacking conditions only 6 lamination parameters suffice.

The stiffness matrices are linearly dependent on the lamination parameters. Svanberg proved that convex objective functions can be created if the structural stiffness is linearly dependent on its parameterization [55]. Grenestedt and Gudmundson proved that convexity of the object functions in the lamination parameter design space is independent of stiffness variations within the laminate [56]. This is an important property related to variable-stiffness laminates [56].

Once one lamination parameter is chosen the others cannot freely be chosen since the lamination parameters are interrelated. The explicit feasible design region in $\mathbb{R}^{12}$ is still unknown. In 2006 an efficient approach to implictly determine the feasible design region is introduced by Setoodeh *et al* that uses feasible points to create convex hulls [57]. This approach forms the basis for an optimization algorithm developed by TU Delft to design variable-stiffness laminates in the lamination parameter design space.

In a follow-up study by the same authors the convex hull of the feasible design region is used to optimize a variable-stiffness laminate for in-plane behavior under in-plane and out of plane loads [58]. Compliance minimization was numerically solved with Feasible Sequential Quadratic Programming which uses the gradient of the complementary strain energy. Compared to the constant stiffness optimum an improvement of 36% was obtained. Optimization in the fiber angle design space yields an improvement of 30%. These results show the superior use of lamination parameters over fiber angles to determine the optimal stiffness distribution. Optimization in lamination parameter space is characterized by a well-behaved convex design problem. This leads to a global optimum, whereas local optima are present in the fiber angle design space. However the lamination parameters were not converted to discretized stacking sequences, which contributes to the difference.

Sequential Approximation Routine
In 2007 the research was extended by Abdalla *et al* by implementing successive approximations to generate separable approximations of the objective function and constraints [59]. Approximations are an integral part of gradient based optimization and chapter 4 elaborates on different approximation routines. Abdalla *et al* carried out the optimization on the reciprocal approximation, ultimately leading to a new design. Only then the design will be analyzed using FEA, improving computational efficiency. This new evaluation leads to an updated approximation. Separability is convenient in discretized domains, since the design variables can be optimized locally at the nodes. Using different aspect ratios increments up to 30% in fundamental frequency was obtained.

In a follow up study in 2008 IJsselmuiden *et al* applied the method of successive approximations to buckling analysis [60]. For buckling the reciprocal approximation is non-homogeneous and non-convex, therefore a hybrid approximation aggregated from the linear and reciprocal approximations was introduced. Additionally, to improve the behavior of the optimization algorithm the conservative convex separable approximation introduced by Svanberg is implemented [61]. Optimizing for a simply supported plate under uniform end shortening results in an increment of 55% in critical buckling load. The lamination parameter distribution shows increased flexural stiffness in the middle area and increased in-plane stiffness around the edges. That is the critical buckling load optimized by local optimization of buckling resistance and global load redistribution from the middle area to the restrained edges.

Although the developed algorithm is suitable for in-plane and flexural stiffness design, designs based on strength are still impossible due to the nature of lamination parameters. Established failure criteria depend on fiber angles, and only after the fiber angle distribution is obtained in a post-processing step strength can be assessed. To resolve this IJsselmuiden *et al* introduced a conservative failure envelope in strain space. A strength response approximation is implemented within the lamination parameter optimization framework [62]. Although stiffness maximization may be used to limit excessive deformations and corresponding stresses in preliminary design, this research showed that strength based optimization yields a 48% higher safety factor.

In 2009 the buckling response approximation was updated to include buckling of curved shells [63]. Multi-modal buckling evaluation was integrated by Falk's dual formulation to include shifts between buckling modes. Compared to an isotropic design improvements up to 70-80% were obtained. A follow-up study used the same algorithm to research other compressive load applications to a variable stiffness panel [64]. A performance gain up to 189% was obtained over a conventional quasi-isotropic laminate.

Multi-Step Framework
Fiber placement machines cannot use lamination parameters as input. Once the lamination parameter distribution is known it is therefore essential to obtain a corresponding fiber angle distribution. The problem is that lamination parameters yield non-unique equivalence to stacking sequences and that the relation is non-convex [65]. Inclusion of manufacturing constraints increase the difficulty of the conversion optimization problem. In 2011 IJsselmuiden combined lamination parameter optimization, fiber angle retrieval, and fiber path construction into a 3-step design framework to get the optimal fiber path distribution [18].

Khani *et al* applied the multi-step approach to a reactangular plate with a center hole under uniaxial tension [66]. An updated failure index for strength analysis is implemented. Using a strength based optimization over a maximum stiffness optimization results in a better stress distribution, this is illustrated in Figure 2.12. The two post-processing steps to retrieve the fiber angle and fiber path result in the fiber path distribution given by Figure 2.13 for a symmetric and balanced 16-ply laminate.

In two follow-up studies Khani *et al* used the same multi-step approach to design cylinders for maximum buckling resistance successfully [67, 68]. Strength constraints were applied and improvements up to 30% are obtained.

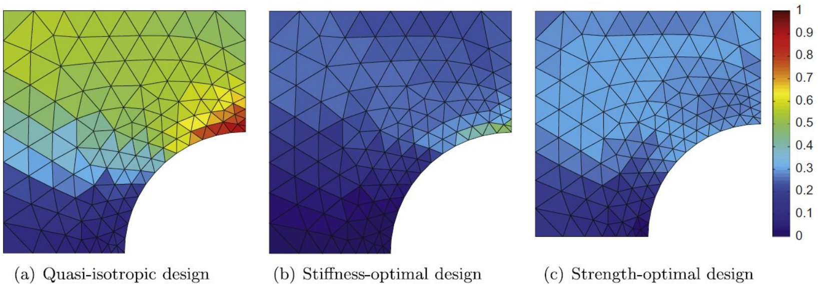

(a) Quasi-isotropic design (b) Stiffness-optimal design (c) Strength-optimal design

Figure 2.12: Failure index for a quasi-isotropic design (a), a design based on maximum stiffness optimization (b), and a design based on minimum failure index (c). Note the effective distribution for the latter, where the loads are almost equally carried by the entire structure. From Khani *et al* (2011) [66].

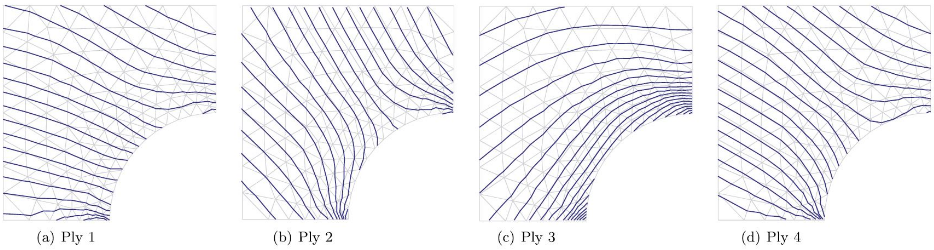

(a) Ply 1 (b) Ply 2 (c) Ply 3 (d) Ply 4

Figure 2.13: Retrieved fiber paths corresponding to minimum failure index optimization. From Khani *et al* (2011) [66].

Extension by Fiber Angle Parameterization

The fiber angle retrieval remains difficult, therefore Peeters and Abdalla adapted the multi-step framework to work with a discrete stiffness approach based on fiber angles [69, 70]. The approximations implemented in the multi-step framework are given in stiffness space for generality. Since the stiffness properties are linearly related to the lamination parameters the lamination parameters are directly superimposed. The general formulation allows to form an approximate sub-problem in the fiber angle design space. This shows similarities with a study by Setoodeh *et al* from 2008 where the generalized reciprocal approximation was used in the fiber angle design space [71].

If the general approximation is based on the optimal lamination parameter distribution the new approach can be used as a retrieval step to determine the corresponding fiber angle distribution. Furthermore true optimal fiber angle distributions are obtained by additional optimization iterations, thereby manufacturing constraints are directly imposed on the optimization design problem.

Peeters *et al* also added other functionalities to the algorithm, such as topology optimization, implementation of the 10% design rule and ply drop optimization [72–75].

Relevance to the Research Objectives

The multi-step framework and sub-approximations in fiber angle space form the basis of the presented work, therefore they are extensively discussed in chapter 4. Emphasis is on the optimization step that uses the successive, conservative and separable approximation mentioned before, but the fiber angle and fiber path retrieval steps are also briefly covered.

In chapter 4 the influence of thermal loads are added to the approximations and thermomechanical sensitivities are derived. The updated framework is used to conceptually design the engine thrust frame with a variable-stiffness laminate design.

3

Composite Laminate Analysis

Before the optimization framework is updated to include thermal effects composite laminate analysis is explained in this chapter. Classical laminate plate theory is briefly summarized in section 3.1 and laminate analysis by lamination parameters is discussed in section 3.2. To assess strength the Tsai-Wu failure criteria is shortly discussed in section 3.3. Section 3.4 explains how thermal loads can be obtained from the stacking sequence and lamination parameters. In section 3.5 thermal loads are included in the linear finite element and buckling analysis. At last section 3.6 will explain how thermal laminate analysis is implemented in the existing framework that is used for the optimization of variable-stiffness panels by fiber steering.

3.1. Classical Laminate Plate Theory

Classical laminte plate theory is thouroughly explained by many authors and is for this report based on Jones, Kassapoglou and Tsai and Hahn [6, 7, 76]. In order to simplify the calculations the constitutive relation can be simplified by plane stress assumption. It is assumed that there are no stresses at the upper side and lower side of the laminate. As a result it can be assumed that the out-of-plane variation of stresses is zero since the laminate is very thin compared to the other dimensions, i.e. stresses $\sigma_3 \approx \tau_{13} \approx \tau_{23} \approx 0$. According to Jones (1975) this assumption is not a mere idealization but functions as an objective. A lamina should only be loaded in plane stress since this is intrinsic to a lamina's fundamental capabilities. The constitutive equation describing the stress-strain relation for a single ply is now given by:

$$\begin{Bmatrix} \sigma_1 \\ \sigma_2 \\ \tau_{12} \end{Bmatrix} = \begin{bmatrix} Q_{11} & Q_{12} & 0 \\ Q_{12} & Q_{22} & 0 \\ 0 & 0 & Q_{66} \end{bmatrix} \begin{Bmatrix} \varepsilon_1 \\ \varepsilon_2 \\ \gamma_{12} \end{Bmatrix} \tag{3.1}$$

where Q_{ij} are the stiffness terms. To use this relation the orthotropic material ply properties are required. By standard coupon test the axial stiffness properties E_1, E_2 and major Poisson ratio ν_{12} can be obtained. Pure shear tests are performed to get the shear modulus G_{12}. The minor Poisson's ratio can be calculated by the relation:

$$\nu_{21} E_1 = \nu_{12} E_2 \tag{3.2}$$

$$\tag{3.3}$$

The stiffness terms Q_{11}, Q_{12}, Q_{12} and Q_{66} can be expressed by the orthotropic material ply properties:

$$Q_{11} = \frac{E_1}{1 - \nu_{12}\nu_{21}} \tag{3.4}$$

$$Q_{12} = \frac{\nu_{12} E_2}{1 - \nu_{12}\nu_{21}} = \frac{\nu_{21} E_1}{1 - \nu_{12}\nu_{21}} \tag{3.5}$$

$$Q_{22} = \frac{E_2}{1 - \nu_{12}\nu_{21}} \tag{3.6}$$

$$Q_{66} = G_{12} \tag{3.7}$$

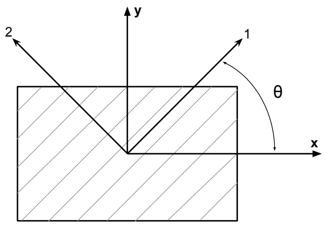

Figure 3.1: The fiber orientation θ indicates the angle between the principal axes of the ply (1,2) and the global laminate coordinate system (xy).

Constitutive Relation for a Rotated Ply

The given relations are for a single orthotropic ply. The main advantage of laminates over isotropic materials is that it is assembled from multiple plies. This gives the opportunity to tailor the design by orienting plies in different directions to improve structural performance. The in-plane rotation of a ply is illustrated in Figure 3.1, where θ is positive for counterclockwise rotation and represents the fiber angle orientation of a ply with respect to the laminate reference system. Stress and strain components will change due to this rotation according to prescribed patterns. To obtain the stiffness matrix that is aligned with the laminate coordinate system the stiffness matrix in lamina coordinates is rotated. The constitutive stress-strain relation for a rotated ply in the laminate coordinate system is given by:

$$\begin{Bmatrix} \sigma_x \\ \sigma_y \\ \tau_{xy} \end{Bmatrix} = \begin{bmatrix} \bar{Q}_{11} & \bar{Q}_{12} & \bar{Q}_{16} \\ \bar{Q}_{12} & \bar{Q}_{22} & \bar{Q}_{26} \\ \bar{Q}_{16} & \bar{Q}_{26} & \bar{Q}_{66} \end{bmatrix} \begin{Bmatrix} \varepsilon_x \\ \varepsilon_y \\ \gamma_{xy} \end{Bmatrix} \tag{3.8}$$

where entries $\bar{Q}_{ij}$ form the transformed reduced stiffness matrix. The transformed reduced stiffness terms can be calculated using $n = \sin\theta$ and $m = \cos\theta$:

$$\bar{Q}_{11} = m^4 Q_{11} + n^4 Q_{22} + 2m^2n^2 Q_{12} + 4m^2n^2 Q_{66} \tag{3.9}$$

$$\bar{Q}_{22} = n^4 Q_{11} + m^4 Q_{22} + 2m^2n^2 Q_{12} + 4m^2n^2 Q_{66} \tag{3.10}$$

$$\bar{Q}_{12} = m^2n^2 Q_{11} + m^2n^2 Q_{22} + (m^4 n^4) Q_{12} - 4m^2n^2 Q_{ss} \tag{3.11}$$

$$\bar{Q}_{66} = m^2n^2 Q_{11} + m^2n^2 Q_{22} - 2m^2n^2) Q_{12} + (m^2 - n^2)^2 Q_{ss} \tag{3.12}$$

$$\bar{Q}_{16} = m^3 n Q_{11} - mn^3 Q_{22} + (mn^3 - m^3 n) Q_{12} + 2(mn^3 - m^3 n) Q_{66} \tag{3.13}$$

$$\bar{Q}_{26} = n^3 m Q_{11} - nm^3 Q_{22} + (nm^3 - n^3 m) Q_{12} + 2(nm^3 - n^3 m) Q_{66} \tag{3.14}$$

The variation of the transformed reduced stiffness terms for a varying fiber orientation are given in Figure 3.2. The variations show that optimization based on fiber angle parameterization results in a non-convex response, the statement given in chapter 2.

Ply Density

Before explaining how the laminate properties are calculated the definition of ply density if introduced. Figure 3.3 (left) indicates the used convention for ply numbering. The first ply is the outer most ply laying at the outside of the stack. In this work laminates are considered to be symmetric, therefore the last design layer d lays at the symmetry axis. The through thickness coordinate z is also illustrated, where the through thickness value at the top of ply k is indicated as z_{k-1} and the bottom as z_k. Ply density is used to scale the ply thickness to allow for thickness optimization. The density factor is a value between 0 and 1 and scales the physical thickness t_k^0 of ply k to a thickness to be used for laminate analysis by:

$$t_k = \rho_k t_k^0 \quad \text{for} \quad 0 \leq \rho_k \leq 1 \tag{3.15}$$

This effect is explained in Figure 3.3 (right). Since such range of ply thickness is physically not possible to manufacture it is preferred to have density values of either 1 or 0 referring to plies being fully present or not present respectively. A black and white formulation is included in the optimization to either have a ply

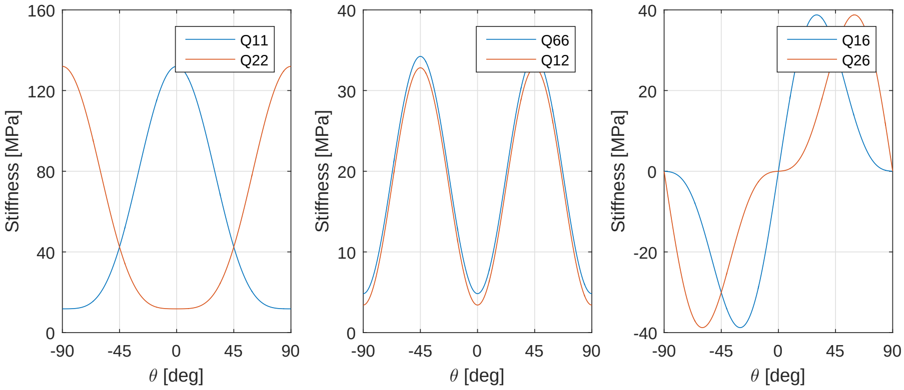

Figure 3.2: Variation of Q for a rotating fiber orientation θ. It shows the non-convex relation to the stiffness terms. Note that for a rotation of zero degrees the components correspond to the stiffness matrix of a single ply: $\bar{Q}_{16} = \bar{Q}_{26} = 0$, $\bar{Q}_{11} = Q_{11}$, $\bar{Q}_{12} = Q_{12}$, $\bar{Q}_{22} = Q_{22}$ and $\bar{Q}_{66} = Q_{66}$.

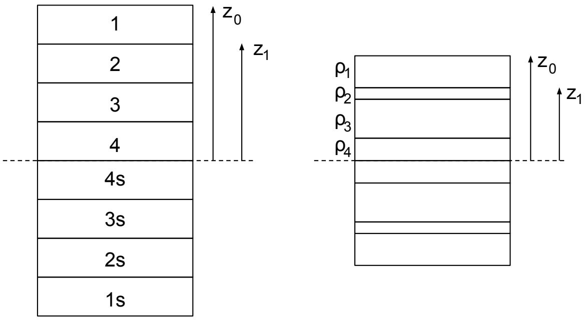

Figure 3.3: Convention for ply numbering (left) and the influence of ply density on the ply thickness and through thickness coordinate z (right). Reproduced from Peeters (2017) [77].

present or not, in this way thickness is optimized by ply drops. For generality the laminate properties are calculated for any density value by changing the through thickness z-coordinates according to:

$$z_k(\boldsymbol{\rho}) = \sum_{i=1}^{s} \rho_i t_i^0 - \sum_{j=1}^{k} \rho_j t_j^0 \tag{3.16}$$

where s indicates the number of symmetric plies and k the ply of interest. The corresponding change in ply-thicknesses will influence the laminate stiffness matrices $\mathbf{A}$ and $\mathbf{D}$ and the thermal load $\mathbf{N}^{Th}$, which will be explained in the next section.

Laminate Stiffness Matrices

In classical laminate plate theory the strains are assumed to be linear through the thickness by Equation 3.17, where ε^0 is the mid-plane strain and κ is the curvature of the laminate. This is a crucial assumption based on the Kirchhoff-Love theory [7].

$$\left\{\begin{array}{c} \varepsilon_x \\ \varepsilon_y \\ \gamma_{xy} \end{array}\right\} = \left\{\begin{array}{c} \varepsilon_x^0 \\ \varepsilon_y^0 \\ \gamma_{xy}^0 \end{array}\right\} + z \left\{\begin{array}{c} \kappa_x \\ \kappa_y \\ \kappa_{xy} \end{array}\right\} \tag{3.17}$$

The stresses in a ply depend on the fiber orientation, since this affects the transformed reduced stiffness matrix. Laminates are normally very thin and it is convenient to use stress resultants which represent the integrated stress state of the laminate by:

$$\mathbf{N} = \int_{-\frac{h}{2}}^{\frac{h}{2}} \boldsymbol{\sigma}\, dz = \int_{-\frac{h}{2}}^{\frac{h}{2}} \bar{\mathbf{Q}}\boldsymbol{\varepsilon}\, dz \tag{3.18}$$

$$\mathbf{M} = \int_{-\frac{h}{2}}^{\frac{h}{2}} \boldsymbol{\sigma} z\, dz = \int_{-\frac{h}{2}}^{\frac{h}{2}} \bar{\mathbf{Q}}\boldsymbol{\varepsilon} z\, dz \tag{3.19}$$

where **N** is the force resultant per unit width and similarly **M** is the moment resultant per unit width. With the stress resultants and the linear through thickness strains the ABD-matrix can be obtained. The ABD-matrix relates the midplane strain and curvature to the force and moment resultants. The **A**-Matrix corresponds to in-plane behavior of the laminate. The **D**-matrix corresponds to pure bending behavior of the laminate. The **B**-matrix corresponds to bending-stretching coupling of the laminate. Based on the ply orientation it is possible that the laminate bends under in-plane loads, or that the laminate exhibits in-plane extension under bending loads. The **A**, **B** and **D** matrices are calculated by:

$$A_{ij} = \int_{-\frac{h}{2}}^{\frac{h}{2}} \bar{Q}_{ij}\, dz = \sum_{k=1}^{n} (\bar{Q}_{ij})^{(k)} (z_{k-1} - z_k) \tag{3.20}$$

$$B_{ij} = \int_{-\frac{h}{2}}^{\frac{h}{2}} \bar{Q}_{ij} z\, dz = \sum_{k=1}^{n} (\bar{Q}_{ij})^{(k)} \frac{z_{k-1}^2 - z_k^2}{2} \tag{3.21}$$

$$D_{ij} = \int_{-\frac{h}{2}}^{\frac{h}{2}} \bar{Q}_{ij} z^2\, dz = \sum_{k=1}^{n} (\bar{Q}_{ij})^{(k)} \frac{z_{k-1}^3 - z_k^3}{3} \tag{3.22}$$

Now the ABD-matrix is known the force and moment resultants are obtained by multiplication with the mid-plane strain and the laminate curvature:

$$\begin{Bmatrix} N_x \\ N_y \\ N_{xy} \\ M_x \\ M_y \\ M_{xy} \end{Bmatrix} = \begin{bmatrix} A_{11} & A_{12} & A_{16} & B_{11} & B_{12} & B_{16} \\ A_{12} & A_{22} & A_{26} & B_{12} & B_{22} & B_{26} \\ A_{16} & A_{26} & A_{66} & B_{16} & B_{26} & B_{66} \\ B_{11} & B_{12} & B_{16} & D_{11} & D_{12} & D_{16} \\ B_{12} & B_{22} & B_{26} & D_{12} & D_{22} & D_{26} \\ B_{16} & B_{26} & B_{66} & D_{16} & D_{26} & D_{66} \end{bmatrix} \begin{Bmatrix} \varepsilon_x^0 \\ \varepsilon_y^0 \\ \gamma_{xy}^0 \\ \kappa_x \\ \kappa_y \\ \kappa_{xy} \end{Bmatrix} \tag{3.23}$$

It is mentioned before that in this work only symmetric laminates are applied. Therefore there is no bending-extension coupling and the **B**-matrix is equal to zero. Therefore the governing equation is simplified to:

$$\mathbf{N} = \mathbf{A}\boldsymbol{\varepsilon}^0 \qquad \text{and} \qquad \mathbf{M} = \mathbf{D}\boldsymbol{\kappa} \tag{3.24}$$

3.2. Lamination Parameters

Traditionally laminate plate theory with fiber angle parameterization is used in the design of composite laminates. Using this parameterization potentially creates an enormous design space for fine discretizations with ill-behaved objective functions, as is explained in the chapter 2. Due to the non-linear relation between ply angles and stiffness it becomes hard to understand how the ABD-matrix will change if multiple plies are rotated.

An alternative is to use a direct stiffness approach based on lamination parameters. Lamination parameters were first introduced by Tsai and Pagano [54]. By use of various trigonometric identities they were able to do rewrite the transformed reduced stiffness terms in a simplified form:

$$\begin{aligned}
\bar{Q}_{11} &= U_1 + U_2\cos 2\theta + U_3\cos 4\theta \\
\bar{Q}_{22} &= U_1 - U_2\cos 2\theta + U_3\cos 4\theta \\
\bar{Q}_{12} &= U_4 - U_3\cos 4\theta \\
\bar{Q}_{16} &= -\tfrac{1}{2}U_2\sin 2\theta - U_3\sin 4\theta \\
\bar{Q}_{26} &= -\tfrac{1}{2}U_2\sin 2\theta + U_3\sin 4\theta \\
\bar{Q}_{66} &= U_5 - U_3\cos 4\theta
\end{aligned} \tag{3.25}$$

$$\begin{aligned}
U_1 &= \frac{3Q_{11} + 3Q_{22} + 2Q_{12} + 4Q_{66}}{8} \\
U_2 &= \frac{Q_{11} - Q_{22}}{2} \\
U_3 &= \frac{Q_{11} + Q_{22} - 2Q_{12} - 4Q_{66}}{8} \\
U_4 &= \frac{Q_{11} + Q_{22} + 6Q_{12} - 4Q_{66}}{8} \\
U_5 &= \frac{Q_{11} + Q_{22} - 2Q_{12} + 4Q_{66}}{8}
\end{aligned} \tag{3.26}$$

Note that the sign in $\bar{Q}_{16}$ and $\bar{Q}_{16}$ is opposite to the sign used by Tsai and Pagano since they used the opposite sign notation for fiber orientation [14, 16]. The transformed reduced stiffnesses are based on material invariants U_{1-5}. These material invariants are invariant of orientation θ and depend on the material properties only. Therefore the newly obtained set of equations for $\bar{Q}_{ij}$ contain an invariant part. In Figure 3.4 $\bar{Q}_{11}$ and $\bar{Q}_{22}$ are decomposed to show the variation of each term. Some understanding of the material invariants can now be derived. The left graphs are the total variation for a varying θ. The variation of the three individual terms is presented in the other graphs in the row, which superimposed yield the same variance as the left graph.

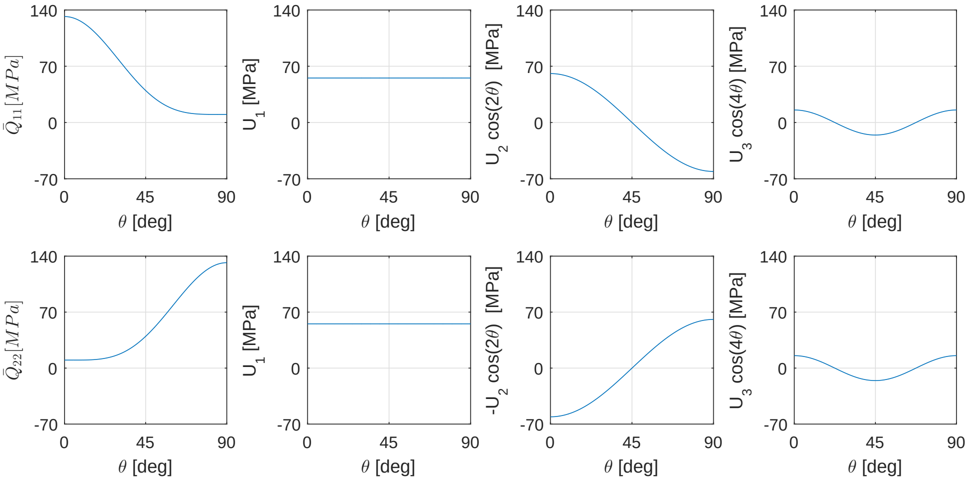

Figure 3.4: Decomposition of $\bar{Q}_{11}$ and $\bar{Q}_{22}$. The left graphs present the total variance and the right three graphs represent the variance of the individual terms.

For $\bar{Q}_{11}$ the first term is U_1, which represents the quasi-isotropic material properties and is invariant of θ. The second term is $U_2\cos(2\theta)$ and reduces from $+X$ to $-X$ for $\theta = 0$ to $\theta = 90$ degrees respectively and is zero at $\theta = 45$ degrees. This term includes the dominant longitudinal/transverse stiffness deviation from the quasi-isotropic stiffness. This explains why this term is of opposite sign for $\bar{Q}_{11}$ and $\bar{Q}_{22}$. The third term varies at a higher frequency but generally has less influence on the stiffness values due to the lower value of U_3. The term is highest at 0 and 90 degrees and lowest at 45 degrees. This indicates that this component gives a relation between shear and axial stiffness for a given orientation. In a similar fashion one can decompose the other $\bar{Q}_{ij}$-values.

Based on the new formulation of the transformed reduced stiffness terms the **A**, **B** and **D** matrix can now be obtained by:

$$[\mathbf{A},\mathbf{B},\mathbf{D}] = \left[h, \frac{h^2}{4}, \frac{h^3}{12}\right]\left(\boldsymbol{\Gamma}_0 V_0^{A,B,D} + \boldsymbol{\Gamma}_1 V_1^{A,B,D} + \boldsymbol{\Gamma}_2 V_2^{A,B,D} + \boldsymbol{\Gamma}_3 V_3^{A,B,D} + \boldsymbol{\Gamma}_4 V_4^{A,B,D}\right) \tag{3.27}$$

in which Γ_i are matrices containing the material invariants:

$$\begin{aligned}
&\Gamma_0 = \begin{bmatrix} U_1 & U_4 & 0 \\ U_4 & U_1 & 0 \\ 0 & 0 & U_5 \end{bmatrix} \quad \Gamma_1 = \begin{bmatrix} U_2 & 0 & 0 \\ 0 & -U_2 & 0 \\ 0 & 0 & 0 \end{bmatrix} \quad \Gamma_2 = \begin{bmatrix} 0 & 0 & \frac{1}{2}U_2 \\ 0 & 0 & \frac{1}{2}U_2 \\ \frac{1}{2}U_2 & \frac{1}{2}U_2 & 0 \end{bmatrix} \\
&\Gamma_3 = \begin{bmatrix} U_3 & -U_3 & 0 \\ -U_3 & U_3 & 0 \\ 0 & 0 & 0 \end{bmatrix} \quad \Gamma_4 = \begin{bmatrix} 0 & 0 & U_3 \\ 0 & 0 & -U_3 \\ U_3 & -U_3 & 0 \end{bmatrix}
\end{aligned} \tag{3.28}$$

The lamination parameters $V_i^{A,B,D}$ contain the through thickness integrated properties of the variant terms of the transformed reduced stiffness terms given in Equation 3.25. All lamination parameters $V_i^{A,B,D} \in [-1,1]$ are calculated by:

$$\begin{aligned}
V_0^{A,B,D} &= [1,0,1] \\
V_1^{A,B,D} &= \int_{-1/2}^{1/2} \cos 2\theta \left[1,\bar{z},\bar{z}^2\right] d\bar{z} \\
V_2^{A,B,D} &= \int_{-1/2}^{1/2} \sin 2\theta \left[1,\bar{z},\bar{z}^2\right] d\bar{z} \\
V_3^{A,B,D} &= \int_{-1/2}^{1/2} \cos 4\theta \left[1,\bar{z},\bar{z}^2\right] d\bar{z} \\
V_4^{A,B,D} &= \int_{-1/2}^{1/2} \sin 4\theta \left[1,\bar{z},\bar{z}^2\right] d\bar{z}
\end{aligned} \tag{3.29}$$

Note that in these equations the laminate thickness h is factorized, therefore the integrals for the lamination parameters can be assessed by upper and lower bounds of $\frac{1}{2}$ and $-\frac{1}{2}$ instead. Equation 3.27 shows that matrices A, B and D are linear dependent on the 12 lamination parameters and the laminate thickness. Svanberg proved that convex objective functions can be created if the structural stiffness is linearly dependent on its parameterization [55]. Furthermore only six lamination parameters are required to describe a balanced symmetric laminate and this limits the number of design variables. Combining these characteristics yield favorable properties for optimization.

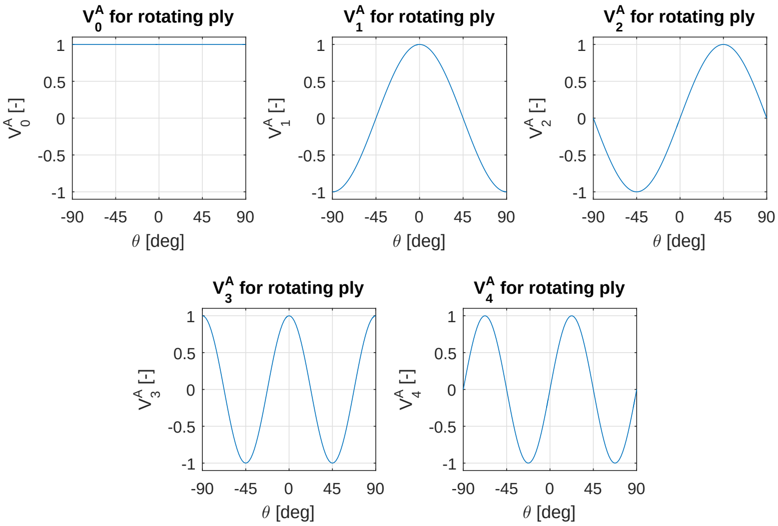

Figure 3.5: Relation of lamination parameters V_i^A to a varying ply angle θ for a single ply laminate.

However, it may be harder to understand lamination parameters physically. The lamination parameter variation for a single ply is given by Figure 3.5 to better understand what happens when a ply is rotated. For membane stiffness given by the A-matrix [18]:

- Γ_0: Matrix Γ_0 stands for the quasi-isotropic laminate properties, normalized by the laminate thickness. For this reason it is the only Γ-matrix not multiplied by a lamination parameter. IJsselmuiden states that Γ_0 is the quasi-isotropic basis for the stiffness properties and the lamination parameters can be used to tailor the laminate in desirable directional properties. Therefore it is intrinsic that for a quasi-isotropic stacking sequence the lamination parameters V_1^A to V_4^A are zero.
- $V_1^A\Gamma_1$: Matrix Γ_1 contains information related to the axial stiffness entries A_{11} and A_{22}. Therefore $V_1^A\Gamma_1$ changes the longitudinal and transverse axial stiffness direction. For example if V_1^A reaches 1 most plies are aligned at 0 degrees and A_{11} is dominant. If V_1^A reaches -1 the opposite is true and mainly 90 degree oriented plies are present and A_{22} becoming dominant. In general this is the most dominant term to tailor the design.
- $V_2^A\Gamma_2$ and $V_4^A\Gamma_4$: Both matrices Γ_2 and Γ_4 only contain material invariants at the shear-extension entries. In combination with the lamination parameters this term influences the shear-extension coupling of the laminate expressed by A_{16} and A_{26}. It is known for a balanced laminate that there is no shear-extension coupling, therefore a balanced laminate inherently has lamination parameters V_2^A and V_4^A equal to zero. In Figure 3.5 the parameters reach ± 1 since unidirectional laminates oriented other than 0 or 90 degrees are the "most unbalanced" laminates. For non-unidirectional unbalanced laminates the lamination parameters will have a maximum absolute value between 0 and 1 based on the severity of the unbalanced design.
- $V_3^A\Gamma_3$: Matrix Γ_3 relates the axial and shear stiffness and extension coupling and bending coupling. Physically this represents the ratio between 45 degree plies and 0,90 degree plies. As one can see in Figure 3.5 if V_3^A reaches -1 most plies will have a 45 degree orientation and the shear stiffness will increase. As V_3^A reaches 1 the axial and transverse stiffness increases at a cost of shear stiffness. Note that based on V_3^A nothing can be said about the ratio 0,90 degree plies.

Feasible Design Space

Once one lamination parameter is chosen the others cannot freely be chosen. The lamination parameters are not independent, since they are based on the same variation of ply orientations through the thickness. Although $V_i^{A,B,D} \in [-1,1]$ holds this explains why the design domain is not simply given by the full unit cube $[-1,1]^{12}$ in $\mathbb{R}^{12}$ [65]. There exist a feasible design region where values of lamination parameters are limited by others. For the general case with 12 lamination parameters this feasible region is still unknown and has yet to be determined. Although this feasible region is unknown, Grenestedt and Gudmundson were able to prove that the feasible design region for the 12 lamination parameters in $\mathbb{R}^{12}$ is convex [56].

Together the concave objective function and convex feasible design space lead to a well-behaved objective function. Global optima is obtained, whereas using fiber orientation as parameterization leads to ill-behaved objective functions with many local optima, especially for buckling [42, 56]. In Appendix A the feasible design space is elaborated, specifically for symmetric and balanced laminates.

3.3. Tsai-Wu Failure Criteria

Failure critera can be distinguised in two categories, namely stress-based and fracture-mechanics-based criteria [78]. The former assesses failure by checking if the stress within the structure reaches a critical value. The latter assumes that failure occurs by growth of initial flaws. For the design of a composite panel with variable-stiffness a stress-based failure criteria is easier to implement within the optimization routine.

The easiest way to assess failure is by the simple non-interactive maximum stress criterion. One could simply check if stresses expressed in the material ply axes exceed the strength values obtained from coupon tests. However, it is known that stresses interact and therefore interaction behavior should be included for more accurate failure predictions. The Von Mises and Tresca yield criteria include this behavior for isotropic materials. The Tsai-Wu formula is probably the best known failure criterion for anisotropic laminates and has acceptable predictions compared with test results [6]. This criteria was first introduced by Tsai and Wu in 1971 and is more of a curve fit rather than a physics based theory [6, 79]. For a 2-dimensional planar stress state the failure index f is calculated by:

$$f = F_{11}\sigma_1^2 + F_{22}\sigma_2^2 + F_{66}\tau_{12}^2 + F_1\sigma_1 + F_2\sigma_2 + 2F_{12}\sigma_1\sigma_2 \tag{3.30}$$

where the F-values are given in Appendix B and are based on the strength values in the material ply axes derived from compression and tensile coupon tests. The failure index is useful to assess first ply failure. First ply failure is predicted to occur within a laminate if the following relation is violated:

$$f \leq 1 \tag{3.31}$$

To determine the critical load for first ply failure the input loads should be increased until the failure index becomes larger then one at a certain location for one of the plies.

Conservative Failure Envelope in Strain Space

To address the failure index the stress state of the individual plies are required, which are based on the fiber orientation. Lamination parameters represent the integrated laminate properties over the thickness. Assessing failure criteria is not straight forward since orientations are unknown. It would be inefficient to apply failure criteria after retrieval of the fiber orientations. Therefore IJsselmuiden *et al* proposed to apply a conservative Tsai-Wu failure criteria [62].

Using the constitutive stress-strain relation the Tsai-Wu failure index given by Equation 3.30 is tranformed into strain space. The criteria still depends on the stacking sequence, therefore it cannot be used in conjunction with lamination parameter optimization. However, it is possible to determine a region in strain space that is safe regardless of the stacking sequence. The boundary of this conservative region in strain space is given by the failure envelope and every point that lays within the enclosed area will fulfill the Tsai-Wu failure criteria. This envelope is derived by IJsselmuiden *et al* and later simplified by the same authors to [62, 66]:

$$f = \frac{1}{2}u_1 I_1^2 + u_2 I_1 I_4 + \frac{1}{2}u_3 I_4^2 + u_4 I_2 + u_5 I_1 + u_6 I_4 \tag{3.32}$$

where I_i and u_i and are respectively strain invariants and parameters to map the stress-based Tsai-Wu criteria in strain-space. The failure envelope is given by the most critical fiber angle where the failure index equals one:

$$\max_{\theta} f = 1 \tag{3.33}$$

Note that this formulation is conservative, especially for load conditions where certain stacking sequences are known to be avoided. For example, it is common to use ±45 oriented plies at the outside of a stack to improve bending resistance, however the conservative failure criteria does not take such design rules into consideration and will also assess fiber angles that are normally avoided. The conservative failure envelope can be expressed in terms of I_i and u_i, for the sake of brevity this formulation is given in Appendix B.

3.4. Thermal Laminate Analysis

So far the stress-strain relations are based on mechanical imposed strains. Before optimization of thermo-mechanical load applications can be performed the influence of thermal loads should be included in the governing stress-strain relations. The analysis presented in this section is based on Gurdal *et al* and Staab [80, 81].

Thermal Uni-directional Ply Analysis

When thermal loads are applied a structure can undergo stress free thermal expansion. An unconstrained plate will expand and contract without creating internal stresses for a uniform temperature difference. The stress free thermal expansion for a uni-directional ply is given by:

$$\begin{Bmatrix} \varepsilon_1^{\text{FT}} \\ \varepsilon_2^{\text{FT}} \\ \gamma_{12}^{\text{FT}} \end{Bmatrix} = \begin{Bmatrix} \alpha_1 \\ \alpha_2 \\ 0 \end{Bmatrix} \cdot \Delta T \tag{3.34}$$

where α is the coefficient of thermal expansion (CTE). Mechanical strains and thermal strains induced by mechanical and thermal loads can be superimposed to yield the total strain:

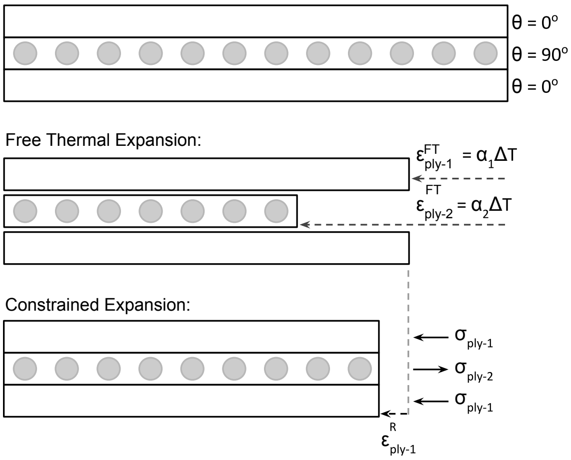

Figure 3.6: Thermal expansion of a ply is constrained by adjacent plies. The first laminate presents a laminate not exposed to thermal loads. The second laminate illustrates the stress free thermal contraction of the single plies. However, the plies are not free to contract due to the bonding with the adjacent plies. This will constrain the contraction of the layers and cause residual stresses and strains, which is illustrated in the third laminate. Adjusted from Staab [81].

$$\boldsymbol{\varepsilon}^{\text{Tot}} = \boldsymbol{\varepsilon}^{\text{M}} + \boldsymbol{\varepsilon}^{\text{FT}} \tag{3.35}$$

Note that ε^{FT} corresponds to stress free thermal expansion, thus in this formulation only mechanical strain will cause stresses in the structure. If the ply is free to expand/contract for a pure thermal load the total strain equals the stress free thermal expansion, thus no stresses are present within the structure. If the thermal expansion/contraction is fully constrained the total strain equals zero and a mechanical strain of $-\varepsilon^{\text{FT}}$ is induced which will exert stresses in the ply. Hence the stress-strain relation for a single ply subject to mechanical and thermal loads is given by the following equation:

$$\begin{Bmatrix} \sigma_1 \\ \sigma_2 \\ \tau_{12} \end{Bmatrix} = \begin{bmatrix} Q_{11} & Q_{12} & 0 \\ Q_{12} & Q_{22} & 0 \\ 0 & 0 & Q_{66} \end{bmatrix} \underbrace{\left(\begin{Bmatrix} \varepsilon_1^{\text{Tot}} \\ \varepsilon_2^{\text{Tot}} \\ \gamma_{12}^{\text{Tot}} \end{Bmatrix} - \begin{Bmatrix} \varepsilon_1^{\text{FT}} \\ \varepsilon_2^{\text{FT}} \\ \gamma_{12}^{\text{FT}} \end{Bmatrix} \right)}_{\varepsilon^M} \tag{3.36}$$

When a ply is rotated with respect to the laminate coordinate system the thermal expansion coefficient of the ply can be rotated to the laminate coordinate system using $m = \cos\theta$ and $n = \sin\theta$:

$$\begin{Bmatrix} \varepsilon_x^{\text{FT}} \\ \varepsilon_y^{\text{FT}} \\ \gamma_{xy}^{\text{FT}} \end{Bmatrix} = \begin{bmatrix} \alpha_1 m^2 + \alpha_2 n^2 \\ \alpha_1 n^2 + \alpha_2 m^2 \\ 2(\alpha_1 - \alpha_2) mn \end{bmatrix} \cdot \Delta T \quad \rightarrow \quad \begin{Bmatrix} \varepsilon_x^{\text{FT}} \\ \varepsilon_y^{\text{FT}} \\ \gamma_{xy}^{\text{FT}} \end{Bmatrix} = \begin{Bmatrix} \alpha_x \\ \alpha_y \\ \alpha_{xy} \end{Bmatrix} \cdot \Delta T \tag{3.37}$$

Thermal Laminate Analysis

Looking at a laminate of multiple plies, the adjacent plies will constrain the free thermal expansion of a single layer. This is effect is illustrated in Figure 3.6. This restraining will cause stresses, referred to as residual stresses since they are often considered with curing temperatures. The residual strain $\boldsymbol{\varepsilon}^R$ due to a pure thermal load of ply k within a laminate is given by:

$$\boldsymbol{\varepsilon}_k^{\text{R}}(z_k) = \boldsymbol{\varepsilon}^{\text{Tot,0}} + z_k \boldsymbol{\kappa}^{\text{Tot}} - \boldsymbol{\varepsilon}^{\text{TF}}(z_k) \tag{3.38}$$

where z_k represents the through thickness ply location within the laminate. Note that the stress free thermal expansion depends on z_k if asymmetrical laminates and through thickness temperature gradients are considered. With the calculated strain the residual stress can be obtained:

$$\boldsymbol{\sigma}_k^{\mathrm{R}}(z_k) = \left[\bar{\mathbf{Q}}_k\right] \boldsymbol{\varepsilon}^{\mathrm{R}}(z_k) \tag{3.39}$$

However, the total strains are unknown and the residual strains cannot be calculated. Therefore it is convenient to represent the residual strains and stresses by equivalent thermal loads. For a pure thermal load case there are no external forces, hence an equivalent thermal load can be calculated that corresponds to the existing stress state by:

$$\mathbf{N}^{\mathrm{R}} = \int_{-\frac{h}{2}}^{\frac{h}{2}} \boldsymbol{\sigma}^{\mathrm{R}} dz = 0 \quad \rightarrow \quad \mathbf{N}^{\mathrm{Th}} = \int_{-\frac{h}{2}}^{\frac{h}{2}} [\bar{\mathbf{Q}}]\, \boldsymbol{\varepsilon}^{\mathrm{Tot}} dz = \int_{-\frac{h}{2}}^{\frac{h}{2}} [\bar{\mathbf{Q}}]\, \boldsymbol{\varepsilon}^{\mathrm{FT}} dz = \int_{-\frac{h}{2}}^{\frac{h}{2}} [\bar{\mathbf{Q}}] \begin{Bmatrix} \alpha_x \\ \alpha_y \\ \alpha_{xy} \end{Bmatrix} \Delta T\, dz \tag{3.40}$$

In a similar way the equivalent thermal moment resultant can be computed:

$$\mathbf{M}^{\mathrm{R}} = \int_{-\frac{h}{2}}^{\frac{h}{2}} \boldsymbol{\sigma}^{\mathrm{R}} z\, dz = 0 \quad \rightarrow \quad \mathbf{M}^{\mathrm{Th}} = \int_{-\frac{h}{2}}^{\frac{h}{2}} [\bar{\mathbf{Q}}]\, \boldsymbol{\varepsilon}^{\mathrm{Tot}} z\, dz = \int_{-\frac{h}{2}}^{\frac{h}{2}} [\bar{\mathbf{Q}}]\, \boldsymbol{\varepsilon}^{\mathrm{FT}} z\, dz = \int_{-\frac{h}{2}}^{\frac{h}{2}} [\bar{\mathbf{Q}}] \begin{Bmatrix} \alpha_x \\ \alpha_y \\ \alpha_{xy} \end{Bmatrix} \Delta T\, z\, dz \tag{3.41}$$

Now the stress strain relation including thermal loads can be written as:

$$\begin{Bmatrix} \mathbf{N} \\ \mathbf{M} \end{Bmatrix} = \begin{bmatrix} \mathbf{A} & \mathbf{B} \\ \mathbf{B} & \mathbf{D} \end{bmatrix} \begin{Bmatrix} \boldsymbol{\varepsilon}^{\mathbf{0}} \\ \boldsymbol{\kappa} \end{Bmatrix} - \begin{Bmatrix} \mathbf{N}^{\mathrm{Th}} \\ \mathbf{M}^{\mathrm{Th}} \end{Bmatrix} \tag{3.42}$$

Thermal Loads by Lamination Parameters

The equivalent thermal loads can also be calculated with lamination parameters. Three thermal invariants are introduced:

$$K_1 = (U_1 + U_4)(\alpha_1 + \alpha_2) + U_2(\alpha_1 - \alpha_2) \tag{3.43}$$

$$K_2 = U_2(\alpha_1 + \alpha_2) + (U_1 + 2U_3 - U_4)(\alpha_1 - \alpha_2) \tag{3.44}$$

$$K_3 = U_2(\alpha_1 + \alpha_2) + 2(U_3 + U_5)(\alpha_1 - \alpha_2) \tag{3.45}$$

These invariants depend only on the material invariants and the thermal expansion coefficients of the ply and are independent of the ply rotation. The equivalent thermal loads can now be calculated by:

$$\mathbf{N}^{\mathrm{Th}} = \frac{1}{2} \int_{-\frac{h}{2}}^{\frac{h}{2}} \begin{Bmatrix} K_1 + K_2 \cos 2\theta \\ K_1 - K_2 \cos 2\theta \\ K_3 \sin 2\theta \end{Bmatrix} \Delta T\, dz = \frac{1}{2} h \begin{Bmatrix} V_0^A K_1 + V_1^A K_2 \\ V_0^A K_1 - V_1^A K_2 \\ V_2^A K_3 \end{Bmatrix} \Delta T \tag{3.46}$$

$$\mathbf{M}^{\mathrm{Th}} = \frac{1}{2} \int_{-\frac{h}{2}}^{\frac{h}{2}} \begin{Bmatrix} K_1 + K_2 \cos 2\theta \\ K_1 - K_2 \cos 2\theta \\ K_3 \sin 2\theta \end{Bmatrix} \Delta T\, z\, dz = \frac{1}{2} \frac{h^2}{4} \begin{Bmatrix} V_1^B K_2 \\ -V_1^B K_2 \\ V_2^B K_3 \end{Bmatrix} \Delta T \tag{3.47}$$

3.5. Linear Finite Element and Buckling Analysis

To allow for intricate geometry an 18 degree of freedom (DOF) triangular shell element is used in the finite element routine. This element is superimposed from a membrane and a bending element. The membrane element is a 12 DOF triangular element that includes drilling degrees of freedom (i.e. in-plane rotation). The bending element is based on the 9 DOF Kirchoff-plate triangular bending element. The elements are high performance finite elements and the stiffness matrix is decomposed in a basic and higher-order stiffness matrix. How these matrices are build is well documented in templates provided by Felippa and Militello [82–84]. In the next two sections it will be explained how the element properties are tied to the linear finite element and buckling analysis.

3.5.1. Linear Finite Element Analysis

The parameterization of the design variables is executed at nodal level. To perform finite element analysis the nodal properties have to be mapped to elemental properties. To generate a smooth distribution reciprocal interpolation of the stiffness matrices is used [59]:

$$\mathbf{A}_e^{-1} = \sum_{n \in \Upsilon_e} w_n \mathbf{A}_n^{-1} \tag{3.48}$$

where Υ_e is the set of nodes connected to element e. The value of weight w_n depends on the element type and is equal to $\frac{1}{3}$ for the triangular elements used in the finite element routine. The linear finite element problem is solved to compute the displacements:

$$\mathbf{K} \cdot \mathbf{u} = \mathbf{F}^{\mathrm{M}} + \mathbf{F}^{\mathrm{Th}} = \mathbf{F} \tag{3.49}$$

For a general membrane element the stiffness matrices $\mathbf{K}_e$ to build the global stiffness matrix are calculated by the relationship:

$$\mathbf{K}_e = \int_{\Omega_e} h_e \mathbf{B}_e^t \mathbf{A}_e \mathbf{B}_e d\Omega_e \tag{3.50}$$

where $\mathbf{B}$ is the strain displacement matrix and Ω is the element domain. The nodal forces acting on the structure are given by the right hand sight of Equation 3.49. The mechanical forces $\mathbf{F}^{\mathrm{M}}$ are given as an input and the equivalent thermal forces $\mathbf{F}^{\mathrm{Th}}$ are derived from the thermal loads by:

$$\mathbf{F}_e^{\mathrm{Th}} = \int_{\Omega_e} \mathbf{B}_e^t \mathbf{N}^{\mathrm{Th}} d\Omega_e = A_e \cdot \bar{\mathbf{B}}_e \cdot \mathbf{N}_e^{\mathrm{Th}} \tag{3.51}$$

Since the thermal loads are assumed to be constant within the element the integral over the domain results in the area A multiplied by the average strain displacement matrix $\bar{\mathbf{B}}$. Note that the thermal element loads are calculated from the nodal properties according to:

$$\mathbf{N}_e^{\mathrm{Th}} = \sum_{n \in \Upsilon_e} w_n \mathbf{N}_n^{\mathrm{Th}} \tag{3.52}$$

After executing the linear finite element analysis and calculating the displacements the element strains and curvatures can be found by:

$$\boldsymbol{\varepsilon}_e = \bar{\mathbf{B}}_e \mathbf{u}_e \tag{3.53}$$

From the strains and curvatures the stress resultants are then obtained by Equation 3.42. The equation is repeated for convenience:

$$\begin{Bmatrix} \mathbf{N} \\ \mathbf{M} \end{Bmatrix} = \begin{bmatrix} \mathbf{A} & \mathbf{B} \\ \mathbf{B} & \mathbf{D} \end{bmatrix} \begin{Bmatrix} \boldsymbol{\varepsilon}^{\mathbf{0}} \\ \boldsymbol{\kappa} \end{Bmatrix} - \begin{Bmatrix} \mathbf{N}^{\mathrm{Th}} \\ \mathbf{M}^{\mathrm{Th}} \end{Bmatrix} \tag{3.54}$$

The thermal stress resultants have to be subtracted to get the actual stress state. Once the stresses are known the failure criteria can be assessed and the buckling analysis can be executed.

3.5.2. Buckling Analysis

Within this work only the critical buckling load is considered and post-buckling behavior is not evaluated. The critical buckling load can be assessed by the linear prebuckling stability eigenvalue problem [63, 64, 71].

$$\left(\mathbf{K}_m - \lambda \mathbf{K}_g\right) \mathbf{a} = 0 \tag{3.55}$$

where $\mathbf{K}_m$ is the global material stiffness matrix, $\mathbf{K}_g$ is the global geometrical stiffness matrix, and $\mathbf{a}$ is the mode shape. The mode shapes are normalized so the following relation holds:

$$\mathbf{a}^t \cdot \mathbf{K}_m \cdot \mathbf{a} = 1 \tag{3.56}$$

The global geometrical stiffness matrix is related to the in-plane stress resultants of the elements $\mathbf{N} = \left(n_x, n_y, n_{xy}\right)^t$ and constant matrices that depend on the element geometry $\mathbf{K_x}$, $\mathbf{K_y}$ and $\mathbf{K_{xy}}$:

$$\mathbf{K}_{g,e} = -n_{x,e}\mathbf{K}_x - n_{y,e}\mathbf{K}_y - n_{xy,e}\mathbf{K}_{xy} \tag{3.57}$$

Thermomechanical Buckling

Equation 3.57 shows that the critical buckling load depends on the stress state of the structure. For thermomechanical load applications both mechanical and thermal stresses attribute to the total stress state. Therefore the eigenvalue problem is given by:

$$\left(\mathbf{K}_m - \lambda_{\mathrm{M}}\mathbf{K}_g^{\mathrm{M}} - \lambda_{\mathrm{Th}}\mathbf{K}_g^{\mathrm{Th}}\right)\mathbf{a} = 0 \tag{3.58}$$

The geometric stiffness is decomposed in mechanical and thermal terms with corresponding load multipliers λ_M and λ_{Th}. There are two unknowns in this formulation, thus it cannot be solved directly. There are two possibilities to assess the posed eigenvalue problem. The first possibility is to assume either the mechanical or thermal load to be constant and check whether this load is stable. If the sub-problem is stable the total buckling problem can be assessed. If for example the structure is subject to a thermal load due to curing the thermal buckling problem is assessed first to check for stability. This assessment is then proceeded by the total buckling analysis.

The second possibility is to scale both thermal and mechanical load by the same load multiplier. The buckling problem formulation is then given by:

$$\left(\mathbf{K}_m - \lambda\mathbf{K}_g^{\mathrm{M}} - \lambda\mathbf{K}_g^{\mathrm{Th}}\right)\mathbf{a} = \left[\mathbf{K}_m - \lambda\left(\mathbf{K}_g^{\mathrm{M}} + \mathbf{K}_g^{\mathrm{Th}}\right)\right]\mathbf{a} = 0 \tag{3.59}$$

The influence of the buckling formulation is illustrated in Figure 3.7. The magnitude of the safety margin of a design depends on the chosen buckling formulation. For the first option one of the loads is set to be constant, in this example $\lambda_{TH} = 1$, and the safety margin is determined by the critical mechanical load multiplier. If both mechanical and thermal load are scaled by the same load factor the safety margin becomes different and depends on both load multipliers.

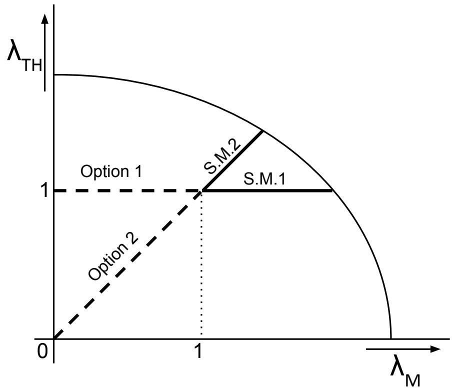

Figure 3.7: For option 1 either the thermal or mechanical load is assumed to be constant (in this illustration the thermal load). For option 2 both loads are scaled by the same multiplier. The safety margin depends on the chosen buckling formulation. Note that the curve is not a representation of reality due to shifting buckling modes during optimization.

It depends on the optimization problem statement which formulation is suitable. If the objective is to maximize the safety margin the chosen formulation will influence the design. If buckling is a constraint the buckling formulation is not of an influence. The constraint only checks whether buckling occurs or not. As is depicted in the figure for both buckling formulations both load multipliers have to be larger than 1.

In the aerospace industry buckling is often a constraint rather than an objective. In this work Equation 3.59 is implemented for practical reasons. Only a single calculation is necessary to determine how close to buckling the structure is. By adjusting the mechanical and thermal loads the influence on the buckling performance can be further studied.

3.6. Implementation in the Framework

The framework presented in this work only considers symmetric laminate to avoid bending-extension coupling, i.e. the B-matrix is zero. Due to symmetry the ply angles and densities of only half the stack are required to fully determine the laminate stacking sequence.

Optionally the laminate can be set to be balanced to avoid shear-extension coupling, i.e. $A_{16} = A_{26} = 0$. Consequently only a fourth of the ply angles and densities is needed to acquire the lay-up. If stacks are given as a balanced laminate the symmetric part of the laminate is generated by the following linking formulation:

$$\boldsymbol{\theta}_s = \mathbf{L}_\theta \cdot \boldsymbol{\theta}_d \tag{3.60}$$

$$\boldsymbol{\rho}_s = \mathbf{L}_\rho \cdot \boldsymbol{\rho}_d \tag{3.61}$$

In this report balanced layers are assumed to be adjacent to limit the effect on values D_{16} and D_{26}. Hence the following linking matrices are implemented:

$$\mathbf{L}_\theta = \begin{bmatrix} 1 & & & 0 \\ -1 & & & \\ & 1 & & \\ & -1 & & \\ & & & \ddots \\ 0 & & & \ddots \end{bmatrix} \qquad \mathbf{L}_\rho = \begin{bmatrix} 1 & & & 0 \\ 1 & & & \\ & 1 & & \\ & 1 & & \\ & & & \ddots \\ 0 & & & \ddots \end{bmatrix} \tag{3.62}$$

Based on the ply angles and ply densities the nodal properties are calculated. First the lamination parameters and its first and second order derivative are calculated for the k-th layer:

$$\mathbf{V}_k = \begin{bmatrix} 1 \\ \cos 2\theta_k \\ \sin 2\theta_k \\ \cos 4\theta_k \\ \sin 4\theta_k \end{bmatrix} \qquad \frac{d\mathbf{V}_k}{d\theta_k} = \begin{bmatrix} 0 \\ -2\sin 2\theta_k \\ 2\cos 2\theta_k \\ -4\sin 4\theta_k \\ 4\cos 4\theta_k \end{bmatrix} \qquad \frac{d^2\mathbf{V}_k}{d\theta_k^2} = \begin{bmatrix} 0 \\ -4\cos 2\theta_k \\ -4\sin 2\theta_k \\ -16\cos 4\theta_k \\ -16\sin 4\theta_k \end{bmatrix} \tag{3.63}$$

To ease the density optimization these are obtained slightly different from the equations given beforehand. Two terms are introduced for the k-th layer:

$$I_0^k = \rho_k \tag{3.64}$$

$$I_2^k = I_0 \frac{z_k^2 + z_{k-1} z_i + z_{k-1}^2}{3} \tag{3.65}$$

With the lamination parameters, densities, ply thicknesses and material invariants the stiffness matrices and thermal load for the k-th layer can be computed. The nodal stiffness and thermal load is obtained by summation of the layer properties, where the summation is over the number of symmetric layers s:

$$\begin{aligned}
\mathbf{A}_k &= \underbrace{2 \cdot I_0^k \cdot t_k^0 \cdot \mathbf{U}}_{\mathbf{L}_k^A} \cdot \mathbf{V}_k & \rightarrow \quad \mathbf{A}_n &= \sum_k^s \mathbf{A}_k \\
\mathbf{D}_k &= \underbrace{2 \cdot I_2^k \cdot t_k^0 \cdot \mathbf{U}}_{\mathbf{L}_k^D} \cdot \mathbf{V}_k & \rightarrow \quad \mathbf{D}_n &= \sum_k^s \mathbf{D}_k^0 \\
\mathbf{N}_k^{Th} &= \underbrace{2 \cdot I_0^k \cdot t_k \cdot \mathbf{K}}_{\mathbf{L}_k^{Th}} \cdot \mathbf{V}_k \cdot \Delta T & \rightarrow \quad \mathbf{N}_n^{Th} &= \sum_k^s \mathbf{N}_k^{Th}
\end{aligned} \tag{3.66}$$

where n denotes the node. Since only symmetric laminates are considered the doubling multiplier indicates that only the symmetric part of the laminate has to be evaluated.

First and Second Order Derivatives:
During optimization the derivatives of the nodal properties with respect to the fiber orientation and ply density are required. The first order fiber angle derivatives for the k-th ply are obtained by:

$$\begin{aligned}
\frac{\partial \mathbf{A}}{\partial \theta_k} &= \frac{d\mathbf{A}}{d\mathbf{V}_k} \cdot \frac{d\mathbf{V}_k}{d\theta_k} &= \mathbf{L}_k^A \cdot \frac{d\mathbf{V}_k}{d\theta_k} \\
\frac{\partial \mathbf{D}}{\partial \theta_k} &= \frac{d\mathbf{D}}{d\mathbf{V}_k} \cdot \frac{d\mathbf{V}_k}{d\theta_k} &= \mathbf{L}_k^D \cdot \frac{d\mathbf{V}_k}{d\theta_k} \\
\frac{\partial \mathbf{N}^{Th}}{\partial \theta_k} &= \frac{d\mathbf{N}^{Th}}{d\mathbf{V}_k} \cdot \frac{d\mathbf{V}_k}{d\theta_k} &= \mathbf{L}_k^{Th} \cdot \frac{d\mathbf{V}_k}{d\theta_k} \cdot \Delta T
\end{aligned} \tag{3.67}$$

The second order derivatives are obtained in a similar fashion using the second order derivative of the lamination parameters. The practical relevance of the introduced I_0 and I_2 terms become apparent when taking the density derivatives:

$$\frac{dI_0^k}{d\rho_k} = 1 \tag{3.68}$$

$$\frac{dI_2^k}{d\rho_k} = \frac{z_k^2 + z_{k+1} z_i + z_{k+1}^2}{3} \tag{3.69}$$

Applying the chain rule the density derivative of the nodal properties can now easily be determined:

$$\begin{aligned}
\frac{\partial \mathbf{A}}{\partial \rho_k} &= \frac{d\mathbf{A}}{dI_0^k} \cdot \frac{dI_0^k}{d\rho_k} &= 2 \cdot \frac{dI_0^k}{d\rho_k} \cdot t_k \cdot \mathbf{U} \cdot \mathbf{V}_k \\
\frac{\partial \mathbf{N}^{Th}}{\partial \rho_k} &= \frac{d\mathbf{N}^{Th}}{dI_0^k} \cdot \frac{dI_0^k}{d\rho_k} &= 2 \cdot \frac{dI_0^k}{d\rho_k} \cdot t_k \cdot \mathbf{K} \cdot \mathbf{V}_k \cdot \Delta T
\end{aligned} \tag{3.70}$$

For the flexural stiffness matrix **D** the density derivative is more complicated. The change in density of a specific layer also influences the z-values of the layers placed on top, thus further influencing the D-matrix. The local effect of a change in density is captured in the first term and the change in z-values of the layer itself and the layers placed on top are included in the second and third terms:

$$\begin{aligned}
\frac{\partial \mathbf{D}}{\partial \rho_k} &= \frac{d\mathbf{D}}{dI_2^k} \cdot \frac{dI_2^k}{d\rho_k} + \sum_{i=1}^{k} \frac{d\mathbf{D}}{dI_2^i} \cdot \frac{dI_2^i}{d\rho_k} \\
&= 2 \cdot \frac{dI_2^k}{d\rho_k} \cdot t_k^0 \cdot \mathbf{U} \cdot \mathbf{V}_k + 2 \cdot \sum_{i=1}^{k-1} \rho_i \cdot \frac{2 \cdot z_i + z_{i-1}}{3} \cdot t_i^0 \cdot \mathbf{U} \cdot \mathbf{V}_i + 2 \cdot \sum_{i=1}^{k} \rho_i \cdot \frac{z_i + 2 \cdot z_{i-1}}{3} \cdot t_i^0 \cdot \mathbf{U} \cdot \mathbf{V}_i
\end{aligned} \tag{3.71}$$

Symmetry is already taken into account in the derivatives. During optimization only the design layers are considered, hence if balanced conditions are used the derivatives of the symmetric layers have to be mapped back to the design layers by the linking matrices given by Equation 3.62.

4

Multi-Step Framework

The optimization scheme depends on the chosen parameterization method. Over the years many different approaches have been introduced and demonstrated and some of these are mentioned in chapter 2. Specifically useful is the multi-step approach used by IJsselmuiden, which code is available at the Aerospace Structures and Materials department of the Aerospace Engineering faculty of Delft University of Technology. The 3-step approach is illustrated in Figure 4.1 and tackles the design problem in the following order:

Step 1 - Optimize the design problem to determine the optimum lamination parameter distribution.
Step 2 - Retrieve the corresponding stacking sequence taking curvature constraints into account.
Step 3 - Determine the corresponding fiber paths.

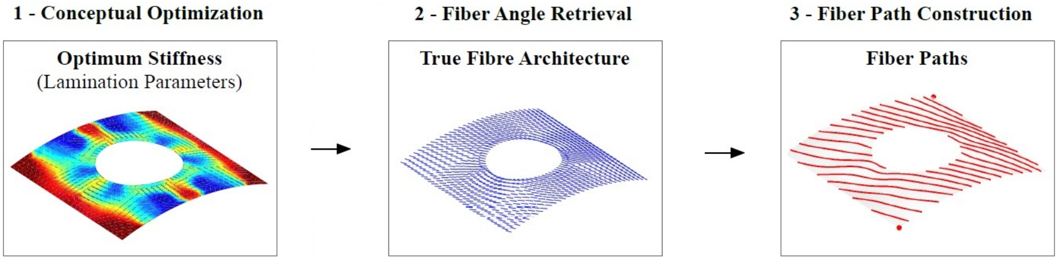

Figure 4.1: The 3-step design approach based on parameterization by lamination parameters. From IJsselmuiden (2011) [18]

Peeters added sub-approximations in fiber angle space to the multi-step framework. This approach functions as an alternative retrieval step and makes it possible to optimize in the fiber angle design space to find the true optimum fiber angle distribution.

In the first three sections the multi-step framework from IJsselmuiden will be explained step by step. The influence of thermal loads is added to the optimization routine in the first step of the framework to allow for thermomechanical optimization. The extension by Peeters is elaborated in section 4.4 and thermal influences are added. Section 4.5 provides a work flow diagram to explain how composite laminate analysis, the optimization step and sub-approximations come together in the optimization routine. At last several structural responses will be given to fit in the optimization framework in section 4.6.

4.1. Step 1 - Conceptual Optimization

The first step solves the optimization problem to find the optimal lamination parameter distribution. Before explaining how this is achieved the general optimization problem will be stated first. The next two sections will explain the method of sequential local approximations and the conservative convex separable approximation. These successive approximation methods are used to solve the optimization problem in lamination parameter space by means of a dual and bound formulation.

4.1.1. Optimization Formulation

A general optimization formulation is presented by Equation 4.1. In this work minimization of f is used as the optimization objective. The objective normally represents a structural response, such as buckling, stiffness, strength or weight. Structural responses can also be used as constraint g to the optimization problem. The optimization problem can also be subject to other constraints such as established design rules. The behavior of the structural responses and constraints determine what optimization scheme is suitable to tackle the problem. This behavior is influenced by the chosen parameterization and corresponding set of design variables **x**. The design parameters do not only influence the response behavior but also indicate whether the parameter space is continuous, discontinuous or contains a discrete variation.

$$\begin{array}{lll} \min & f(\mathbf{x}) & \\ \text{s.t.} & g_j(\mathbf{x}) \leq 0 & \text{for} \quad j = 1 \ldots m \\ & x_i^L \leq x_i \leq x_i^U & \text{for} \quad i = 1 \ldots n \end{array} \tag{4.1}$$

Convexity is necessary to ensure global optima [85]. A well-behaved convex design problem is defined by a convex objective function for minimization and has a convex feasible design region. A convex objective function is best explained for a 2-dimensional problem statement. A function is strictly convex if a line between any two points of the response lays above the original function. This is illustrated by Figure 4.2 (left) and the mathematically relation is given by:

$$f\left[\mathbf{x}_2 \cdot \alpha + \mathbf{x}_1 \cdot (1-\alpha)\right] \leq \alpha \cdot f(\mathbf{x}_2) + (1-\alpha) f(\mathbf{x}_1), \quad \text{for} \quad 0 \leq \alpha \leq 1. \tag{4.2}$$

This relation implies that there is non-negative curvature, i.e. the second derivative is larger than zero. It is also possible to have a non-strictly convex function. In this case there exists a line connecting two points on the function curve that lies on the curve itself, i.e. the function curve contains a straight segment with a second derivative that equals zero. For a set of n variables function f is convex if the matrix of second derivatives (referred to as the Hessian) is positive semi-definite. Function f is strictly convex if the matrix of second derivatives is positive definite.

The feasible region of set **S** is convex if a line connecting any design vectors in **S** is also in **S**. This is illustrated in Figure 4.2 (right) and the mathematical relation is given by:

$$\mathbf{x}_1, \mathbf{x}_2 \in \mathbf{S}, \quad \mathbf{x}_1 \cdot \alpha + \mathbf{x}_2 \cdot (1-\alpha) \in \mathbf{S} \quad \text{for} \quad 0 \leq \alpha \leq 1 \tag{4.3}$$

Furthermore the design space is related to the constraints, to have a convex feasible region inequality constraints have to be convex and equality constraints have to be linear.

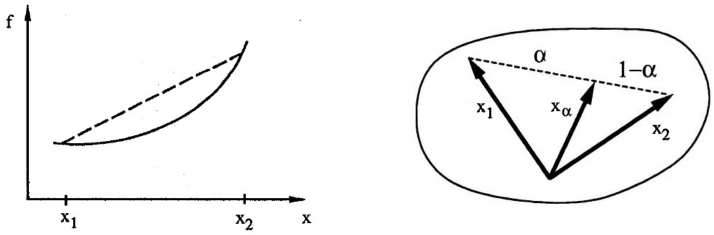

Figure 4.2: Convex objective function (left) and convex feasible design region (right). From Grenestedt and Gudmundson (1993) and from Haftka and Gurdal (1992) [56, 85].

4.1.2. Sequential Local Approximations

Global approximations try to approximate the response accurately for the entire design space and are most commonly related to response surface approaches [85]. A design of experiments is performed to obtain the response for given sets of design variables, thereafter curve fitting techniques are applied to obtain a global approximation. A global approximation can be applied to structural responses and many evaluations are required to accurately approximate the global response. For large amounts of nodes and elements the finite

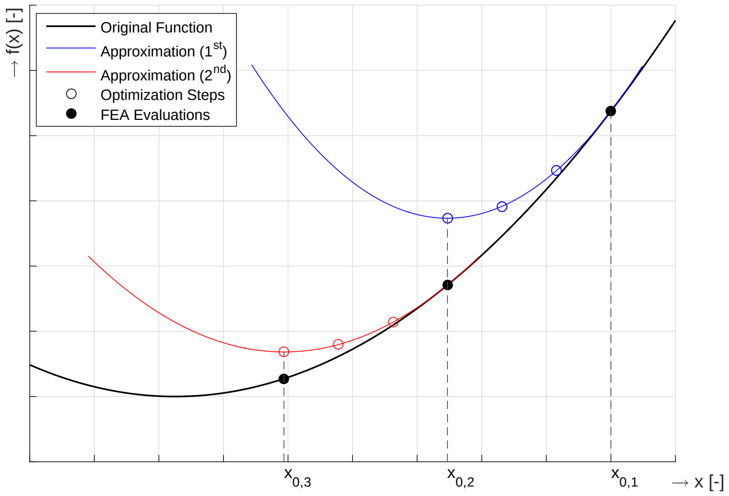

Figure 4.3: Method of sequential/successive local approximations. Using local approximations the number of FEA evaluations is reduced. In the figure only three FEA evaluations are used to reach $x_{0,3}$ which is already close to the global optimum. Using an optimization scheme based on global approximations could significantly increase this number.

element analysis routine to calculate the structural responses dominates the computational demand compared to the computational demand of the optimization procedure. For this reason global approximations are inefficient and often avoided.

To reduce the amount of finite element iterations sequential local function approximations are often applied in structural optimization [59, 85, 86]. The original design problem is replaced by an explicit local approximate design problem based on a single finite element analysis iteration. This local approximation is used to obtain the optimum which in turn will be used to update the original problem which leads to a new local approximation. Hence such methods are called successive or sequential local approximate optimization and this approach is illustrated in Figure 4.3. Such methods reduce the amount of finite element iterations, thus speeding up the optimization process. The simplest form of a local approximation is the linear Taylor series expansion, given by [85]:

$$f_A = f(\mathbf{x}_0) + \sum_{i=1}^{n} \left(\left. \frac{\partial f}{\partial x_i} \right|_0 (x_i - x_{0i}) \right) \tag{4.4}$$

where f_A is approximate response function, f is the actual response, $\mathbf{x}_0$ is the approximate point and n is the number of design variables. For certain responses linear approximations are not accurate. Adding higher order derivatives improves accuracy, but are computationally demanding. As an alternative intervening variables can be used to improve the accuracy. Popular is the reciprocal variable leading to the reciprocal approximation given by [85]:

$$f_A = f(\mathbf{x}_0) + \sum_{i=1}^{n} \left(\left. \frac{\partial f}{\partial x_i} \right|_0 \frac{x_{0i}}{x_i} (x_i - x_{0i}) \right) \tag{4.5}$$

It depends on the response behavior what approximation yields the most accurate representation. A combination of both is also possible and is called the conservative or hybrid approximation given by Equation 4.6 [85]. An approximation is considered conservative if $f_A > f$ for all possible set of design variables. This effectively means that the optimization always improves the objective function and the optimization is globally convergent, this is explained by Figure 4.4. Conservativeness for the hybrid approximation is true if Equation 4.7 holds, which selects the most conservative of the linear and reciprocal formulations.

$$f_A = f(\mathbf{x}_0) + \sum_{i=1}^{n} \left[\delta_i \left(\left. \frac{\partial f}{\partial x_i} \right|_0 (x_i - x_{0i}) \right) + (1 - \delta_i) \left(\left. \frac{\partial f}{\partial x_i} \right|_0 \frac{x_{0i}}{x_i} (x_i - x_{0i}) \right) \right] \tag{4.6}$$

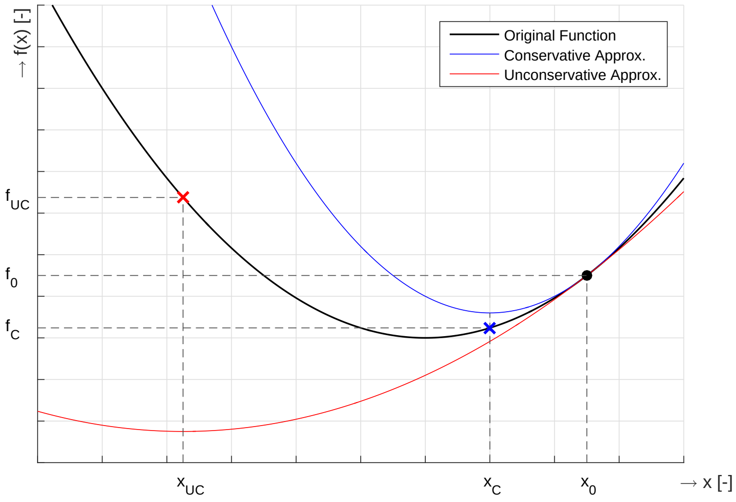

Figure 4.4: The conservative approximation (blue) always yields and improvement in the objective function, i.e. $f_c < f_0$. Althought it is possible for an unconservative approximation (red) to yield an improvement step, it is not guaranteed and therefore global convergence cannot be guaranteed. In this case $f_{uc} > f_0$. From Peeters (2016) [77].

$$\delta_i = \begin{cases} 1 & \text{for} \frac{\partial f}{\partial x_i} \geq 0 \\ 0 & \text{otherwise} \end{cases} \tag{4.7}$$

All three approximations are convex, using them on the constraints and the objective function will yield a convex design problem. Thereby the approximations have the characteristic to be separable, that is [85]:

$$f(\mathbf{x}) = \sum_{i=1}^{N} f_i(x_i) \tag{4.8}$$

$$g_j(\mathbf{x}) = \sum_{i=1}^{N} g_{j,i}(x_i) \quad \text{for} \quad j = 1 \ldots m \tag{4.9}$$

This is advantageous if both the objective function and constraints are separable, since the approximation and the optimization can be evaluated and executed at nodal level i. Furthermore if a second order approximation would be applied to increase accuracy, no mixed partial derivatives between nodes need to be taken and only the diagonal of the Hessian is evaluated [87].

4.1.3. Conservative Convex Separable Approximation

In 2002 Svanberg introduced a conservative convex separable approximation (CCSA) method [61]. This method is suitable to solve problems with many design variables. Due to separability the problem can be approximated by a set of convex subproblems and the conservativeness guarantees global convergence. The general form of the approximation is given by:

$$f_C(\mathbf{x}) = f_A(\mathbf{x}) + \zeta f_D(\mathbf{x}) \tag{4.10}$$

The first term $f_A(\mathbf{x})$ is the local approximation and has the same function value and gradient at the local approximate point $\mathbf{x}_0$ as the original objective function. The second term $\zeta f_D(\mathbf{x})$ ensures conservativeness and can also be used to ensure convexity if necessary. Within this work this term is referred to as damping. The following should be true to conform with the CCSA methodology:

1. Functions f_A and f_D have to be continuous. They must be separable and differentiable twice with continuous derivatives.

2. The value and gradient of f_A must equal the original function. Therefore the value and gradient of f_D have to be zero at the approximate point to not interfere with the local approximation.
3. The Hessian of f_A must be positive semi-definite. This means the approximation is not required to be strictly convex.
4. The Hessian of f_D must be positive definite. Therefore this term functions as convexifying term to ensure a strictly convex approximation f_C.

Based on the advantages of CCSA proposed by Svanberg IJsselmuiden *et al* derived a generic approximation form for structural responses to comply with variable stiffness optimization. A modified conservative approximation is used for the local approximation f_A. Instead of using the δ-term to select between the linear an reciprocal terms the physical response behavior is studied to determine whether the linear, reciprocal or combination of both terms should attribute to the approximation. In general form the local approximation is given by [18, 60]:

$$f_A = f(\mathbf{x}_0) + \sum_{i=1}^{N} \left(\left. \frac{\partial \hat{f}}{\partial x_i} \right|_0 (x_i - x_{0i}) + \left. \frac{\partial \tilde{f}}{\partial x_i^{-1}} \right|_0 \left(x_i^{-1} - x_{0i}^{-1} \right) \right) \tag{4.11}$$

For composite laminate analysis the ABD-matrix is directly related to structural responses. Design variable $\mathbf{x}$ can be considered to contain the stiffness terms related to the structural response of interest. Thus the approximated response f_A can be given as [63]:

$$f_A = \hat{f} + \sum_{i=1}^{N} \left[\frac{\partial \hat{f}}{\partial \mathbf{A}_i} : \left(\mathbf{A}_i - \hat{\mathbf{A}}_i \right) + \frac{\partial \hat{f}}{\partial \mathbf{D}_i} : \left(\mathbf{D}_i - \hat{\mathbf{D}}_i \right) + \frac{\partial \hat{f}}{\partial \mathbf{A}_i^{-1}} : \left(\mathbf{A}_i^{-1} - \hat{\mathbf{A}}_i^{-1} \right) + \frac{\partial \hat{f}}{\partial \mathbf{D}_i^{-1}} : \left(\mathbf{D}_i^{-1} - \hat{\mathbf{D}}_i^{-1} \right) \right] + C_0 \tag{4.12}$$

in which N represents the number of nodes or elements and $\mathbf{A}_i$ and $\mathbf{D}_i$ are the corresponding stiffness matrices. The hat-accent denotes the values at the approximate point. C_0 includes all remaining constant terms and can be used to enforce homogeneity. The : operator is a matrix contraction and is the Fobrenius inner product or trace, i.e. $\mathbf{A} : \mathbf{B} = \sum A_{ij} B_{ij}$. By Euler's theorem for homogeneous functions the approximation can be simplified to the form [18, 63]:

$$f_A = \sum_{i=1}^{N} \left(\left. \boldsymbol{\Psi}_i^m \right|_0 : \mathbf{A}_i + \left. \boldsymbol{\Psi}_i^b \right|_0 : \mathbf{D}_i + \left. \boldsymbol{\Phi}_i^m \right|_0 : \mathbf{A}_i^{-1} + \left. \boldsymbol{\Phi}_i^m \right|_0 : \mathbf{D}_i^{-1} \right) + C_0 \tag{4.13}$$

where the $\boldsymbol{\Phi}^{m,b}$ and $\boldsymbol{\Psi}^{m,b}$ terms are the stiffness sensitivity tensors given by:

$$\boldsymbol{\Psi}_i^m = \frac{\partial \hat{f}}{\partial \mathbf{A}_i} \tag{4.14}$$

$$\boldsymbol{\Psi}_i^b = \frac{\partial \hat{f}}{\partial \mathbf{D}_i} \tag{4.15}$$

$$\boldsymbol{\Phi}_i^m = \frac{\partial \tilde{f}}{\partial \mathbf{A}_i^{-1}} \tag{4.16}$$

$$\boldsymbol{\Phi}_i^b = \frac{\partial \tilde{f}}{\partial \mathbf{D}_i^{-1}} \tag{4.17}$$

Assessing the second variation of the approximation IJsselmuiden proved that sensitivities $\boldsymbol{\Phi}^{m,b}$ have to be positive semi-definite to ensure that the response function has non-negative curvature, which is required for convexity. Thus the convexity of the approximation depends on the derivatives of the response with respect to the $\mathbf{A}^{-1}$ and $\mathbf{D}^{-1}$ matrices.

When thermal load applications are considered the structural responses are influenced by the thermal loads. According to the thermal analysis in section 3.4 a change in laminate design will change the exerted thermal loads accordingly. To capture this behavior a term is added to the approximation:

$$f_A = \sum_{i=1}^{N} \left(\left. \boldsymbol{\Psi}_i^m \right|_0 : \mathbf{A}_i + \left. \boldsymbol{\Psi}_i^b \right|_0 : \mathbf{D}_i + \left. \boldsymbol{\Phi}_i^m \right|_0 : \mathbf{A}_i^{-1} + \left. \boldsymbol{\Phi}_i^m \right|_0 : \mathbf{D}_i^{-1} + \left. \boldsymbol{\eta}_i \right|_0 \cdot \Delta \mathbf{N}_i^{th} \right) + C_0 \tag{4.18}$$

where $\boldsymbol{\eta}$ is the thermal sensitivity tensor:

$$\boldsymbol{\eta}_i = \frac{\partial \hat{f}}{\partial \mathbf{N}^{th}} \tag{4.19}$$

Note that the thermal moment is not added since only symmetric laminates are considered and the through thickness temperature gradient is assumed to be zero in this work.

Lamination Parameters

For generality the approximation is related to the stiffness matrices and change in thermal load. Different parameterizations can be applied to the general approximation by sub-approximations, referred to as level-2 approximations in this work. Lamination parameters are specifically chosen in the work of IJsselmuiden to reduce the number of design variables and to limit the design space. Lamination parameters are linearly related to the stiffness matrices and thermal load. Therefore the general approximation can directly be expressed by the lamination parameter design variables while the convex properties are retained. This results in a well-behaved optimization problem.

To use fiber angles as design parameters the level-2 sub-approximation becomes more complicated, since fiber angles are not linearly related to the stiffness matrices. In section 4.4 optimization in the fiber angle design space will be discussed.

Thickness Optimization

Since the general formulated approximation is given in terms of stiffness it is possible to consider thickness as an additional design variable. The combination of lamination parameters and thickness does not yield a linear relation with stiffness. Therefore adjustments to the general approximations are made to include a thickness term in the approximation. For the sake of brevity this is not repeated in this work, for details the reader is referred to the work of IJsselmuiden [18].

Damping Term

Guaranteed conservativeness is lost due to the modified approximation. In early studies by IJsselmuiden *et al* the proximal point algorithm by Rockafellar is applied in lamination parameter space [18, 63, 64]. In essence this approach uses a move limit on the iteration step to create a conservative approximation. However, a more general damping term is sought for in the stiffness space so it is free to choose any parameterization that leads to the stiffness matrices. Applying the CCSA method by Svanberg the convexity term $\zeta f_D(x)$ scales dynamically throughout the optimization algorithm, thus improving convergence. A damping function is derived and given by Equation 4.20.

$$f_D = \sum_{i=1}^{N} w_i \left(\mathbf{A}_{0,i}^{-1} : \mathbf{A}_i + \mathbf{D}_{0,i}^{-1} : \mathbf{D}_i + \mathbf{A}_{0,i} : \mathbf{A}_i^{-1} + \mathbf{D}_{0,i} : \mathbf{D}_i^{-1} - 4\mathbf{I} : \mathbf{I} \right) \tag{4.20}$$

The last term is required to ensure a function value of zero at the approximate point, therefore f_D fulfills the four requirements imposed by Svanberg to conform with the CCSA framework. The weight factor w_i scales the contributing of the separable terms. The separable terms are represented by the nodes and elements of the discretized structure, therefore their corresponding area fraction is used as weight factor. For thermal load applications the damping function does not have to be updated since the thermal term in Equation 4.18 is linearly dependent on the thermal loads. Since the form of the damping function equals the local approximation it allows for easy implementation in the optimization routine by adjusting the sensitivities by:

$$\check{\mathbf{\Psi}}_i^m\big|_0 = \mathbf{\Psi}_i^m\big|_0 + \zeta w_i \mathbf{A}_{0,i}^{-1} \tag{4.21}$$

The same holds for the other stiffness sensitivities and the constant damping term $-4\zeta\mathbf{I} : \mathbf{I}$ is captured as a constant in C_0. To complete the conservative approximation ζ has to be determined, which is a dynamic scalar to allow for adaptive damping. Based on a move limit in stiffness space the initial damping factor is obtained and applied to all local responses, where non-zero condition is enforced by triangular inequality. The initial damping factor is used for all responses and is given by Equation 4.22, where m represents the number of structural responses that are considered. The derivation is specified by IJsselmuiden [18].

$$\zeta^2 = \sum_{j=0}^{m} \sum_{i=1}^{N} \frac{w_i}{2} \left(\left(|| \mathbf{\Psi}_{i,j}^m \mathbf{A}_i || + || \mathbf{\Phi}_{i,j}^m \mathbf{A}_i^{-1} || \right)^2 + \left(|| \mathbf{\Psi}_{i,j}^b \mathbf{D}_i || + || \mathbf{\Phi}_{i,j}^b \mathbf{D}_i^{-1} || \right)^2 \right) \tag{4.22}$$

It is advantageous to use separate damping for responses to improve convergence rates. The damping factor is updated every iteration for all responses m according to:

$$\zeta_j^{(k+1)} = \gamma^* \zeta_j^{(k)} \quad \text{for} \quad j = 1...m \tag{4.23}$$

Damping needs to be added if the approximate function is unconservative to ensure global convergence. Furthermore damping is used to influence the convergence rate of the optimization problem. Convergence rates are sped up by fast increments in damping for unconservative approximations to quickly arrive at approximations that are more likely to yield an improvement step. If an approximation is too conservative only small improvement steps are made, hence relaxation of damping is included to arrive at approximations that yield larger step sizes. The update factor γ is calculated by an exponential function given in Equation 4.24. This allows for fast increments in damping for unconservative approximations.

$$\gamma = \exp\left[\frac{f_j^{(k+1)} - f_{A,j}^{(k+1)}}{f_{D,j}^{(k+1)}}\right] \tag{4.24}$$

Furthermore the update factor is subject to bound limits to obtain the update factor γ^* given by Equation 4.25. The limits are based on experience and set arbitrary by IJsselmuiden and are determined by the following template:

$$\gamma^* = \begin{cases} \gamma^-_{min} & \text{if} \quad \gamma \leq \gamma^-_{min} \\ \gamma & \text{if} \quad \gamma^-_{min} < \gamma < 1 \\ \gamma^+_{min} & \text{if} \quad 1 \leq \gamma \leq \gamma^+_{min} \\ \gamma & \text{if} \quad \gamma^+_{min} < \gamma < \gamma^+_{max} \\ \gamma^+_{max} & \text{if} \quad \gamma \geq \gamma^+_{max} \end{cases} \tag{4.25}$$

$$\gamma^-_{min} = 0.95 \qquad \gamma^+_{min} = 1.05 \qquad \gamma^+_{max} = 2.00 \tag{4.26}$$

The set limits allow for fast increments in damping for unconservative approximations but only gradual relaxation if the approximation is conservative.

4.1.4. Optimization by Dual and Bound Formulation

Within the work of IJsselmuiden a combination of the dual and bound formulation is used to reformulate the optimization problem in an effort to simplify the optimization routine [18]. Dual methods divide the constrained optimization problem in local and global optimization problems. Dual methods are advantageous for optimization problems with many variables and few constraints, and therefore suitable to optimize discretized structural design problems [85]. Falk generalized dual methods to structural optimization and Fleury successfully specialized the formulation to separable problems. For the constrained optimization problem stated by Equation 4.1 f is the structural response objective and g_j are the constrained structural responses. By Karush-Kuhn-Tucker conditions a Lagrangian function is formulated as:

$$\mathscr{L}\left(\mathbf{x}, \boldsymbol{\mu}\right) = \mu^f f\left(\mathbf{x}\right) + \sum_{j=1}^{m} \mu_j^g g_j\left(\mathbf{x}\right) \tag{4.27}$$

where μ are the dual variables subject to $\mu^f = 1$ for the objective function and $\mu_j^g \geq 0$ for the constraints. The introduction of the dual variables allow to split the optimization problem. Based on the Lagrangian function the optimization of the dual variables is stated by the dual formulation:

$$\max_{\boldsymbol{\mu}} \mathscr{L}_C\left(\boldsymbol{\mu}\right) \qquad \text{s.t.} \quad \mu^f = 1 \quad \text{and} \quad \mu_j^g \geq 0 \tag{4.28}$$

where $\mathscr{L}_C$ is Falk's dual Lagrangian which expresses the minimization of the Lagrangian in the primal design variables:

$$\mathscr{L}_C = \min_{\mathbf{x}\in C} \mathscr{L}\left(\mathbf{x}\left(\boldsymbol{\mu}\right)\right) \tag{4.29}$$

in which C is a closed convex set of variables. Within this formulation the optimization of the local variable set $\mathbf{x}$ and the global dual variable μ are separated. Both the maximization and minimization are virtually unconstrained, simplifying the optimization problem for separable objective and constraint functions. Furthermore the Lagrangrian is also separable and can be minimized one-dimensionally, therefore $\mathscr{L}_C$ is easily calculated [85]. Haftka and Gurdal demonstrate the usefullness of the dual formulation by an optimization example that uses linear and reciprocal local approximations. This example is given in Chapter 9.2.4 of their book *Elements of Structural Optimization* [85].

For optimization of multi-modal buckling analysis or optimization of a min-max formulation to minimize the maximum failure index a multi-response objective function is commonly formulated. For multi-response optimization the bound formulation introduced by Olhoff can be applied to the optimization formulation [88]:

$$\begin{array}{llll} \min & \beta & & \\ \text{s.t.} & \beta \geq f_k\left(\mathbf{x}\right) & \text{for} & k = 1...o \\ & g_j\left(\mathbf{x}\right) \leq 0 & \text{for} & j = 1...m \\ & x_i^L \leq x_i \leq x_i^U & \text{for} & i = 1...n \end{array} \tag{4.30}$$

where o represents the number of structural responses of interest. Since μ equals 1 for the objective function the Lagrangian is adjusted to Equation 4.31. Falk's dual formulation can now be updated to the form given by Equation 4.32

$$\mathscr{L}\left(\mathbf{x},\boldsymbol{\mu}\right) = \sum_{k=1}^{o} \mu_k^f f_k\left(\mathbf{x}\right) + \sum_{j=1}^{m} \mu_j^g g_j\left(\mathbf{x}\right) + \beta\left[1 - \sum_{k=1}^{o} \mu_k^f\right] \tag{4.31}$$

$$\max_{\boldsymbol{\mu}} \mathscr{L}_C\left(\boldsymbol{\mu}\right) \qquad \text{s.t.} \quad \sum_{k=1}^{o} \mu_k^f = 1 \quad \text{and} \quad \mu_k^f \geq 0,\ \mu_j^g \geq 0 \tag{4.32}$$

With the CCSA framework and the dual-bound formulation the optimization problem is split in local and global optimization problems. Even though the response is influenced by the design parameters at other nodes the local optimization problem allows to minimize the structural response approximation given by Equation 4.18 at nodal level. The convex conservative separable approximation is given in general stiffness form to allow for different parameterizations. In the multi-step approach from IJsselmuiden lamination parameters are chosen as design variables to solve the local optimization problem. In Figure 3.2 it is explained that the lamination parameters are only constrained by the feasible design region, making this parameterization suitable for the dual-bound formulation. Since the first and second derivative of the structural response with respect to the lamination parameters are easily obtained for the approximation the local optimization is optimized by a sequential quadratic programming.

The global optimization problem is stated by Equation 4.32 and is related to find the optimal dual variables. The derivatives of the dual formulation with respect to the dual variables are readily available and a sequential quadratic algorithm can be used to obtain the optimum. However, an interior-point method is implemented within the optimization routine for convergence reasons related to design problems that are subject to additional constraints [18].

4.2. Step 2 - Fiber Orientation Retrieval

Fiber placement machines cannot use lamination parameters as input. Once the optimal lamination parameter distribution is known it is therefore essential to obtain a corresponding fiber angle distribution. The problem is that lamination parameters yield non-unique equivalence to stacking sequences and that the relation is non-convex [65]. Inclusion of manufacturing constraints increases the difficulty of the conversion optimization problem. Steering is given by:

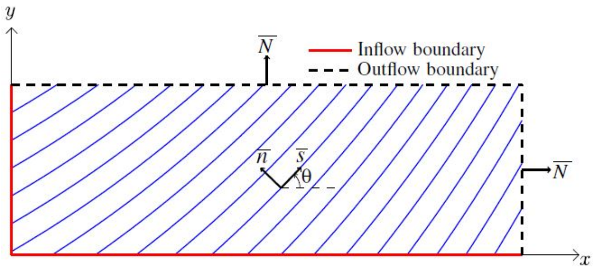

Figure 4.5: Streamlines with inflow and outflow boundaries. $\bar{N}$ are the outward normals of the boundaries and they are used to determined the inflow boundaries by $\bar{s} \cdot \bar{N} \leq 0$. From Blom *et al* (2010) [97].

$$\xi^2 = \frac{2}{\Omega} \cdot \boldsymbol{\theta}^t \cdot \mathbf{L} \cdot \boldsymbol{\theta} \tag{4.33}$$

where ξ is the steering, Ω is the domain and L is the Laplacian of either the element or the total ply. Using the Laplacian of the former leads to local steering and the latter to global steering [77]. The steering limit is inversely related to the minimum steering radius of a Fiber Placement Machine:

$$\xi_{\text{lim}} = \frac{1}{r_{\text{min}}} \tag{4.34}$$

For the conversion problems optimization approaches comparable to least square forms have been applied in different studies [89–91]. In 1998 Todoroki and Haftka were the first to retrieve a stacking sequence by evolutionary genetic algorithms, which proved to be more robust [92]. Later Autio used a similar approach to optimize the conversion [93]. Based on this work Van Campen *et al* derived an algorithm where a genetic algorithm is used to seed a gradient based optimization algorithm to prevent to be trapped in local optima [94, 95]. For a given lamination distribution of a square plate that yields 52% improvement in buckling resistance compared to a constant stiffness design, the algorithm was able to obtain a fiber angle distribution that yields 31% to 47% improvement depending on the number of plies that was used. Irisarri *et al* use a innovative response surface to generate a single surrogate model with an improved Shepard's method [96]. A genetic solver is used to find the optimum. This optimum is used to update the surrogate model, thereafter a new genetic optimization run is performed until global convergence is achieved. This algorithm from Irisarri *et al* is used as the second step in the multi-step framework from IJsselmuiden.

4.3. Step 3 - Fiber Path Construction

The third and last step is to generate fiber paths from the fiber angle distribution. Blom *et al* found an effective way by applying a streamline analogy and it is this analogy that is used for the fiber path construction in the multi-step framework [97]. The stream function is given by:

$$\Psi\left(x, y\right) = C \tag{4.35}$$

which connects all points with constant value C. In the analogy the streamlines represent centerlines of fiber courses, this is illustrated in Figure 4.5. For a given fiber angle distribution the streamlines can be obtained by solving the partial differential equation given by Equation 4.36 subject to specified constraints and boundary conditions. The inflow boundary conditions specify the inflow fiber course distribution, hence they influence the ply coverage. To obtain realistic results Blom optimized the inflow boundary conditions to find a smooth streamline distribution that minimizes either gaps, overlaps or the combination of both.

$$\frac{d\Psi\left(x, y\right)}{ds} = \frac{\partial \Psi}{\partial x}\frac{\partial x}{\partial s} + \frac{\partial \Psi}{\partial y}\frac{\partial y}{\partial s} = \Psi_{,x}\cos\theta + \Psi_{,y}\sin\theta = 0 \tag{4.36}$$

4.4. Different Parameterizations by Level-2 Approximations

The general conservative approximation is given in terms of stiffness to allow for different parameterization approaches, therefore this approximation is referred to as level-1 approximation. For convenience the general form is repeated:

$$f^{(1)} = \sum_{i=1}^{N} \left(\check{\boldsymbol{\Psi}}_i^m\Big|_0 : \mathbf{A}_i + \check{\boldsymbol{\Psi}}_i^b\Big|_0 : \mathbf{D}_i + \check{\boldsymbol{\Phi}}_i^m\Big|_0 : \mathbf{A}_i^{-1} + \check{\boldsymbol{\Phi}}_i^m\Big|_0 : \mathbf{D}_i^{-1} + \check{\boldsymbol{\eta}}_i\Big|_0 \cdot \Delta\mathbf{N}_i^{th} \right) + C_0 \tag{4.37}$$

where the breves indicate the embedded damping within the sensitivities. In the work of IJsselmuiden lamination parameters are used as design variables to define the stiffness properties. Lamination parameters are linearly related to the stiffness matrices and thermal load and can be substituted directly in the level-1 approximation. For parameterization based on fiber angles and ply densities the relation is more complex and implementation is not straight forward. In recent work Peeters derived level-2 approximations with fiber angles and ply densities as design variables [77]. Before explaining how this was done Figure 4.6 illustrates how the level-2 approximations derived by Peeters complement the multi-step approach from IJsselmuiden. With the addition of the level-2 approximation 3 procedures can be followed to optimize a design:

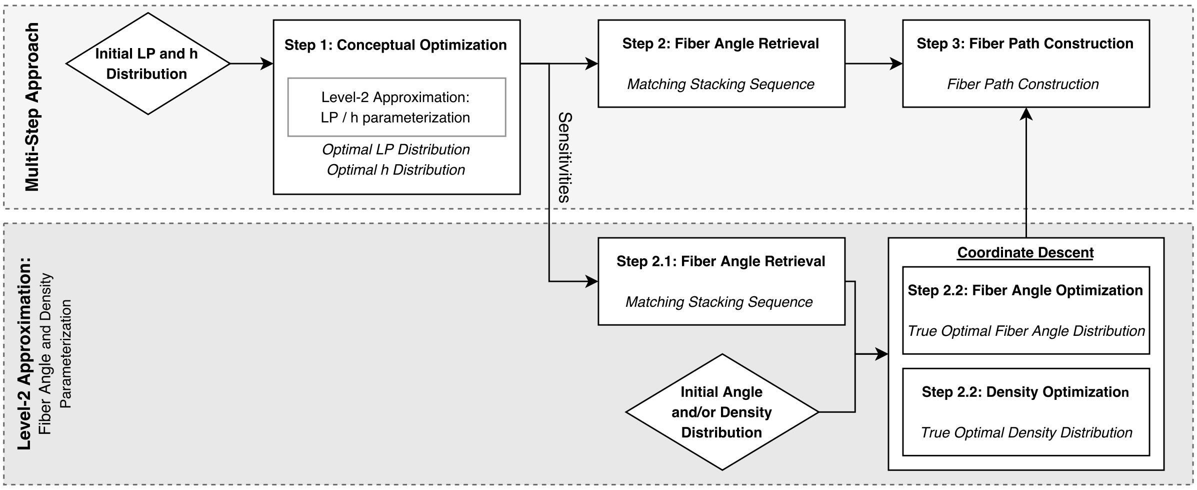

Figure 4.6: Diagram illustrating the combination of the level-2 approximation method and the multi-step approach.

1. The first option is to stick to the original multi-step approach indicated by the light grey block in Figure 4.6. For completeness thickness is also included. Note that although the lamination parameters can be fed into the level-1 approximation directly, this is still a form of a level-2 approximation.

2. The second option is to run the first step of the multi-step approach to use the favorable optimization properties of lamination parameters to determine the corresponding optimal distribution. In section 4.2 the challenge to obtain the best fit in fiber angle distribution was discussed. With the level-2 approximation in the fiber angle design space a corresponding fiber angle distribution can be retrieved if the sensitivities of the optimal design from step-1 are used to build the level-1 approximation. Using the obtained corresponding fiber angle distribution to update the level-1 approximation allows to run additional optimization iterations to obtain a true optimal fiber angle distribution. In Figure 4.6 this is denoted as step-2.2 in the dark grey block. The resulting fiber angle distribution is used to construct the fiber paths in step-3.

   If the optimal thickness distribution is provided density optimization can be added to the optimization problem and a coordinate descent method is used to determine whether the fiber angles or ply densities are updated.

3. As a third option the level-2 approximations with fiber angles and ply densities as design variables can be used for the entire optimization problem. The advantage is that the critical conversion problem is

avoided and the manufacturing constraints on steering are directly used during the entire optimization. However the favorable optimization properties of the lamination parameters are abandoned and more finite element iterations will be needed to update the local approximations of the structural responses. Thereby the routine has to be started from multiple design points to avoid being trapped in local minima that deviate significantly from the global optimum.

To optimize the local approximations in the fiber angle design space a level-2 approximation based on a second order Taylor Series expansion is applied:

$$f^{(2)}\left(\boldsymbol{\theta}\right) = f_0^{(1)} + \mathbf{g} \cdot \Delta\boldsymbol{\theta} + \frac{1}{2}\Delta\boldsymbol{\theta}^t \cdot \mathbf{H} \cdot \Delta\boldsymbol{\theta} \tag{4.38}$$

where $f_0^{(1)}$ is the function value of the level-1 approximation given by Equation 4.37. Vector $\mathbf{g}$ and matrix $\mathbf{H}$ represent the gradient and Hessian of the level-2 function value with respect to the fiber angle design variables at the approximate point. Introducing $\mathbf{s}$, which contains either the membrane or bending stiffness components, the level-2 approximation is given as $f^{(2)}\left(\boldsymbol{\theta}\right) = f^{(1)}\left(\mathbf{s}\left(\boldsymbol{\theta}\right)\right)$. Based on this formulation the gradient based on the stiffness matrices can be determined by the chain-rule:

$$g_i = \frac{\partial f}{\partial \theta_i} = \frac{\partial f^{(1)}}{\partial \mathbf{s}_\alpha}\frac{\partial \mathbf{s}_\alpha}{\partial \theta_i} \tag{4.39}$$

Using the sensitivities and the derivatives given in section 3.6 both terms can be calculated. For the membrane stiffness this yields:

$$\frac{\partial f^{(1)}}{\partial \mathbf{A}} = \boldsymbol{\psi}_i^m - \mathbf{A}^{-1} \cdot \boldsymbol{\phi}_i^m \cdot \mathbf{A}^{-1} \qquad \text{and} \qquad \frac{\partial \mathbf{A}}{\partial \theta_i} = \frac{\partial \mathbf{A}}{\partial \mathbf{V}_i}\frac{\partial \mathbf{V}_i}{\partial \theta_i} \tag{4.40}$$

In a similar fashion the bending stiffness can be used to obtain the corresponding gradient. For thermal load applications a change in the stacking sequence influences the thermal loads. Thus the gradient is complemented with a term dependent on the thermal sensitivity:

$$g_i = g_i^A + g_i^D + g_i^{N^{Th}} \qquad \text{with} \qquad g_i^{N^{Th}} = \frac{\partial f^{(1)}}{\partial \mathbf{N}^{Th}}\frac{\partial \mathbf{N}^{Th}}{\partial \theta_i} = \boldsymbol{\eta}_i \frac{\partial \mathbf{N}^{Th}}{\partial \mathbf{V}_i}\frac{\partial \mathbf{V}_i}{\partial \theta_i} \tag{4.41}$$

The Hessian is given by:

$$H_{ij} = \frac{\partial^2 f^{(1)}}{\partial \theta_i \partial \theta_j} = \underbrace{\frac{\partial^2 f^{(1)}}{\partial \mathbf{s}_\alpha \partial \mathbf{s}_\beta} \cdot \frac{\partial \mathbf{s}_\alpha}{\partial \theta_i} \cdot \frac{\partial \mathbf{s}_\beta}{\partial \theta_j}}_{\text{Gauss-Newton Term}} + \underbrace{\frac{\partial f^{(1)}}{\partial \mathbf{s}_\alpha} \cdot \frac{\partial^2 \mathbf{s}_\alpha}{\partial \theta_i \partial \theta_j}}_{\text{Omitted Term}} \tag{4.42}$$

For the Hessian the last term is omitted since it is does not guarantee to be semi-positive definite and only the Gauss-Newton term is used to ensure a positive semi-definite contribution to the approximation. The thermal term is only linearly expanded in the approximation and thus absent in the Hessian.

The level-2 approximation has to agree with the CCSA framework from Svanberg. A damping function that has the same form as the Hessian term is used to not interfere with the value and gradient at the approximate point and the form of the approximation. The function is given by Equation 4.43, where $\mathbf{H}_D$ is a regularisation matrix. The initial damping factor is given by Equation 4.44, the regularisation matrix and the derivation of the damping factor are specified by Peeters [77]. Since the damping function depends on the Hessian the formulation does not change for thermal load applications.

$$f_D^{(2)}\left(\theta\right) = \frac{1}{2}\Delta\boldsymbol{\theta}^t \cdot \mathbf{H}_D \cdot \Delta\boldsymbol{\theta} \tag{4.43}$$

$$\zeta_\theta^{2^{(2)}} = \frac{1}{2} \cdot \mathbf{g}^t \cdot \mathbf{H}_D^{-1} \cdot \mathbf{g} \tag{4.44}$$

Peeters also added a level-2 approximation related to the density for thickness optimization. The approximation is linearly expanded:

$$f^{(2)}\left(\boldsymbol{\rho}\right) = f_0^{(1)} + \mathbf{g}\cdot\Delta\boldsymbol{\rho} \tag{4.45}$$

where the gradient $\mathbf{g}$ is given by:

$$g_i = \frac{\partial f^{(1)}}{\partial \rho_i} = g_i^A + g_i^D + g_i^{N^{Th}} \tag{4.46}$$

The gradient is calculated in a similar fashion as the gradient of the fiber angle approximation. The density approximation is linearly expanded, hence the damping function does change the form to create a convex approximation. The damping function is given by:

$$f_D^{(2)}\left(\boldsymbol{\rho}\right) = \sum_j^m \sum_{i=1}^N \left(\frac{\rho_i}{\rho_{0,i}} + \frac{\rho_{0,i}}{\rho_i} - 2\right)\cdot w_i \tag{4.47}$$

The derivation of the initial damping factor is specified by Peeters [77] and yields:

$$\zeta_\rho^{2(2)} = \sum_i^N \frac{w_i}{2}\left(\left(\boldsymbol{\Phi}_i^m : \boldsymbol{\Phi}_i^{m^t} + \boldsymbol{\Psi}_i^m : \boldsymbol{\Psi}_i^{m^t}\right)^2 + \left(\boldsymbol{\Phi}_i^b : \boldsymbol{\Phi}_i^{b^t} + \boldsymbol{\Psi}_i^b : \boldsymbol{\Psi}_i^{b^t}\right)^2\right) \tag{4.48}$$

Both fiber angle and density level-2 approximations are optimized by a predictor-corrector primal-dual interior-point solver. The dual formulation used by IJsselmuiden is no longer efficient due to the additional curvature constraints. The optimization algorithm is extensively discussed by Peeters [77]. Optimization of both the fiber angle distribution and thickness is performed by a coordinate descent algorithm.

4.5. Model Work Flow Diagram

A work flow diagram with the level-2 approximations in fiber angle and density space are presented in Figure 4.7. The model starts with different input blocks. In the laminate input the material properties are used to calculate the material invariant matrices **U** and **K**. The initial stacking sequence and density distribution is specified as well. The model input is used to define the finite element model and specifies the boundary and load conditions. For a thermal load application the temperature difference is defined at the nodes. With the model and laminate inputs the nodal and element properties are calculated.

If the optimal lamination parameter distribution is obtained from optimization in lamination parameter space the corresponding sensitivities are used to determine the level-1 approximation. If these sensitivities are not available the finite element model is constructed and the finite element and buckling analysis is performed to determine the responses and sensitivities. If the level-1 approximation is build damping is added, thereafter the level-2 approximations are build.

A coordinate descent methodology is implemented as consensus what parameter is updated. Both the fiber angle and density distribution are optimized. With the newly found distributions the response is approximated by the level-1 approximation. If the response does not yield an improvement the damping function is updated. Note that the damping factor is always updated, even if an improvement is found. This process is iterated until convergence is established for both the fiber angle and density optimization.

Once the optimization routine has converged it is checked what parameter yields the most improvement. The respective parameter will be used to update the level-1 damping factor and to perform FEA. If the FEA does not yield an improvement the level-1 damping function is updated and another iteration of the coordinate descent routine is executed. If an improvement step is made convergence is checked. If convergence is not reached the level-1 approximation is updated and the entire routine is repeated until a optimum solution is established.

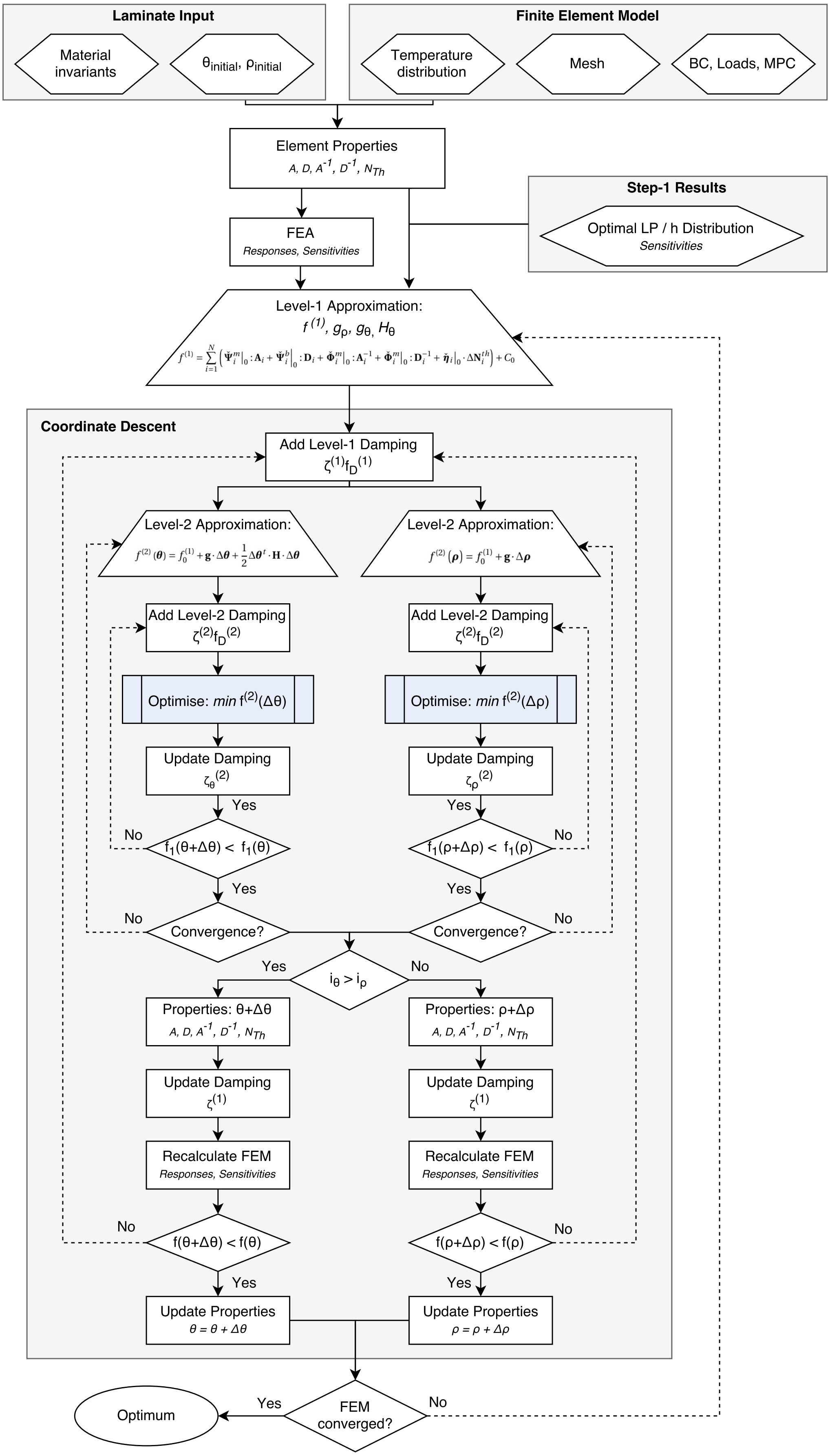

Figure 4.7: Work Flow Diagram of the fiber angle optimization routine. A coordinate descent algorithm is applied to include thickness optimization. Adjusted from Peeters [77].

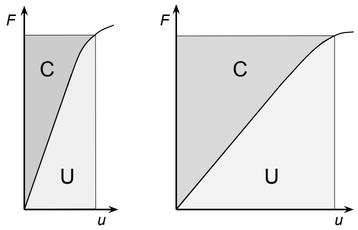

Figure 4.8: Relation of compliance and strain energy to stiffness. Strain energy is given by U and complementary strain energy is indicated as C. Minimizing compliance corresponds to a maximum stiffness design.

4.6. Stiffness Response Approximation

Maximum stiffness is obtained by optimizing for minimum complementary strain energy C, also referred to as compliance and this is explained by Figure 4.8 [58, 65]. The optimization problem is stated as:

$$\min_{\mathbf{x}\in S} C(\mathbf{x}) \tag{4.49}$$

where $\mathbf{x}$ are the design parameters and C is the compliance given by:

$$C_N = \frac{1}{2}\mathbf{N}^t \cdot \mathbf{A}^{-1} \cdot \mathbf{N} \tag{4.50}$$

Taking the derivative of the compliance with respect to an arbitrary parameter b results in the following:

$$\frac{dC_N}{db} = \underbrace{\frac{1}{2}\mathbf{N}^t \cdot \frac{d\mathbf{A}^{-1}}{db} \cdot \mathbf{N}}_{\text{local}} + \underbrace{\mathbf{N}^t \cdot \mathbf{A}^{-1} \frac{d\mathbf{N}}{db}}_{\text{glocal}} \tag{4.51}$$

Working out both terms shows that the global term nullifies, leaving only the local term. This term is not influenced by thermal loads, therefore the general approximation has the following form:

$$C \approx \sum_{i=1}^{N} \boldsymbol{\Phi}_{\boldsymbol{i}}^{\boldsymbol{m}} : \mathbf{A}^{-1} + \boldsymbol{\Phi}_{\boldsymbol{i}}^{\boldsymbol{b}} : \mathbf{D}^{-1} \tag{4.52}$$

The convexity and conservativeness of the total approximation are proven by Setoodeh *et al* and Peeters [58, 77]. Furthermore the approximation is separable and can be evaluated at nodal level. The corresponding sensitivities at element level are derived in Appendix C.1 to be:

$$\phi_{\alpha\beta}^{m,e} = \frac{\partial C}{\partial A_{\alpha\beta}^{-1}} = \frac{1}{2}\sum_{\sigma\rho}^{N} A_{\beta\sigma} A_{\rho\alpha} \left(\mathbf{u}_e^t \cdot \frac{d\mathbf{K}_{m,e}}{dA_{\rho\sigma}} \cdot \mathbf{u}_e \right) \tag{4.53}$$

$$\phi_{\alpha\beta}^{b,e} = \frac{\partial C}{\partial D_{\alpha\beta}^{-1}} = \frac{1}{2}\sum_{\sigma\rho}^{N} D_{\beta\sigma} D_{\rho\alpha} \left(\mathbf{u}_e^t \cdot \frac{d\mathbf{K}_{m,e}}{dD_{\rho\sigma}} \cdot \mathbf{u}_e \right) \tag{4.54}$$

4.7. Strength Response Approximation

Groenwold and Haftka proposed to incorporate a load multiplier in the failure criterion to impose a safety factor within the strength optimization algorithm [98]. That is the critical load for first ply failure is $P^* = \lambda P$. The distance from the origin to a point P within the failure envelope is given by a and the distance from the origin to projection P^* of point a on the boundary curve is given by point b, this is illustrated in Figure 4.9. Therefore the load multiplier is given by [62]:

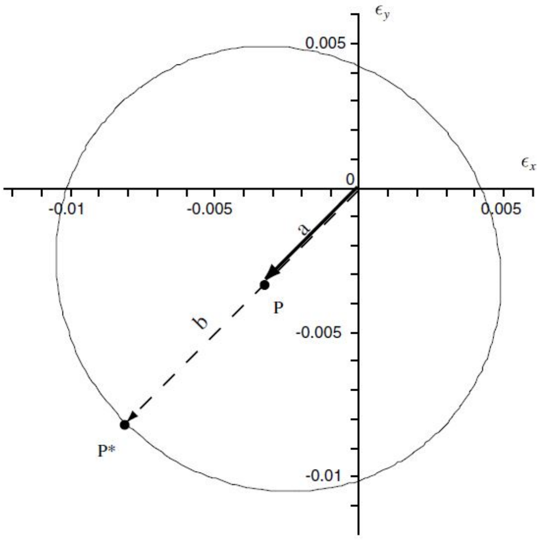

Figure 4.9: Representation of a failure envelope in strain space. For every point within the envelope the multiplier λ is given by b over a. From IJsselmuiden (2008) [62].

$$\lambda = \frac{b}{a} \tag{4.55}$$

The objective of the optimization procedure is to directly maximize the safety factor. This is similar to the minimization of the inverse load multiplier referred to as the failure index r. The optimization problem is stated as:

$$\min_{\mathbf{x}\in S} r\left(\boldsymbol{\epsilon}\left(\mathbf{x}\right)\right) = \min_{\mathbf{x}\in S} \frac{1}{\lambda\left(\boldsymbol{\epsilon}\left(\mathbf{x}\right)\right)} \tag{4.56}$$

The conservative Tsai-Wu failure criterion explained in Equation 3.3 is used to asses the failure index, where the failure envelope is determined by the critical orientation. The failure index equals 0 at the origin and 1 at the boundary curve of the failure envelope. To save computational demand the failure index is approximated by a linear Taylor Series Expansion. Euler's Theorem of homogeneous functions allows to simplify the approximation:

$$r\left(\boldsymbol{\epsilon}\right) \approx r_0 + \mathbf{g}^t \cdot \Delta\boldsymbol{\epsilon} = \boldsymbol{\epsilon}^t \cdot \mathbf{g} = \mathbf{N}^t \cdot \mathbf{A}^{-1} \cdot \mathbf{g} \qquad \text{where} \quad \mathbf{g} = \left.\frac{\partial r}{\partial \epsilon}\right|_0 \tag{4.57}$$

Taking the derivative of the failure index with respect to an arbitrary parameter b results in:

$$\frac{dr}{db} = \underbrace{\mathbf{N}^t \cdot \frac{d\mathbf{A}^{-1}}{db} \cdot \mathbf{g}}_{\text{local}} + \underbrace{\frac{d\mathbf{N}^t}{db} \cdot \mathbf{A}^{-1} \cdot \mathbf{g}}_{\text{global}} \tag{4.58}$$

The first term is local in the sense that the stress resultants are considered to be constant. However, it is known that the failure index also benefits if load is redistributed towards other areas of the structure. This effect is incorporated in the global part. The sensitivity of the local term is given by:

$$r_{\text{local}} \approx \boldsymbol{\Phi}^m : \mathbf{A}^{-1} \qquad \text{where} \qquad \boldsymbol{\Phi}^m = \frac{dr}{d\mathbf{A}^{-1}} = \frac{1}{2}\left(\mathbf{N} \cdot \mathbf{g}^t + \mathbf{g} \cdot \mathbf{N}^t\right) \tag{4.59}$$

where $\boldsymbol{\Phi}^m$ is not necessarily positive definite. To guarantee convexity $\boldsymbol{\Phi}^m$ is split in a positive $\boldsymbol{\Phi}^{m^+}$ and indefinite part $\boldsymbol{\Phi}^{m^-}$. The indefinite part is linearly expanded around $\mathbf{A}_0$ resulting in:

$$r_{\text{local}} \approx \boldsymbol{\Phi}^{m} : \mathbf{A}^{-1} = \boldsymbol{\Phi}^{m^{+}} : \mathbf{A}^{-1} + \boldsymbol{\Phi}^{m^{-}} : \mathbf{A}_0^{-1} + \boldsymbol{\Psi}^{m^{-}} : \mathbf{A} \tag{4.60}$$

For homogeneity the second term $\boldsymbol{\Phi}^{m^{-}} : \mathbf{A}_0^{-1}$ has to be zero, the analysis is omitted here and is explained by Khani *et al* [66]. Dropping the superscripts from the local approximation the final approximation form is given by:

$$r \approx \sum_{i=1}^{N} \boldsymbol{\Phi}_i^{m} : \mathbf{A}^{-1} + \boldsymbol{\Psi}_i^{m} : \mathbf{A} \tag{4.61}$$

In this approximation $\boldsymbol{\Phi}^{m}$ represents the positive definite part of the local approximation and $\boldsymbol{\Psi}^{m}$ is the sum of the linear expanded part of the indefinite part and the sensitivity to the global redistribution effect of loads. The latter is obtained using the adjoint displacement method [66]. The total approximation is homogeneous, convex, but not necessarily conservative [69]. Furthermore the approximation is separable and can be evaluated at nodal level [66]. The corresponding sensitivities at element level are derived in Appendix C.2.

4.7.1. Thermomechanical Strength Response Approximation

The approximation in stiffness space is updated to include the thermal load contribution by an additional thermal term:

$$r \approx \sum_{i=1}^{N} \boldsymbol{\Phi}_i^{m} : \mathbf{A}^{-1} + \boldsymbol{\Psi}_i^{m} : \mathbf{A} + \boldsymbol{\eta}_i^{m} \cdot \Delta\mathbf{N}^{\text{Th}} \tag{4.62}$$

For strain based strength analysis the strain should not include stress thermal expansion. Thus the Taylor Series Expansion of the strength response in strain space given by Equation 4.57 does not change for thermomechanical applications and the local and global derivatives given in Equation 4.58 hold. The global term takes the load redistribution into account, therefore this term needs to be re-evaluated to consider thermal loads. The term is obtained by summation of all element contributions to the load distribution:

$$T_{\text{glocal}} = \frac{d\mathbf{N}^{t}}{db} \cdot \mathbf{A}^{-1} \cdot \mathbf{g} = \sum_{e} \frac{d\mathbf{N}_e^{t}}{db} \cdot \mathbf{A}_e^{-1} \cdot \mathbf{g}_e \tag{4.63}$$

Due to thermal loads the governing equation is now given by:

$$\mathbf{N}_e = \mathbf{A}_e \cdot \boldsymbol{\varepsilon}_e - \mathbf{N}_e^{\text{Th}} \tag{4.64}$$

Therefore the derivative of the stress resultant is given by:

$$\frac{d\mathbf{N}_e}{db} = \frac{d\mathbf{A}_e}{db} \cdot \boldsymbol{\varepsilon}_e + \mathbf{A}_e \cdot \bar{\mathbf{B}}_e \cdot \frac{d\mathbf{u}_e}{db} - \frac{d\mathbf{N}_e^{\text{Th}}}{db} \tag{4.65}$$

The derivatives of the membrane stiffness and thermal load can be evaluated at element level, but the displacement derivative cannot be evaluated at local level. If a stacking sequence of a single element changes the load distribution throughout the structure changes accordingly. Using $\mathbf{s}_e = \mathbf{A}_e^{-1} \cdot \mathbf{g}_e$ the global term is given as:

$$T_{\text{glocal}} = \mathbf{s}_i^{t} \cdot \frac{d\mathbf{A}_i}{db} \cdot \boldsymbol{\varepsilon}_i + \sum_{e} \mathbf{s}_e^{t} \cdot \mathbf{A}_e \cdot \bar{\mathbf{B}}_e \cdot \frac{d\mathbf{u}_e}{db} - \mathbf{s}_i^{t} \cdot \frac{d\mathbf{N}_i^{\text{Th}}}{db} \tag{4.66}$$

A new term $\mathbf{f}_e$ is introduced to simplify the equation:

$$\mathbf{f}_e = \bar{\mathbf{B}}_e^{t} \cdot \mathbf{A}_e \cdot \mathbf{s}_e \qquad \rightarrow \qquad T_{\text{glocal}} = \mathbf{s}_i^{t} \cdot \frac{d\mathbf{A}_i}{db} \cdot \boldsymbol{\varepsilon}_i + \sum_{e} \mathbf{f}_e \cdot \frac{d\mathbf{u}_e}{db} - \mathbf{s}_i^{t} \cdot \frac{d\mathbf{N}_i^{\text{Th}}}{db} \tag{4.67}$$

Adjoint Displacement Approach

To determine the derivative of the displacement vector the adjoint displacement approach is applied. The adjoint displacement vector **v** is calculated by solving:

$$\mathbf{K}_m \mathbf{v} = \mathbf{f} \tag{4.68}$$

Taking the derivative of the linear finite element problem $\mathbf{K}_m \cdot \mathbf{u} = \mathbf{F} + \mathbf{F}^{\mathrm{Th}}$:

$$\frac{d\mathbf{K}_m}{db} \cdot \mathbf{u} + \mathbf{K}_m \cdot \frac{d\mathbf{u}}{db} = \frac{d\mathbf{F}^{\mathrm{Th}}}{db} \quad \rightarrow \quad \mathbf{K}_m \cdot \frac{d\mathbf{u}}{db} = \frac{d\mathbf{F}^{\mathrm{Th}}}{db} - \frac{d\mathbf{K}_m}{db} \cdot \mathbf{u} \tag{4.69}$$

Multiplying both sides by the adjoint displacement vector **v** yields:

$$\mathbf{v}^t \cdot \mathbf{K}_m \cdot \frac{d\mathbf{u}}{db} = \mathbf{v}^t \cdot \left(\frac{d\mathbf{F}^{\mathrm{Th}}}{db} - \frac{d\mathbf{K}_m}{db} \cdot \mathbf{u} \right) \quad \rightarrow \quad \mathbf{f} \cdot \frac{d\mathbf{u}}{db} = \mathbf{v}^t \cdot \left(\frac{d\mathbf{F}^{\mathrm{Th}}}{db} - \frac{d\mathbf{K}_m}{db} \cdot \mathbf{u} \right) \tag{4.70}$$

The right hand side can be evaluated at the local element level, since all global redistribution of load is embedded in the adjoint displacement vector. The right hand side is substituted in the global term and now all terms can be evaluated at element level:

$$T_{\mathrm{glocal}} = \mathbf{s}_i^t \cdot \frac{d\mathbf{A}_i}{db} \cdot \boldsymbol{\varepsilon}_i + \mathbf{v}_i^t \cdot \left(\frac{d\mathbf{F}_i^{\mathrm{Th}}}{db} - \frac{d\mathbf{K}_{m,i}}{db} \cdot \mathbf{u}_i \right) - \mathbf{s}_i^t \cdot \frac{d\mathbf{N}_i^{\mathrm{Th}}}{db} \tag{4.71}$$

Total Derivative

Combining the local and global terms the total derivative is given by:

$$\frac{dr}{db} = \underbrace{\mathbf{N}_i^t \cdot \frac{d\mathbf{A}_i^{-1}}{db} \cdot \mathbf{g}_i}_{T_{\mathrm{local}}} + \underbrace{\mathbf{s}_i^t \cdot \frac{d\mathbf{A}_i}{db} \cdot \boldsymbol{\varepsilon}_i + \mathbf{v}_i^t \cdot \left(\frac{d\mathbf{F}_i^{\mathrm{Th}}}{db} - \frac{d\mathbf{K}_{m,i}}{db} \cdot \mathbf{u}_i \right) - \mathbf{s}_i^t \cdot \frac{d\mathbf{N}_i^{\mathrm{Th}}}{db}}_{T_{\mathrm{glocal}}} \tag{4.72}$$

The local term depends on $\mathbf{A}^{-1}$ and the global term on **A**, therefore the stiffness sensitivities for element e are given by:

$$\phi_{\alpha\beta}^{m,e} = \frac{\partial r}{\partial A_{\alpha\beta}^{-1}} = \sum_{\sigma\rho}^{N} \mathbf{N}_e^t \cdot \frac{d\mathbf{A}_e^{-1}}{dA_{\rho\sigma}^{-1}} \cdot \mathbf{g}_e \tag{4.73}$$

$$\psi_{\alpha\beta}^{m,e} = \frac{\partial r}{\partial A_{\alpha\beta}} = \sum_{\sigma\rho}^{N} \left(\mathbf{s}_e^t \cdot \frac{d\mathbf{A}_e}{dA_{\rho\sigma}} \cdot \boldsymbol{\varepsilon}_e - \mathbf{v}_e^t \cdot \frac{d\mathbf{K}_{m,e}}{dA_{\rho\sigma}} \cdot \mathbf{u}_e \right) \tag{4.74}$$

Note that $\boldsymbol{\Phi}^m$ is similar to the mechanical strength response and needs to be split in a positive and indefinite part. Furthermore the global term is influenced by thermal loads, therefore the thermal sensitivity is given by:

$$\boldsymbol{\eta}^{m,e} = \frac{\partial r}{\partial N^{\mathrm{Th}}} = \mathbf{v}_e^t \frac{d\mathbf{F}_e^{\mathrm{Th}}}{dN^{\mathrm{Th}}} - \mathbf{s}_i^t \cdot \frac{d\mathbf{N}_e^{\mathrm{Th}}}{dN^{\mathrm{Th}}} \tag{4.75}$$

The thermal forces are calculated by the thermal loads, hence the thermal sensitivity can be rewritten to:

$$\frac{d\mathbf{F}_e^{\mathrm{Th}}}{dN_e^{\mathrm{Th}}} = A_e \bar{\mathbf{B}}_e^t \frac{d\mathbf{N}_e^{\mathrm{Th}}}{dN_e^{\mathrm{Th}}} \quad \rightarrow \quad \boldsymbol{\eta}^{m,e} = \left(A_e \bar{\mathbf{B}}_e \mathbf{v}_e - \mathbf{s}_e \right)^t \tag{4.76}$$

4.8. Buckling Response Approximation

Buckling can be described as an eigenvalue problem given by Equation 4.77, where $\mathbf{K}_b$ is the global bending stiffness matrix, $\mathbf{K}_g$ the global geometric stiffness matrix, λ the buckling factor and $\mathbf{a}$ is the normalized eigenvector corresponding to the buckling mode.

$$\left(\mathbf{K}_m - \lambda \mathbf{K}_g\right) \cdot \mathbf{a} = 0 \tag{4.77}$$

Maximizing the buckling load yields a minimization of the inverse buckling load, this optimization is stated as:

$$\min_{\mathbf{x} \in S} r(\mathbf{x}) = \min_{\mathbf{x} \in S} \frac{1}{\lambda(\mathbf{x})} \tag{4.78}$$

The derivative of the buckling factor with respect to a general parameter b is given by:

$$\frac{d\lambda}{db} = \underbrace{\lambda \mathbf{a}^t \frac{d\mathbf{K}_m}{db} \mathbf{a}}_{\text{local}} - \underbrace{\lambda^2 \mathbf{a}^t \frac{d\mathbf{K}_g}{db} \mathbf{a}}_{\text{global}} \tag{4.79}$$

The first term is related to derivative of the local bending stiffness and the second term depends on the derivative of the global geometric stiffness. This term is global since it depends on the element loads of the entire structure, therefore this term essentially represents the effect of load redistribtion [64].

For a plate the buckling load factor is homogeneous with respect to the in-plane and bending stiffness of order zero and one respectively. Therefore the inverse buckling load is homogeneous of order zero and one with respect to the in-plane membrane stiffness $\mathbf{A}$ and the inverse bending stiffness $\mathbf{D}^{-1}$. The approximation then becomes of the form presented:

$$r \approx \sum_{i=1}^{N} \mathbf{\Psi}_i^m : \mathbf{A} + \mathbf{\Phi}_i^b : \mathbf{D}^{-1} \tag{4.80}$$

Note that the membrane stiffness accounts for the global load distribution and the inverse bending stiffness accounts for the local bending resistance. Euler's theory for homogeneous functions shows that $\mathbf{\Psi}^m$ is not necessarily positive definite. This does not appear problematic since the terms are linear, therefore the positive definite reciprocal terms guarantees a total approximation that is convex [63, 64]. Thereby the approximation is homogeneous, not necessarily conservative and separability allows for evaluation at nodal level.

The inverse buckling load approximation for shells is given by Equation 4.81. By curvature of the part in- and out-of-plane contributions are no longer separate. The bending stiffness influences in-plane behavior and the membrane stiffness influences out-of-plane behavior, thus terms $\mathbf{A}$ and $\mathbf{D}^{-1}$ appear in the approximation:

$$r \approx \sum_{i=1}^{N} \mathbf{\Psi}_i^m : \mathbf{A} + \mathbf{\Psi}_i^b : \mathbf{D} + \mathbf{\Phi}_i^m : \mathbf{A}^{-1} + \mathbf{\Phi}_i^b : \mathbf{D}^{-1} \tag{4.81}$$

For the pure mechanical buckling response the elemental sensitivities are derived in Appendix C.3.

4.8.1. Thermomechanical Buckling Response Approximation

The approximation is updated to include the thermal load contribution by an additional thermal term:

$$r \approx \sum_{i=1}^{N} \mathbf{\Psi}_i^m : \mathbf{A} + \mathbf{\Psi}_i^b : \mathbf{D} + \mathbf{\Phi}_i^m : \mathbf{A}^{-1} + \mathbf{\Phi}_i^b : \mathbf{D}^{-1} + \boldsymbol{\eta}_i^m \cdot \Delta \mathbf{N}^{\mathrm{Th}} \tag{4.82}$$

For thermomechanical load applications it is discussed in subsection 3.5.2 that the buckling equation becomes of the following form:

$$\left[\mathbf{K}_m - \lambda\left(\mathbf{K}_g^{\mathrm{M}} + \mathbf{K}_g^{\mathrm{Th}}\right)\right] \cdot \mathbf{a} = 0 \tag{4.83}$$

The sensitivity analysis of the pure mechanical buckling formulation is given in Appendix C.3. Based on this the sensitivities of the thermomechanical buckling formulation are derived. Taking the derivative of the buckling factor with respect to a general parameter b yields:

$$\frac{d\lambda}{db} = \underbrace{\lambda \mathbf{a}^t \frac{d\mathbf{K}_m}{db}\mathbf{a}}_{\text{local}} - \underbrace{\lambda^2 \mathbf{a}^t \left(\frac{d\mathbf{K}_g^{\mathrm{M}}}{db} + \frac{d\mathbf{K}_g^{\mathrm{Th}}}{db}\right)\mathbf{a}}_{\text{global}} \tag{4.84}$$

Local Term - Material Stiffness
The local term can be evaluated at the local ith element level:

$$T_{\text{local}} = \mathbf{a}^t \cdot \frac{d\mathbf{K}_m}{db} \cdot \mathbf{a} = \mathbf{a}_i^t \cdot \frac{d\mathbf{K}_{m,i}}{db} \cdot \mathbf{a}_i \tag{4.85}$$

Global Term - Geometric Stiffness
Due to the implementation of thermal load the global term has to be re-evaluated. The geometric stiffness matrix changes on a global level and the derivatives of all elements are summed. Defining:

$$\mathbf{K}_{g,e} = -n_{x,e}\mathbf{K}_x - n_{y,e}\mathbf{K}_y - n_{xy,e}\mathbf{K}_{xy} \qquad \text{and} \qquad \mathbf{s}_e = \left[\mathbf{a}_e^t \cdot \mathbf{K}_x \cdot \mathbf{a}_e; \quad \mathbf{a}_e^t \cdot \mathbf{K}_y \cdot \mathbf{a}_e; \quad \mathbf{a}_e^t \cdot \mathbf{K}_{xy} \cdot \mathbf{a}_e\right]^t \tag{4.86}$$

results in the following global term:

$$T_{\text{global}} = \mathbf{a}^t \left(\frac{d\mathbf{K}_g^{\mathrm{M}}}{db} + \frac{d\mathbf{K}_g^{\mathrm{Th}}}{db}\right)\mathbf{a} = -\sum_e \mathbf{s}_e^t \cdot \frac{d\mathbf{N}_e}{db} \tag{4.87}$$

Due to thermal loads the governing equation is now given by:

$$\mathbf{N}_e = \mathbf{A}_e \cdot \boldsymbol{\varepsilon}_e - \mathbf{N}_e^{\mathrm{Th}} \tag{4.88}$$

Therefore the derivative of the stress resultant is given by:

$$\frac{d\mathbf{N}_e}{db} = \frac{d\mathbf{A}_e}{db} \cdot \boldsymbol{\varepsilon}_e + \mathbf{A}_e \cdot \bar{\mathbf{B}}_e \cdot \frac{d\mathbf{u}_e}{db} - \frac{d\mathbf{N}_e^{\mathrm{Th}}}{db} \tag{4.89}$$

The derivatives of the membrane stiffness and thermal load can be evaluated at element level, but the displacement derivative cannot be evaluated at local level. If a stacking sequence of an element changes the load distribution throughout the structure changes accordingly. Altogether the global derivative term becomes:

$$T_{\text{global}} = -\mathbf{s}_i^t \cdot \frac{d\mathbf{A}_i}{db} \cdot \boldsymbol{\varepsilon}_i - \sum_e \mathbf{s}_e^t \cdot \mathbf{A}_e \cdot \bar{\mathbf{B}}_e \cdot \frac{d\mathbf{u}_e}{db} + \mathbf{s}_i^t \cdot \frac{d\mathbf{N}_i^{\mathrm{Th}}}{db} \tag{4.90}$$

A new term $\mathbf{f}_e$ is introduced to simplify the equation:

$$\mathbf{f}_e = \bar{\mathbf{B}}_e^t \cdot \mathbf{A}_e \cdot \mathbf{s}_e \qquad \rightarrow \qquad T_{\text{global}} = -\mathbf{s}_i^t \cdot \frac{d\mathbf{A}_i}{db} \cdot \boldsymbol{\varepsilon}_i - \sum_e \mathbf{f}_e^t \cdot \frac{d\mathbf{u}_e}{db} + \mathbf{s}_i^t \cdot \frac{d\mathbf{N}_i^{\mathrm{Th}}}{db} \tag{4.91}$$

Adjoint Displacement Approach

To determine the derivative of the displacement vector the adjoint displacement approach used for the thermomechanical strength response is applied. The global term can now be evaluated at element level:

$$T_{\text{global}} = -\mathbf{s}_i^t \cdot \frac{d\mathbf{A}_i}{db} \cdot \boldsymbol{\varepsilon}_i - \mathbf{v}_i^t \cdot \left(\frac{d\mathbf{F}_i^{\text{Th}}}{db} - \frac{d\mathbf{K}_{m,i}}{db} \cdot \mathbf{u}_i \right) + \mathbf{s}_i^t \cdot \frac{d\mathbf{N}_i^{\text{Th}}}{db} \tag{4.92}$$

Total Derivative

Substituting both local and global terms into the total derivative yields the following relation for the *i*th element:

$$\frac{d\lambda}{db} = \underbrace{\lambda \left(\mathbf{a}_i^t \cdot \frac{d\mathbf{K}_{m,i}}{db} \cdot \mathbf{a}_i \right)}_{\text{material stiffness}} + \underbrace{\lambda^2 \left(\mathbf{s}_i^t \cdot \frac{d\mathbf{A}_i}{db} \cdot \mathbf{e}_i + \mathbf{v}_i^t \cdot \left(\frac{d\mathbf{F}_i^{\text{Th}}}{db} - \frac{d\mathbf{K}_{m,i}}{db} \cdot \mathbf{u}_i \right) - \mathbf{s}_i^t \frac{d\mathbf{N}_i^{\text{Th}}}{db} \right)}_{\text{geometric stiffness}} \tag{4.93}$$

The thermomechanical response formulation is repeated. The linear terms are based on the geometric stiffness, and the reciprocal terms depend on the material stiffness:

$$r \approx \sum_{i=1}^{N} \underbrace{\boldsymbol{\Psi}_i^m : \mathbf{A} + \boldsymbol{\Psi}_i^b : \mathbf{D}}_{\text{geometric stiffness}} + \underbrace{\boldsymbol{\Phi}_i^m : \mathbf{A}^{-1} + \boldsymbol{\Phi}_i^b : \mathbf{D}^{-1} + \boldsymbol{\eta}_i^m \cdot \Delta \mathbf{N}^{\text{Th}}}_{\text{material stiffness}} \tag{4.94}$$

Combining the following expressions:

$$\frac{\partial f}{\partial \mathbf{A}} = -\mathbf{A}^{-1} \cdot \frac{\partial f}{\partial \mathbf{A}^{-1}} \cdot \mathbf{A}^{-1} \quad \text{and} \quad \frac{\partial f}{\partial \mathbf{A}^{-1}} = -\mathbf{A} \cdot \frac{\partial f}{\partial \mathbf{A}} \cdot \mathbf{A} \tag{4.95}$$

And using the chain-rule to obtain the actual response derivative:

$$\frac{\partial r}{\partial b} = \frac{\partial r}{\partial \lambda} \frac{\partial \lambda}{\partial b} \quad \rightarrow \quad \frac{\partial r}{\partial b} = -\frac{1}{\lambda^2} \frac{\partial \lambda}{\partial b} \tag{4.96}$$

results in the following sensitivities for material stiffness at element level:

$$\phi_{\alpha\beta}^{m,e} = \frac{\partial r}{\partial A_{\alpha\beta}^{-1}} = \frac{1}{\lambda} \sum_{\sigma\rho}^{N} A_{\beta\sigma} A_{\rho\alpha} \left(\mathbf{a}_e^t \cdot \frac{d\mathbf{K}_{m,e}}{dA_{\rho\sigma}} \cdot \mathbf{a}_e \right) \tag{4.97}$$

$$\phi_{\alpha\beta}^{b,e} = \frac{\partial r}{\partial D_{\alpha\beta}^{-1}} = \frac{1}{\lambda} \sum_{\sigma\rho}^{N} D_{\beta\sigma} D_{\rho\alpha} \left(\mathbf{a}_e^t \cdot \frac{d\mathbf{K}_{b,e}}{dD_{\rho\sigma}} \cdot \mathbf{a}_e \right) \tag{4.98}$$

and for geometric stiffness:

$$\psi_{\alpha\beta}^{m,e} = \frac{\partial r}{\partial A_{\alpha\beta}} = \sum_{\sigma\rho}^{N} \left(-\mathbf{s}_e^t \cdot \frac{d\mathbf{A}_e}{dA_{\rho\sigma}} \cdot \mathbf{e}_e + \mathbf{v}_e^t \cdot \frac{d\mathbf{K}_{m,e}^t}{dA_{\rho\sigma}} \cdot \mathbf{u}_e \right) \tag{4.99}$$

$$\psi_{\alpha\beta}^{b,e} = \frac{\partial r}{\partial D_{\alpha\beta}} = \sum_{\sigma\rho}^{N} \left(\mathbf{v}_e^t \cdot \frac{d\mathbf{K}_{b,i}^t}{dD_{\rho\sigma}} \cdot \mathbf{u}_e \right) \tag{4.100}$$

$$\boldsymbol{\eta}^{m,e} = \frac{\partial r}{\partial N^{\text{Th}}} = \mathbf{v}_e^t \frac{d\mathbf{F}_e^{\text{Th}}}{dN_e^{\text{Th}}} + \mathbf{s}_e^t \frac{d\mathbf{N}_e^{\text{Th}}}{dN_e^{\text{Th}}} \tag{4.101}$$

The thermal forces are calculated by the thermal loads, hence the thermal sensitivity can be rewritten to:

$$\frac{d\mathbf{F}_e^{\text{Th}}}{dN_e^{\text{Th}}} = A_e \bar{\mathbf{B}}_e^t \frac{d\mathbf{N}_e^{\text{Th}}}{dN_e^{\text{Th}}} \quad \rightarrow \quad \boldsymbol{\eta}^{m,e} = \left(-A_e \bar{\mathbf{B}}_e \mathbf{v}_e + \mathbf{s}_e \right)^t \tag{4.102}$$

5

Verification - Rectangular Plate

The optimization procedure is explained in the previous chapters. Before looking into a real world application it is essential to verify the model. Verification is based on research led by Gurdal that optimized the rectangular plate shown in Figure 5.1 for both mechanical and thermomechanical loads [17, 99, 100].

Similar to the reference papers a = 381mm and the aspect ratio of the plate is set to 1. The edges of the plate are simply supported, that is the out of plane deformation is suppressed but rotation is allowed. Additionally the edges are traction free and the transverse edges are forced to remain straight. Mechanical load is applied to generate uniform end shortening due to a corresponding uni-axial N_x distribution. The laminate is build from T300/5208 plies and the corresponding material properties are given in Table 5.1. A total of 12 plies are used to yield a total thickness of 1.524mm. This is thin enough so the in-plane failure strains are a magnitude larger than the experienced buckling strains, thus no strength failure criteria needs to be checked [99].

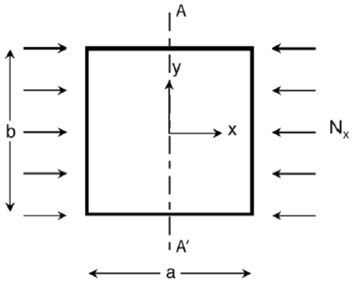

Figure 5.1: Simply Supported rectangular plate used for verification.

Table 5.1: Material Properties of the T300/5208 carbon fiber composite

E_1	174.1	GPa	α_1	0.02e-6	K^{-1}
E_2	10.3	GPa	α_2	2.25e-6	K^{-1}
ν_{12}	0.28	–	t	0.1270	mm
G_{12}	7.17	GPa	h	1.5240	mm

5.1. Linearly Varying Fiber Orientations

Buckling optimization is performed for the described plate by Olmedo and Gurdal [17]. Linearly varying fiber orientations are discussed in chapter 2 and this parameterization is used to define a variable-stiffness laminate. For convenience the equation related to the fiber angle variation is repeated:

$$\theta\left(x'\right) = \phi + \frac{(T_1 - T_0)}{d} x' + T_0 \tag{5.1}$$

To ease the optimization they set parameter ϕ to 90 degrees, this effectively sets the fiber angle variation to be in the y-direction of the plate, i.e. $\theta\left(y\right)$. For free transverse edges variable stiffness causes a variation in poisson's ratio, thus the panel experiences deformation patterns that are nonuniform due to the applied compression load. For standard panel tests of variable-stiffness laminates the transverse edge are constrained to remain straight. This results in an uniform deformation pattern, however the applied load is distributed in a nonuniform pattern over the structure. Applications that represents this behavior are stiffened variable stiffness panels.

The load distribution depends on the stiffness variation over the structure. Since the stiffness of the panels is determined by the fiber paths a change in parameters T_0 and T_1 will lead to different load distributions. Optimization of the buckling load resulted in advantageous load distributions to increase the buckling resistance of the plate. To analyze the critical buckling load the Ritz method is applied.

Olmedo and Gurdal compared the determined optimum linearly varying fiber angle distribution $< 90, (0\,|\,75) >$ with the optimal constant stiffness design ±45. The results are given in Table 5.2 where the critial buckling load multiplier is normalized by:

$$\bar{\lambda}_{cr} = \frac{\lambda_{cr} a^2}{E_1 h^3} \tag{5.2}$$

The varying fiber paths yields high stiffness close to the restrained transverse edges and low stiffness at the center of the plate. The major part of the compression load is carried by the high stiffness regions close to the transverse edges that has better buckling resistance due to the suppressed out of plane deformation by the boundary conditions. The middle area that is prone to buckling only carries a minor part of the compression load, hence the load distribution improves the buckling resistance of the plate.

Table 5.2: Normalized critical buckling load multiplier for the optimal constant and linearly varying fiber orientation designs [17].

Design	$\bar{\lambda}_{cr}$
±45	1.75
$\pm < 90, (0\,|\,75) >$	3.14

5.2. Optimization in Lamination Parameter Space

In later studies IJsselmuiden *et al* used the same panel to demonstrate the influence of thermomechanical loads on the buckling performance [99, 100]. The following eigenvalue buckling formulation was used:

$$\left(\mathbf{K}_m - \lambda_M \mathbf{K}_g^M - \mathbf{K}_g^{Th}\right)\mathbf{a} = 0 \tag{5.3}$$

In this formulation the thermal load is given as a pre-load, thereafter the critical mechanical load is calculated in their research. To increase the flexibility of variable stiffness panels they optimized the stiffness distribution based on the optimization framework from IJsselmuiden in the lamination parameter design space described in the previous chapter. Optimization was performed for 0, -100 and -200 degrees temperature difference:

Case I: Optimization for $\Delta T = 0^o$C.
Case II: Optimization for $\Delta T = -100^o$C.
Case III: Optimization for $\Delta T = -200^o$C.

The obtained optimal designs are compared to the optimal design derived by Olmedo and Gurdal as well as a quasi-isotropic and the optimal constant stiffness ±45 design. The results are given in Table 5.3 for a 20 x 20 mesh consisting of rectangular elements.

Table 5.3: Normalized critical buckling load multipliers for the optimal constant, optimal linearly varying fiber orientation, and optimal thermomechanical load cases I-III [100]. The values in bold show the critical buckling multiplier for the designs optimized for the corresponding thermal load.

	Temperature change ΔT		
Design	0K	−100K	−200K
QI	1.3842	1.3842	1.3842
±45	1.7424	1.7424	1.7424
$\pm<90,(0\,|\,75)>$	2.9282	4.3855	1.4518
Case I	**4.0157**	6.0802	2.9758
Case II	3.2468	**7.2615**	8.0472
Case III	2.5481	6.2637	**9.0829**

5.3. Verification of Thermal Analysis

The results presented in Table 6.2 are ideal to verify the implemented thermal load analysis. First the buckling loads of the constant stiffness panels are verified. The results are given in Table 5.4, 18 DOF triangular shell elements are used and a mesh refinement is included to show convergence. Similar results are obtained and the temperature differences do not influence the buckling load since the plate exhibits stress free thermal expansion for constant stiffness designs.

Table 5.4: Normalized critical buckling multipliers for different meshes. Results are exactly similar for $\Delta T = 0$K, $\Delta T = -100$K and $\Delta T = -200$K due to free thermal expansion. Difference is measured with respect to the result for a 60 x 60 mesh.

Mesh	QI Design	Difference [%]	±45 Design	Difference [%]
10 x 10	1.3717	-0.91	1.6722	-3.07
20 x 20	1.3782	-0.44	1.7030	-1.28
30 x 30	1.3811	-0.23	1.7139	-0.65
40 x 40	1.3826	-0.12	1.7195	-0.32
50 x 50	1.3837	-0.04	1.7228	-0.13
60 x 60	1.3843		1.7251	
Ref. [100]: 20 x 20	1.3842	-0.01	1.7424	+0.99

The optimal linearly varying fiber orientation design found by Olmedo and Gurdal is analyzed to check whether the thermal induced stresses influence the buckling behavior correctly. For $\Delta T = 0$K the results are given in Table 5.5. For a 20 x 20 mesh the normalized critical buckling multiplier of 2.94 is similar to the result found by IJsselmuiden *et al.* Refining the mesh increases the buckling multiplier to 3.09, which is closer to the solution found by Olmedo and Gurdal with the Ritz method.

Table 5.5: Normalized buckling multipliers for $\Delta T = 0$K for different meshes. Difference is measured with respect to the result for a 60 x 60 mesh. (1) Difference is measured with respect to the result for a 20 x 20 mesh.

Mesh	$\pm<90,(0\,|\,75)>$	Difference [%]
20 x 20	2.9410	-4.88
30 x 30	3.0320	-1.94
40 x 40	3.0660	-0.84
50 x 50	3.0826	-0.30
60 x 60	3.0920	
Ref. [62]	3.14	+1.55
Ref. [100]: 20 x 20 (1)	2.9282	-0.44

For $\Delta T = -100$K and $\Delta T = -200$K the results cannot directly be compared due to the different buckling formulation. The buckling multiplier in the buckling formulation given in Equation 3.59 also scales the thermal load, yielding different results from the buckling formulation given by Equation 5.3. To make a comparison between the reference paper and the obtained results from the implemented thermal analysis the critical buckling multiplier from Table 6.2 is converted to its corresponding critical mechanical load. The thermal load and the critical mechanical load are applied and should yield a buckling multiplier of 1, since the initial load condition is already critical. The results are given in Table 5.6 and buckling multipliers of 1 are found for $\Delta T = -100$K and $\Delta T = -200$K. Additionally pure thermal buckling is found for $\Delta T = -240$K and $\Delta T = 27$K in correspondence with the reference paper.

Table 5.6: Critical buckling load multipliers for ΔT of -100K, -200K, -240K and 27K.

ΔT [K]	Mesh	N_{cr} [kN]	$\pm < 90, (0 \mid 75) >$
-100	20 x 20	19.4	0.9947
-200	20 x 20	6.4	1.0017
-240	20 x 20	-	1.0035
+27	20 x 20	-	0.9962

5.4. Verification of the Optimization Routine

Before the optimization is performed and compared to the results given in Table 6.2 first the approximations are verified. The sensitivities form the backbone of the approximations and are verified by the finite difference approximation [85]. A small step deviation δ is introduced to the design parameter x, this is followed by finite element analysis to compute the structural responses $f(x+\delta)$ and $f(x-\delta)$. This is used to determine the sensitivity according to the second order central finite difference approximation:

$$\frac{\partial f}{\partial x} = \frac{f(x+\delta) - f(x-\delta)}{2\delta} \tag{5.4}$$

The response sensitivities calculated by the derivatives given in the previous chapter should be close or similar to the sensitivities derived by the finite difference approximation. For all responses the sensitivities are verified to yield the same results as the finite difference results for different design parameters and small step sizes. To check whether the approximations are correctly build the sensitivities are used to approximate the structural responses for small deviations of the design parameters. The deviations are also used to calculate the response by finite element analysis, for small step sizes the results showed to be close or similar:

$$f^{(1)}\left(\Delta\mathbf{A}, \Delta\mathbf{D}, \Delta\mathbf{N}^{Th}\right) \approx f_{\text{FEM}}\left(\mathbf{A}+\Delta\mathbf{A}, \mathbf{D}+\Delta\mathbf{D}, \mathbf{N}^{Th}+\Delta\mathbf{N}^{Th}\right) \tag{5.5}$$

$$f^{(2)}(\Delta\boldsymbol{\theta}) \approx f_{\text{FEM}}(\boldsymbol{\theta}+\Delta\boldsymbol{\theta}) \tag{5.6}$$

For the verification the buckling optimization is performed in the fiber angle design space. The local steering constraint is set to a minimal steering radius of 333mm. To make a comparison with the optimal results obtained by IJsselmuiden *et al* the mechanical load is iteratively changed for a given thermal load until the critical buckling multiplier equals 1. This effectively simulates the buckling formulation used by IJsselmuiden *et al* where the thermal load is defined as a pre-load and the mechanical load is scaled to find the critical buckling factor. The results are presented in Table 5.7.

Table 5.7: The first three critical buckling modes after optimization for ΔT of 0K, -100K and -200K.

ΔT [^{o}C]	Mesh	N_{cr} [kN] of ref. [100]	Difference [%]	$N_{cr,1}$ [kN]	$N_{cr,2}$ [kN]	$N_{cr,3}$ [kN]
0	20 x 20	17.7	-28	12.8	12.8	19.7
-100	20 x 20	32.0	-27	23.5	24.8	27.8
-200	20 x 20	40.1	-28	29.0	29.1	31.9

The critical buckling loads for the first three buckling modes are given. It is clear from the table that due to the optimization the first two buckling modes are almost equally critical. In essence the optimization routine tries to redistribute the load and to change the buckling resistance to counteract the most critical buckling mode. Due to this behavior other buckling modes become more dominant until one of these modes becomes critical. This process continues until two or more buckling modes are dominant and changing the design will only cause one of the buckling modes to initiate at a lower load.

The presented results are for a minimum steering radius of 333mm. This is one of the causes of the differences with the result of the reference paper. Although the designs in lamination parameters does consider continuity it does not take into account manufacturability. To investigate the influence of the steering radius optimization with minimum steering radii of 500mm and 250mm are also performed. The results are given in Table 5.8, from the results it is clear that more steering allows for a design that is closer to the reference design.

Table 5.8: The first three critical buckling modes after optimization for $\Delta T = -200^0$C and for different steering radii.

ΔT [^{o}C]	Mesh	r_{min} [mm]	N_{cr} [kN] of ref. [100]	Difference [%]	$N_{cr,1}$ [kN]	$N_{cr,2}$ [kN]	$N_{cr,3}$ [kN]
-200	20 x 20	500	40.1	-41	23.8	26.2	29.0
-200	20 x 20	333	40.1	-28	29.0	29.1	31.9
-200	20 x 20	250	40.1	-18	32.9	33.0	35.7

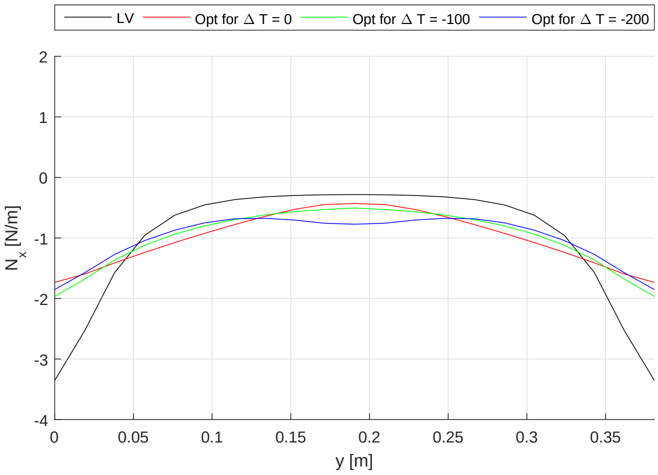

Figure 5.2: Stress resultant at $x = a/2$ for different designs for a unit applied compressive load. 'LV' stand for linear variation and 'Opt' stands for optimal design.

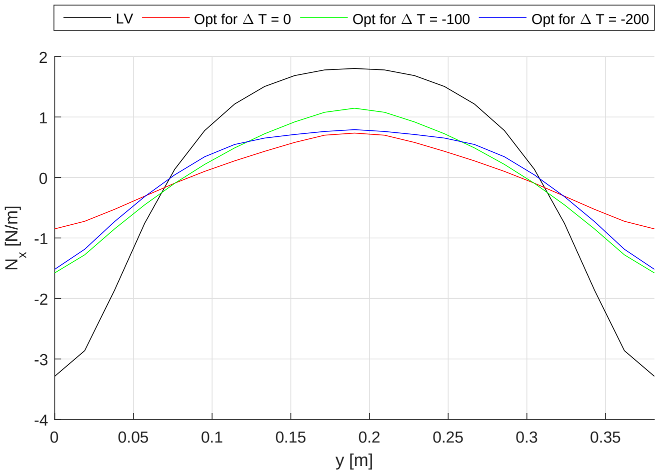

Figure 5.3: Stress resultant at $x = a/2$ for different designs for a unit applied negative thermal load. 'LV' stand for linear variation and 'Opt' stands for optimal design.

To explain how the buckling resistance of the plate increases the stress resultant N_x is plotted over the center-line presented in Figure 5.1 at $x = a/2$ for a unit applied compressive and negative thermal load in Figure 5.2 and Figure 5.3 respectively. Both thermal and mechanical loads are distributed towards the constrained transverse edges, whereas the prone to buckling middle section is relieved from compressive stresses. Furthermore the thermal loads are distributed in such a way that stabilizing tensile stresses in the middle area are created, hence the gain in performance under negative thermal load.

For case I the thermal loads are not assessed in the optimization. This is visible in Figure 5.3, where the design does not distribute the thermal load as effectively as the designs for case II and case III. The distributions for case II and case III are more consistent, where case III distributes the stabilizing tensile stresses over a larger area.j Since the thermal load for case III is higher a larger area benefits from the stabilizing effect.

The influence of the load distribution on the buckling modes is visible in the buckling mode plots. The buckling modes are plotted in Figure 5.4, Figure 5.5 and Figure 5.6 for $\Delta T = 0$K, $\Delta T = -100$K and $\Delta T = -200$K respectively. For the plates under a higher thermal load it is visible that the buckling modes shift towards the transverse edges and edge buckling appears. This behavior corresponds to the described load distribution.

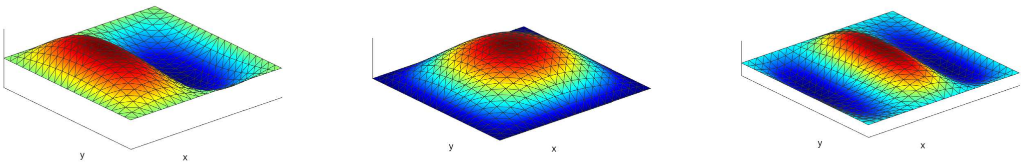

Figure 5.4: First three critical buckling modes for $\Delta T = 0$. The corresponding critical buckling loads are $N_{x,1} = 12.8$kN, $N_{x,2} = 12.8$ and $N_{x,3} = 19.7$.

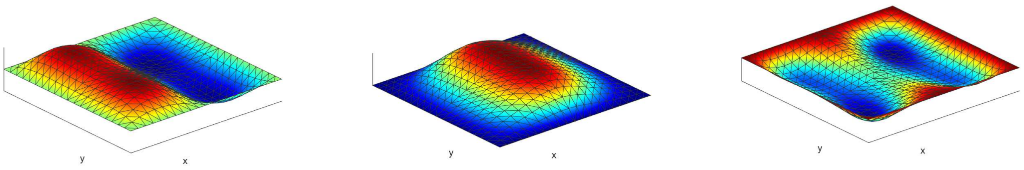

Figure 5.5: First three critical buckling modes for $\Delta T = -100$. The corresponding critical buckling loads are $N_{x,1} = 23.5$kN, $N_{x,2} = 24.8$ and $N_{x,3} = 27.8$kN.

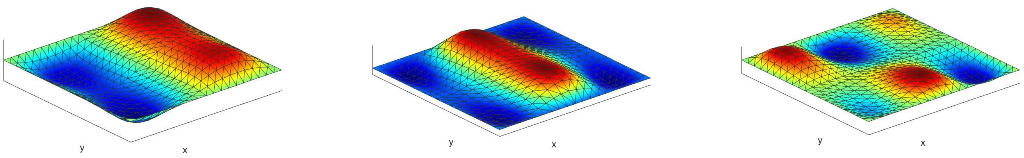

Figure 5.6: First three critical buckling modes for $\Delta T = -200$. The corresponding critical buckling loads are $N_{x,1} = 29.0$kN, $N_{x,2} = 29.1$ and $N_{x,3} = 31.9$kN.

At last the verification is performed once more for the same plate, but the plate is rotated so the local element orientation and global coordinate system do not coincide. This is done to check whether the implementation of transformations between local element orientations and the global model coordinate system is executed correctly. The exact same results were obtained, indicating correct implementation of transformations.

6

Application - Engine Thrust Frame

Now the optimization routine has been verified it will be used to optimize the laminate design of an engine thrust frame (ETF), which is shown in Figure 6.1. The structure transfers the thrust load of the rocket engine to the rocket bus, due to the dimension differences of the bus and the engine a conical shape is used. The conical shape is made from carbon fiber reinforced polymer.

The conical part is connected to a top and an X-ring made from aluminum. For the application considered in this study the ring is simplified to the geometry shown in Figure 6.1. Due to confidentiality the material properties and dimensions of the engine thrust frame will not be specified.

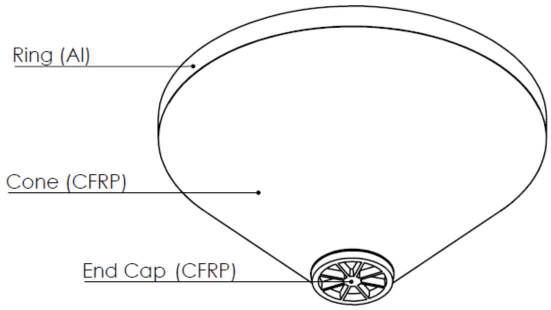

Figure 6.1: Design and dimensions of the ETF in meters. The ETF consist of an aluminum top-ring, CFR cone and a CFRP end-cap. There are multiple CFRP stiffeners placed at the inside of the cone.

Reference Laminate

The circumference of the cone increases towards the top of the structure, hence the load can be distributed over a larger area. A constant thickness laminate would yield an over-designed structure at the top of the cone, thus a tapered design is implemented by Airbus. Due to confidentiality the reference laminate is not specified.

To limit the mismatch in the coefficient of thermal expansion (CTE) between aluminum and the CFRP material ply angles of 90 degrees are avoided at the ring-cone interface to reduce thermal induced stresses.

The optimization routine only works with symmetric laminates, thereby lay-ups are assumed to be balanced to simplify the optimization for this conceptual work. Altogether the laminate given in Figure 6.2 is used as a QI reference design. Similar to the design from Airbus this design also avoids 90 degree angles at the ring-cone interface. By balanced-symmetric conditions a multiple of four layers have to be used, therefore four sections are implemented to have a similar tapered thickness. The laminate is close to QI, however sections 2 and 3 slightly deviate to assure continuity between the different sections.

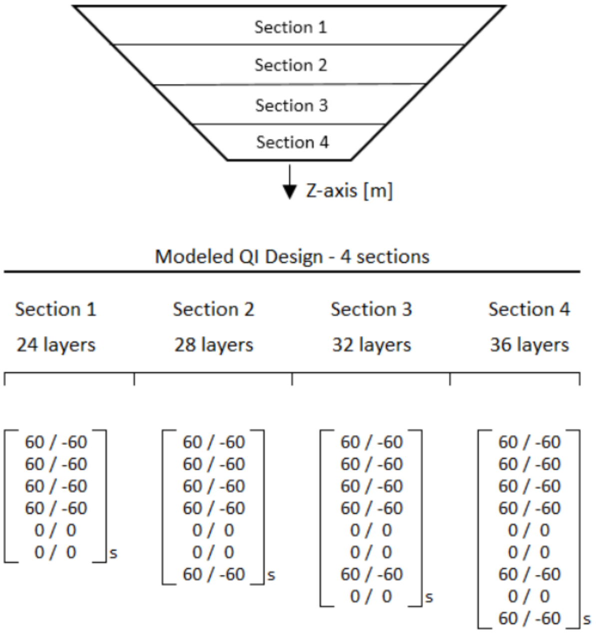

Figure 6.2: Laminate design of the CFRP cone. An QI reference design is used for optimization. The laminate has 4 sections to create the tapered thickness distribtuion. Sections 2 and 3 slight deviate from QI properties to guarantee continuity between sections.

Load and Boundary Conditions

For the design study in this work the load application is simplified to the load case given in Figure 6.3. The main load is the thrust load from the engine in axial direction. The bottom edge of the cone is set to remain horizontal when it displaces. This condition distributes the thrust load over the bottom edge of the cone. The temperature difference is -205 Kelvin at the top of the ring and +5 Kelvin at the bottom of the cone.

To allow the ring to contract and expand by thermal loads it is free to move in the xy-plane. The ring is attached to the rocket bus, thus the top of the ring cannot move in z-direction, i.e. $U_3 = 0$. To impose some of the stiffness of the rocket bus on the ring the rotations are set to zero, i.e. $R_1 = R_2 = R_3 = 0$.

Since the thermal load on the bottom of the cone is negligible the end-cap is not modeled to simplify the finite element analysis. To impose the stiffness of the end-cap on the bottom of the cone the bottom edge cannot expand in the xy-plane and the rotations are set to zero, i.e. $U_1 = U_2 = R_1 = R_2 = R_3 = 0$.

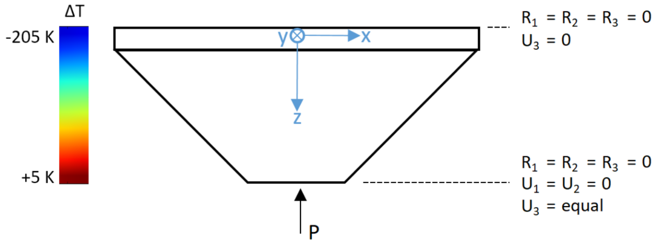

Figure 6.3: The applied load and boundary conditions for the finite element and buckling analysis.

Optimization Problem

The main load on the structure is the axial compressive thrust load, therefore the critical buckling load of the ETF will be the optimization objective. Peak stresses are expected at the ring-cone interface for thermal loads due to the mismatch in CTE. Strength constraints at nodal level could be implemented to avoid first ply failure, however this will put an incredible demand on the computational cost by the large number of constraints involved. The optimization of the ETF fits in a conceptual framework and a single quasi-isotropic compliance constraint is used instead. Although this does not guarantee that first ply failure does not occur excessive deformations and accompanied stresses are limited to some extend. A minimum steering radius of 333mm is applied.

Mesh

For the given load and boundary conditions a mesh convergence study is performed, an overview is given in Table 6.1. The laminate is build from a balanced-symmetric conventional QI stacking sequence. The fiber orientations are measured in the local nodal reference systems which are shown in Figure 6.4. To limit the computational cost the mesh should be as coarse as possible yet generating accurate results. A mesh of [7 + 63] x 63 ($[\mathrm{n}_{\mathrm{ring,axial}}+\mathrm{n}_{\mathrm{cone,axial}}]$ x $\mathrm{n}_{\mathrm{radial}}$) is found acceptable. To study the influence of the number of nodes in the axial and radial directions two extra meshes of [7 + 53] x 73 and [7 + 73] x 53 are generated. The corresponding results show that the accuracy of the model is predominated by the radial mesh refinement, thus a [7 + 53] x 73 is implemented.

Table 6.1: Mesh convergence study for a conventional $[0\ 90\ 45\ \text{-}45]_{b/s}$ laminate. Difference^1 is compared to the [8 + 83] x 83 MATLAB model. Difference^2 is compared to a [11 + 103] x 103 ABAQUS model that uses the S3 element type. This is a 3-node triangular general-purpose shell and a critical buckling load of $\lambda_{cr} = 1.4998e5$ is obtained.

Mesh $[\mathrm{n}_{\mathrm{ring,axial}} + \mathrm{n}_{\mathrm{cone,axial}}]$ x $\mathrm{n}_{\mathrm{radial}}$	λ_{cr}	Difference^1 [%]	Difference^2 [%]
[6 + 43] x 43	1.6798e5	+13.75	+12.00
[6 + 53] x 53	1.5755e5	+6.68	+5.05
[7 + 63] x 63	1.5294e5	+3.56	+1.97
[7 + 73] x 73	1.4987e5	+1.48	-0.73
[8 + 83] x 83	1.4768e5		-1.53
[7 + 53] x 73	1.4866e5	+0.66	-0.88
[7 + 73] x 53	1.6062e5	+8.76	+7.09

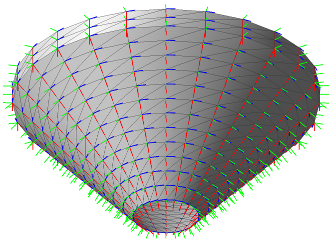

Figure 6.4: Nodal reference systems for a coarse mesh of the MATLAB model. Local 1 and 2 directions are given in red and blue.

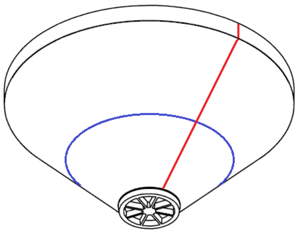

Figure 6.5: Axial (red) and radial (blue) paths used to plot stiffness and stress resultant distributions.

6.1. Results - Constant Thickness Design

Before applying the taper thickness distribution given by Figure 6.2 a constant thickness laminate is modeled first to gain a better understanding of the optimization process. Based on the thickest section a laminate of 36 layers is implemented. By the balanced-symmetric lay-up conditions 9 design layers are optimized and the total laminate is constructed by the linking matrices specified in Chapter 3. The results of a QI-design and optimized VS-design are given in Table 6.2 for a temperature difference of 0 and −200K.

Table 6.2: Results for a constant thickness design for $\Delta T = 0$ and -200K.

Loads		QI-Design		Opt. VS-Design		
ΔT [K]	P [N]	λ_{cr}	Compliance	λ_{cr}	Compliance	Difference in λ_{cr} [%]
0	N.A.	6.31	6.59e2	6.83	5.68e2	8.2
-200	N.A.	6.31	3.07e4	7.12	3.06e4	12.8

6.1.1. Constant Thickness – ΔT = 0K

Due to the axisymmetric model the stress resultant and property distributions in circumferential direction are constant. Hence only the distributions in axial direction specified in Figure 6.5 are studied.

Deformation

Figure 6.6 - The deformation profile primarily shows displacements in radial direction at the ring-cone interface. The transferred loads from the cone to the ring impose out-of-plane loads on the ring known as a kick load, hence radial displacement is present. The displacement profile is slightly smoother for the optimum VS-design.

Stress resultants

Figure 6.7 - Due to force equilibrium in axial direction the N_x distribution does not change for the optimized VS-design. The slightly smoother deformation profile of the optimal VS-design is accompanied by a lower peak stress resultant in hoop direction. Altogether there is no load and stress redistribution visible that increases the buckling performance.

Stiffness

Figure 6.8 - The cause of the increased buckling performance is found in the stiffness distributions. The dominant part of the buckling equation for a simply supported cylinder under an axial compressive load is given by Equation 6.1 [101]. In this equation D_{11} represents axial bending stiffness and D_{22} represents hoop bending stiffness in radial direction. The higher the axial or hoop bending stiffness the higher the resistance against buckling in the corresponding direction. This formulation is for constant stiffness cylinders and not variable-stiffness cones, however the concept of axial and hoop bending stiffness is applicable. The QI-design has a high D_{22} value, therefore the critical buckling mode given in Figure 6.9 is in axial direction. The VS-design shows reduced D_{22} and increased D_{11} values. During optimization the stiffness distribution is changed to yield a critical buckling mode that absorbs the most energy before buckling is initiated. For the optimal design the critical buckling mode given by Figure 6.10 in hoop direction is obtained.

$$F_{66} = D_{11}\left(\frac{m\pi}{L}\right)^4 + 2\left(D_{12} + 2D_{66}\right)\left(\frac{m\pi}{L}\right)^2\left(\frac{n}{R}\right)^2 + D_{22}\left(\frac{n}{R}\right)^4 \tag{6.1}$$

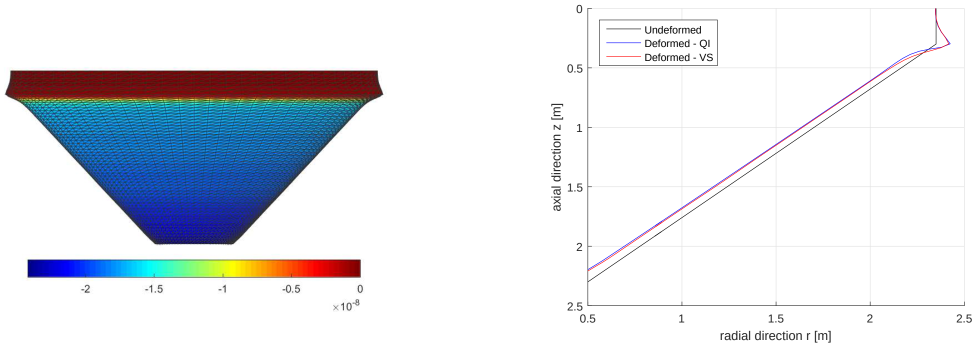

Figure 6.6: Displacement for a constant thickness design for $\Delta T = 0$K, scale = 30. Left: Axial displacement displayed on the total deformed structure. Right: Displacement profile in radial direction.

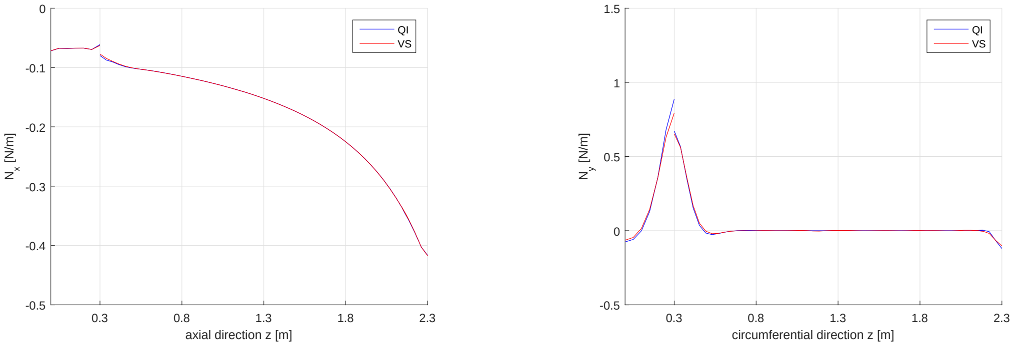

Figure 6.7: Mechanical induced axial ($_x$) and hoop ($_y$) stress resultant distributions in axial direction due to thrust load P for a constant thickness design optimized for ΔT = 0K. The stress resultants are normalized by N_x=N_x/P.

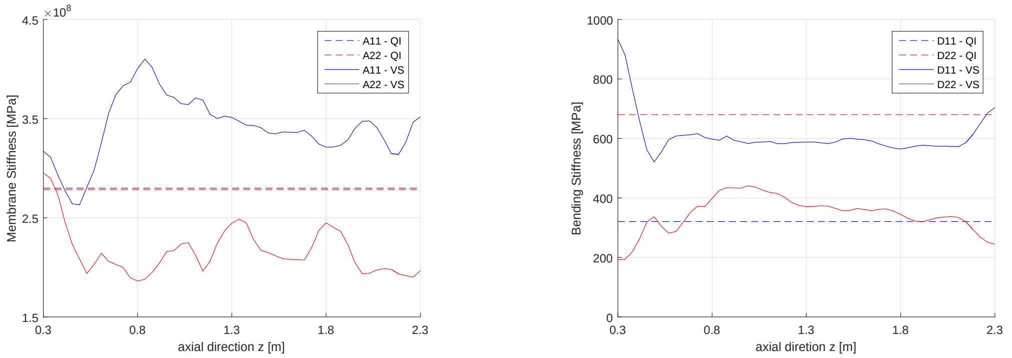

Figure 6.8: The axial membrane (left) and bending stiffness distributions (right) in axial direction for axial ($_{11}$) and hoop ($_{22}$) stiffness for a constant thickness design optimized for ΔT = 0K.

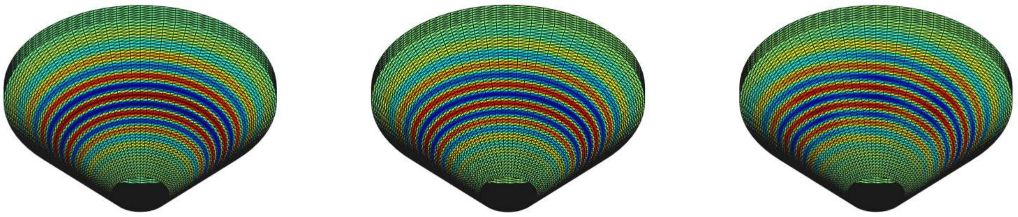

Figure 6.9: Bucking modes ($\lambda_{cr-1,2,7}$ = 6.3125, 6.3144, 6.3567) for a constant thickness QI-design for ΔT = 0K. The 1st buckling mode is purely in axial direction. The 2nd mode has a spiraling pattern. The 2nd to 6th mode are almost similar, hence the 7th mode is plotted because the spiraling pattern is better visible.

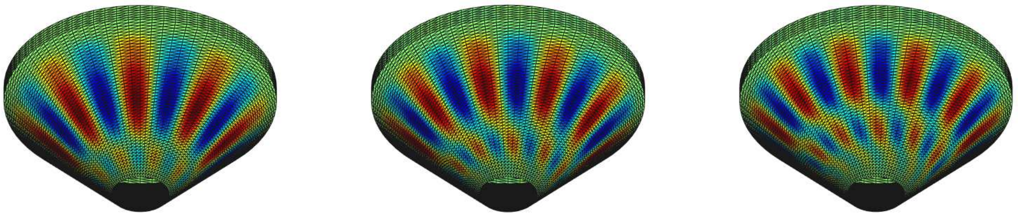

Figure 6.10: First three bucking modes ($\lambda_{cr-1,2,3}$ = 6.8333, 6.8374, 6.8419) for an optimized constant thickness VS-design for ΔT = 0K.

6.1.2. Constant Thickness – ΔT = -200K

The critical buckling load for the QI-design under thermo-mechanical load is similar as the pure mechanical load case. However, the increment in buckling performance is larger for the thermomechanical case. Similar to the previous load case the distributions in axial direction are studied to explain this behavior.

Deformation	Figure 6.11 - The contraction of the aluminum ring by the thermal load is clearly visible, this causes the increment in compliance compared to the pure mechanical load case.
Stress resultants	Figure 6.12 - Similarly to the previous load case the stress resultants due to the mechanical load do not change for the VS-design and do not influence the buckling improvement. Figure 6.13 - The thermal stress resultants are almost zero for the largest part of the structure, indicating free thermal expansion. At the bottom of the cone minor peak stress resultant are induced by the boundary conditions. At the ring-cone interface the mismatch in CTE forces the aluminum ring to contract more in radial direction than the CFRP cone. Consequently tensile hoop stresses are induced in the ring and compression stresses in the cone, however the latter is counteracted by the mechanical tensile peak. The axial stress resultants are negligible, therefore the critical axial buckling mode of the QI-design given in Figure 6.15 is unaffected. For the VS-design the critical buckling modes given in Figure 6.16 are in hoop direction. A minor tensile hoop stress is present below the ring-cone interface, this could explain the larger improvement for the thermomechanical case.
Stiffness	Figure 6.14 - At the ring-cone interface the membrane stiffness of the VS-design is primarily in axial direction, this reduces the mismatch in CTE and explains why the thermal induced stress peak is reduced. Similar to the pure mechanical load case the critical buckling mode is further optimized by altering the membrane and bending stiffness terms.

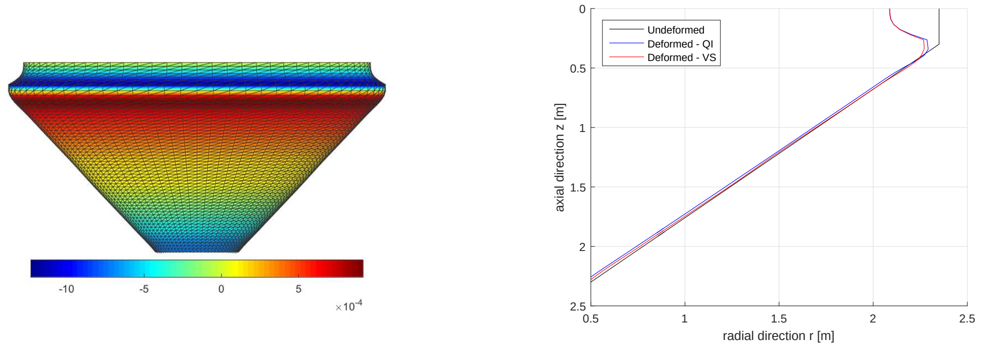

Figure 6.11: Displacement for a constant thickness design for $\Delta T = -200$K, scale = 30. Left: Axial displacement displayed on the total deformed structure. Right: Displacement profile in radial direction.

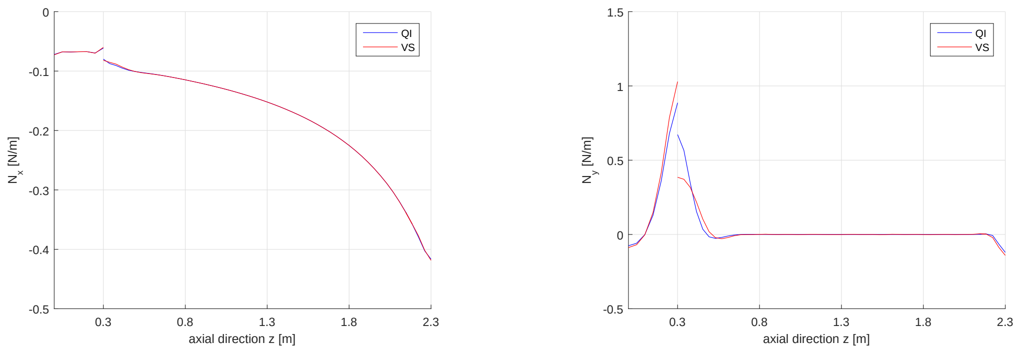

Figure 6.12: Mechanical induced axial (x) and hoop (y) stress resultant distributions in axial direction due to thrust load P for a constant thickness design optimized for $\Delta T = -200$K. The stress resultants are normalized by N_x=N_x/P.

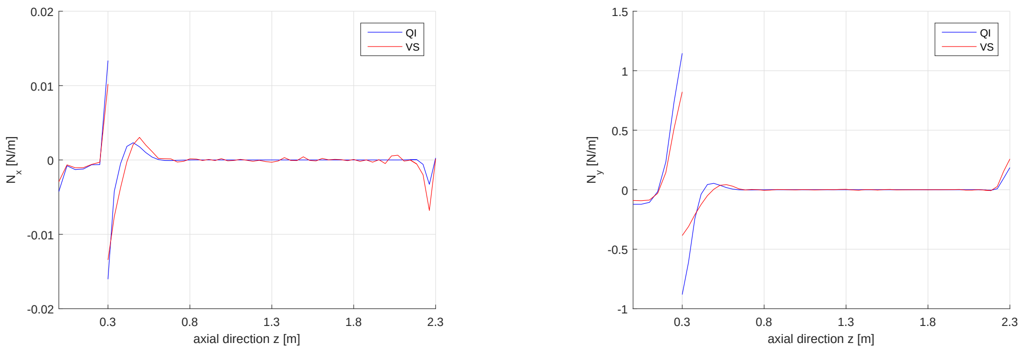

Figure 6.13: Thermal induced axial $(_x)$ and hoop $(_y)$ stress resultant distributions in axial direction due to a temperature difference of −200K for a constant thickness design optimized for $\Delta T = -200$K. The stress resultants are normalized by N_x=N_x/P to make a comparison with the mechanical induced stress resultant distribution.

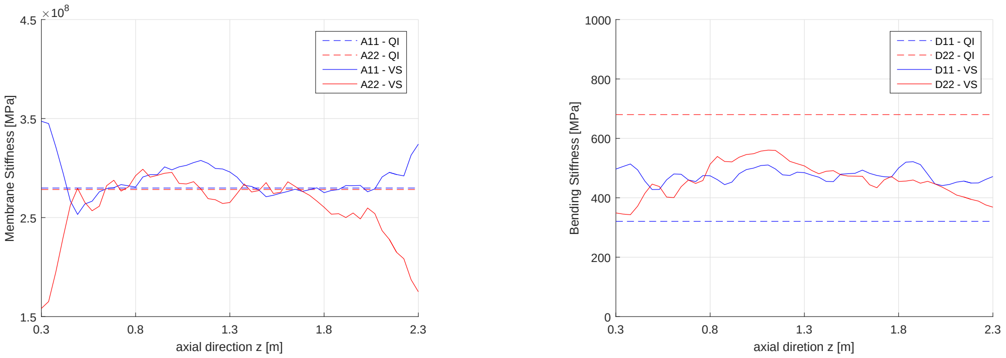

Figure 6.14: The axial membrane (left) and bending stiffness distributions (right) in axial direction for axial $(_{11})$ and hoop $(_{22})$ stiffness for a constant thickness design optimized for $\Delta T = -200$K.

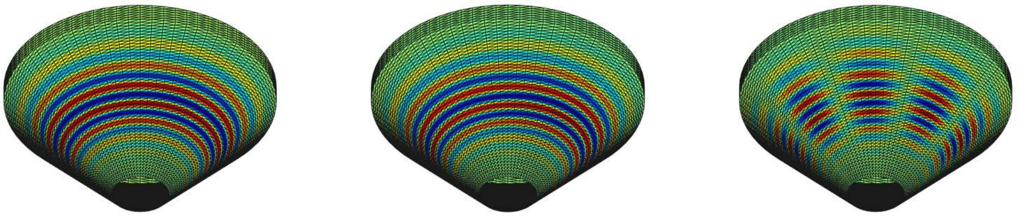

Figure 6.15: Bucking modes ($\lambda_{cr-1,2,8}$ = 6.3125, 6.3144, 6.3572) for a constant thickness QI-design for $\Delta T = -200$K. The 2nd mode has a spiraling pattern. The differences between the 2nd to 7th mode are negligible, hence the 8th mode is plotted showing a combination of axial and hoop buckling.

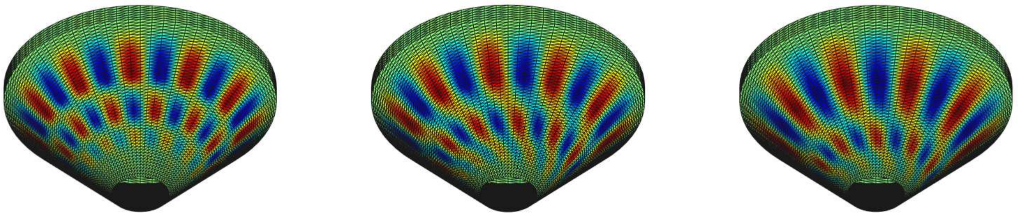

Figure 6.16: First three bucking modes ($\lambda_{cr-1,2,3}$ = 7.1220, 7.1318, 7.1323) for an optimized constant thickness VS-design for $\Delta T = -200$K.

6.2. Results - Tapered Thickness Design

A tapered thickness design in correspondence to Figure 6.2 is optimized for temperature differences of 0 and −200K. The performance of the QI reference design and the optimized VS-design are given in Table 6.3. The optimal VS-designs yield larger performance gains than for found for the optimal constant thickness designs.

Table 6.3: Results for a tapered thickness design for $\Delta T = 0$ and −200K.

Loads		QI-Design		VS-Design		
ΔT [K]	P [N]	λ_{cr}	Compliance	λ_{cr}	Compliance	Difference in λ_{cr} [%]
0	N.A.	3.14	8.68e2	3.56	7.81e2	13.1
-200	N.A.	3.28	3.06e4	3.91	3.06e4	19.2

6.2.1. Tapered Thickness – ΔT = 0K

Compared to the constant thickness design the critical buckling load of the tapered design is almost halved. This is expected since the constant thickness design was over-designed. The tapered design is also axis-symtric, therefore only the distributions in axial direction are studied.

Deformation	Figure 6.17 - The laminate at the top of the cone is thinner, therefore the kick load at the ring-cone interface causes more deformation than the constant thickness designs. Again the optimal VS-design is slightly smoother than the QI-design.
Stress resultants	Figure 6.18 - The influence of the larger deformation by the kick load corresponds to a larger peak in the hoop stress resultant compared to the constant thickness design. By force equilibrium the N_x distribution is unaffected by the tapered thickness. However, the same load has to be carried by a thinner laminate and the top of the cone is now critical for buckling, this is visualized by the critical buckling modes given in Figure 6.20 and Figure 6.21
Stiffness	Figure 6.19 - The influence of the tapered thickness is clearly present in the stiffness distribution and the larger performance gain of the tapered design with respect to the constant thickness design is related to this. The ply-drops of the QI-design are at predefined fiber angles and cause a distinctive stepwise distribution, whereas the VS-design can optimize at what fiber angle a ply is dropped. This allows for a more gradual change between thickness sections. During optimization the stiffness distributions are changed to yield a critical buckling mode that absorbs most energy. The buckling modes of the optimal QI-design and the VS-design are similar, but the critical buckling modes of the optimal VS-design are more spread out corresponding to higher energy absorption. From the stiffness distributions it is also apparent that fiber steering is only active in first two sections, the last two sections are not critical for buckling. Also note that thickness sections 2 and 3 are not fully quasi-isotropic and that the step sizes in the bending stiffness distribution show that every added layer contributes more to the bending stiffness.

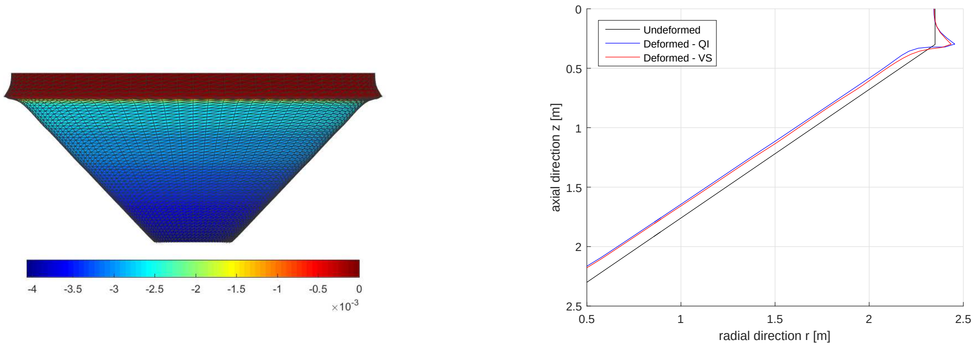

Figure 6.17: Displacement for a tapered thickness design for $\Delta T = 0$K, scale = 30. Left: Axial displacement displayed on the total deformed structure. Right: Displacement profile in radial direction.

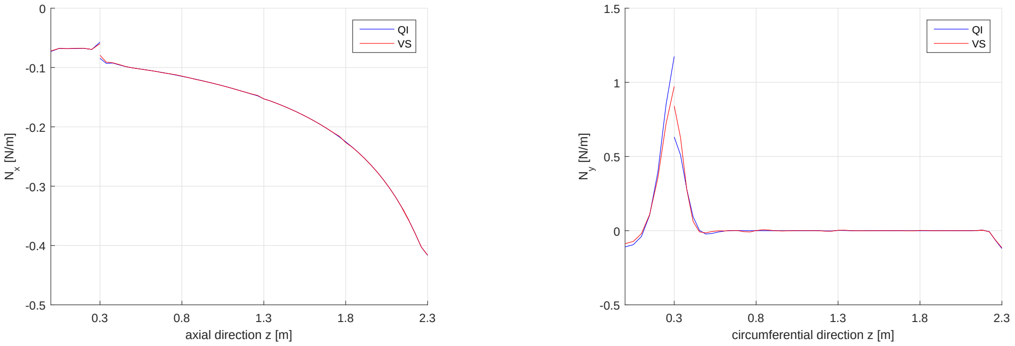

Figure 6.18: Mechanical induced axial (x) and hoop (y) stress resultant distributions in axial direction due to thrust load P for a tapered thickness design optimized for $\Delta T = 0$K. The stress resultants are normalized by N_x=N_x/P.

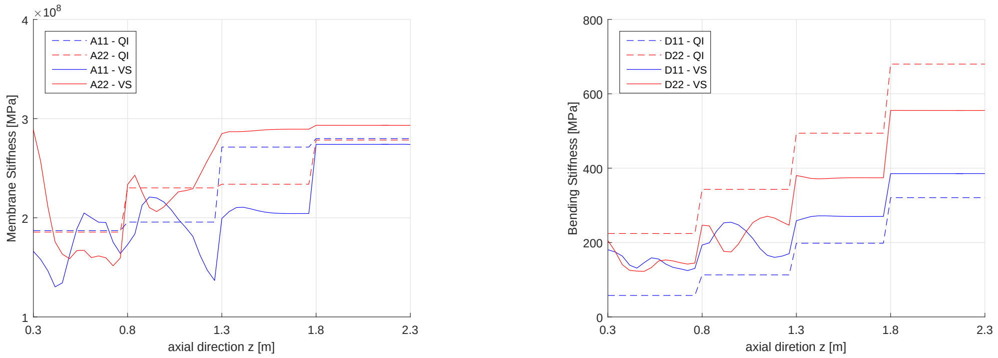

Figure 6.19: The axial membrane (left) and bending stiffness distributions (right) in axial direction for axial ($_{11}$) and hoop ($_{22}$) stiffness for a tapered thickness design optimized for $\Delta T = 0$K.

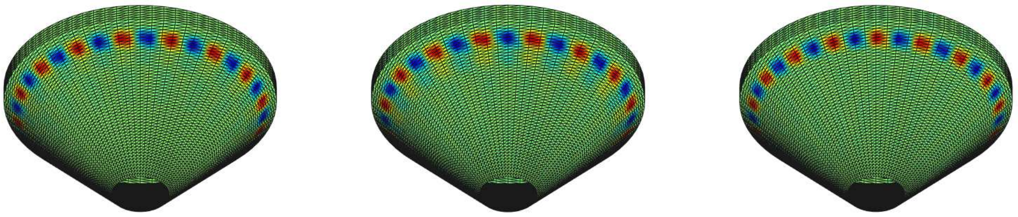

Figure 6.20: First three bucking modes ($\lambda_{cr-1,2,3} = 3.1444, 3.15534, 3.1652$) for an optimized tapered thickness VS-design for $\Delta T = 0$K.

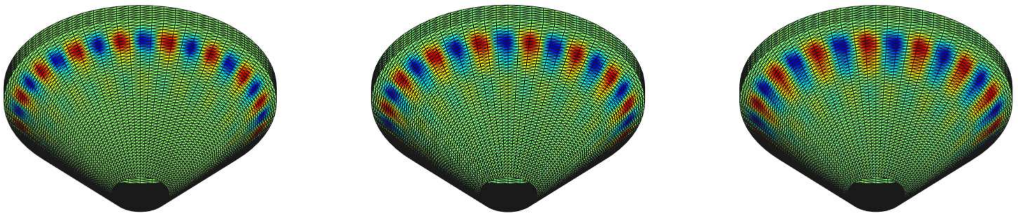

Figure 6.21: First three bucking modes ($\lambda_{cr-1,2,3} = 3.5579, 3.5580,3.5757$) for an optimized tapered thickness VS-design for $\Delta T = 0$K.

6.2.2. Tapered Thickness – ΔT = -200K

The thermomechanical load case yields a larger increment in buckling performance after optimization than the pure mechanical case. Also for this load case the axial distributions are studied.

Deformation	Figure 6.22 - Similar to the thermomechanical constant thickness load application the aluminum ring contracts more by the thermal load than the CFRP cone.
Stress resultants	Figure 6.23 - As with the previous cases the stress resultants induced by the mechanical load do not influence the buckling optimization. Figure 6.24 - The tapered thickness design has a minor influence on the thermal induced stress resultants. Small jumps are visible and they cause the radial deformation variation in the deformation profile. For the VS-design minor tensile hoop stress regions are present at the cone's surface, since the buckling modes in Figure 6.27 are predominantly in hoop direction this could explain the larger improvement for the thermomechanical load case. The reduced stiffness at the top of the CFRP cone lowers the thermal induced peak stresses at the ring-cone interface. The peaks are further reduced by the optimal VS-design.
Stiffness	Figure 6.25 - This reduction in the thermal induced peak stresses originates from the relatively high membrane stiffness at the top of the cone compared to the hoop membrane stiffness. This reduces the mismatch of the CTE between the aluminum ring and CFRP cone. The buckling pattern from the QI-design given by Figure 6.26 is a combination of hoop and axial buckling modes, whereas the optimal buckling modes given by Figure 6.27 are more dominated by hoop buckling. This is in correspondence to the higher axial bending stiffness D_{11} at the top of the cone for the VS-design. During optimization the stiffness is varied to increase the resistance to the critical buckling modes.

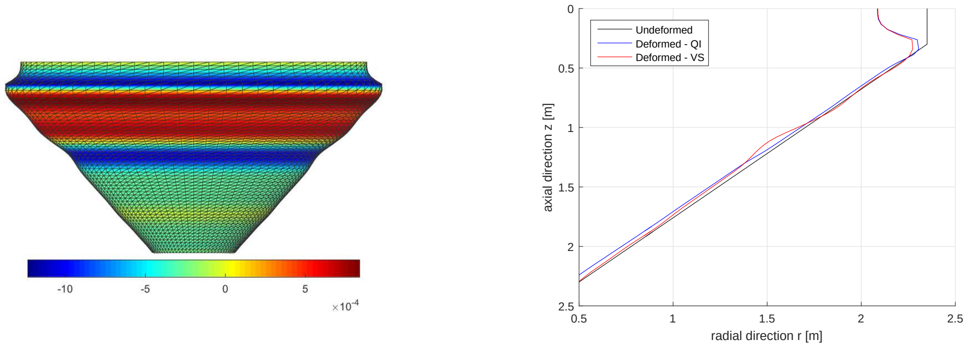

Figure 6.22: Displacement for a tapered thickness design for $\Delta T = -200$K, scale = 30. Left: Axial displacement displayed on the total deformed structure. Right: Displacement profile in radial direction.

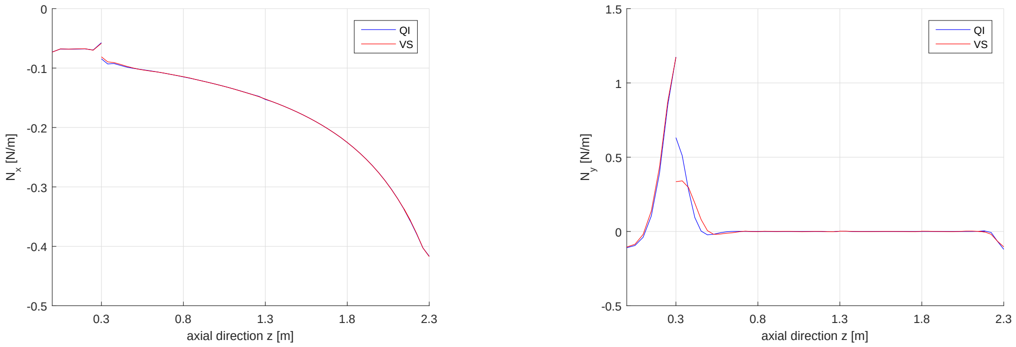

Figure 6.23: Mechanical induced axial (x) and hoop (y) stress resultant distributions in axial direction due to thrust load P for a tapered thickness design optimized for $\Delta T = -200$K. The stress resultants are normalized by N_x=N_x/P.

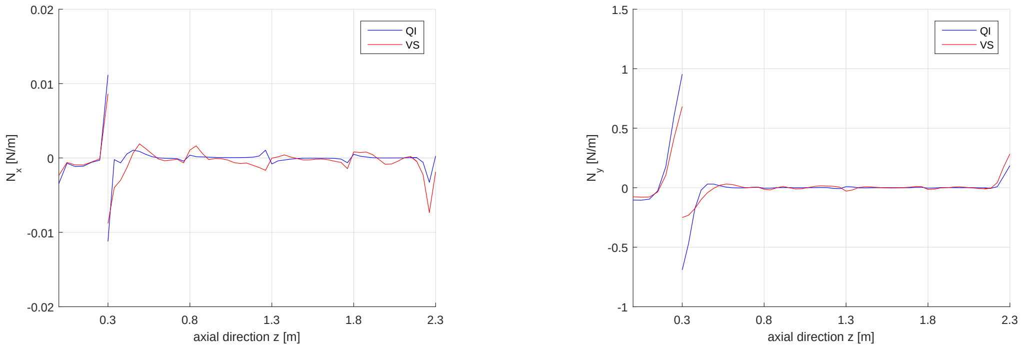

Figure 6.24: Thermal induced axial $(_x)$ and hoop $(_y)$ stress resultant distributions in axial direction due to a temperature difference of −200K for a tapered thickness design optimized for $\Delta T = -200\text{K}$. The stress resultants are normalized by $N_x{=}N_x/P$ to make a comparison with the mechanical induced stress resultant distribution.

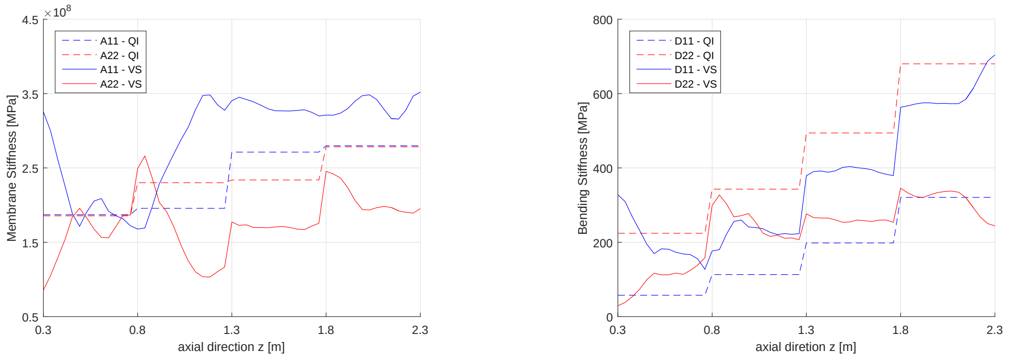

Figure 6.25: The axial membrane (left) and bending stiffness distributions (right) in axial direction for axial $(_{11})$ and hoop $(_{22})$ stiffness for a tapered thickness design optimized for $\Delta T = -200\text{K}$.

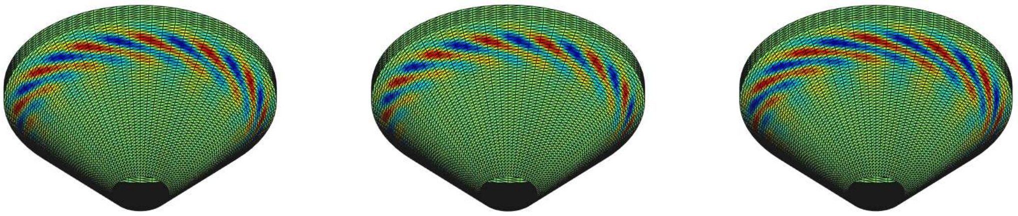

Figure 6.26: First three bucking modes ($\lambda_{cr-1,2,3}$ = 3.2827, 3.2842, 3.2844) for an optimized tapered thickness VS-design for $\Delta T = -200\text{K}$.

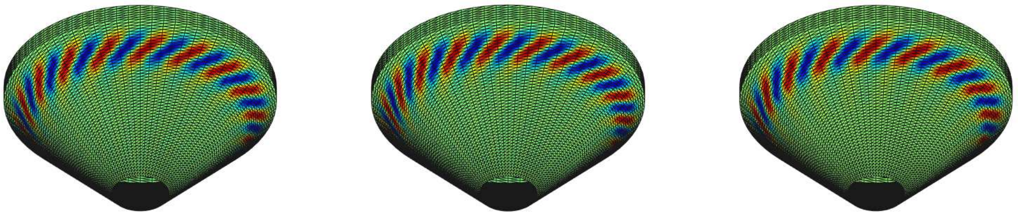

Figure 6.27: First three bucking modes ($\lambda_{cr-1,2,3}$ = 3.9119, 9.2277, 3.9306) for an optimized tapered thickness VS-design for $\Delta T = -200\text{K}$.

6.3. Results - Stiffened Tapered Thickness Design

The original stiffener laminate design is not specified due to confidentiality reasons. To limit computational cost only 8 equally spaced stiffeners are implemented and to emphasize on the influence of the stiffeners the height and stacking sequence of the stiffeners are doubled compared to the reference design. This way the stiffeners have a dominant influence on the optimization process. To properly model inter-stiffener bay buckling more elements are required between the stiffeners, therefore the mesh is refined to [7 + 97] x 63 nodes. Note that the stiffener properties are constant and not optimized. The obtained results are presented in Table 6.4 and higher performance gains are noticable than for the design cases without stiffeners.

Table 6.4: Results for a stiffened tapered thickness design for $\Delta T = 0$ and $-205/+5$K.

Loads		QI-Design		VS-Design		
ΔT [K]	P [N]	λ_{cr}	Compliance	λ_{cr}	Compliance	Difference in λ_{cr} [%]
0	N.A.	2.35	8.86e2	3.42	7.81e2	45.4
-205/+5	N.A.	2.74	2.76e4	3.92	2.74e4	43.2

6.3.1. Stiffened Tapered Thickness Design – ΔT = 0K

For the optimized VS-design an improvement of 45.5% is obtained over the QI-design. Due to the stiffeners the design is no longer axisymmetric and the variations in circumferential direction are studied as well.

Deformation Figure 6.28 - In general the axial displacement of the VS-design is lower than the QI-design. Especially the bay regions close to the top of the cone and the stiffened areas experience less displacement.

Stress resultants Figure 6.29 - The axial N_x distribution at the center of a bay is given. The designs with stiffeners experience lower axial stress resultants than the design without stiffeners. This effect is mostly present at the constrained bottom of the cone. The circumferential N_x distribution at the critical top region of the cone is given for $z = 0.6$m. The plots shows that the VS-design distributes some of the axial compressive stress resultant towards the stiffened areas to relieve the more susceptible bay regions. For the QI-design this relation is opposite, hence the large gain in buckling performance for the optimized design. The distributions of the hoop stress resultants N_y are similar to the tapered thickness design without stiffeners and close to zero along the cone's surface and therefore not shown.

Stiffness Figure 6.30 - The stiffness variations in circumferential direction are shown for $z = 0.6$m. The axial membrane stiffness distribution corresponds to the distribution of axial stress resultants towards the stiffened areas. The critical buckling modes of the QI-design given by Figure 6.31 are dominated in axial direction, whereas the critical buckling modes of the VS-design given in Figure 6.32 are in hoop direction. This corresponds to the increased axial bending stiffness for the VS-design. By the addition of the stiffeners the optimization of the buckling performance is now a combination of global load redistribution and increasing the buckling resistance by optimizing local bending stiffness.

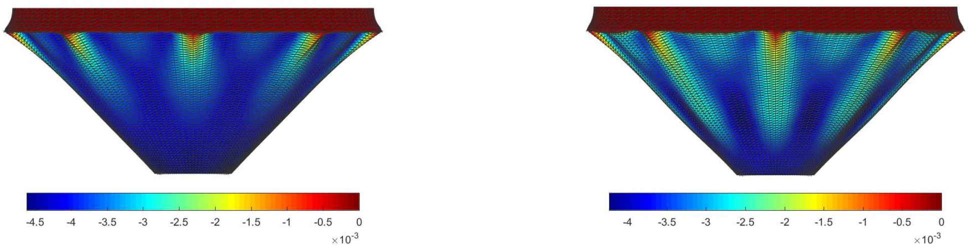

Figure 6.28: Displacement for a stiffened tapered thickness design for $\Delta T = 0$K, scale = 30. Left: Axial displacement displayed on the total deformed structure for the QI-design. Right: Axial displacement displayed on the total deformed structure for the VS-design.

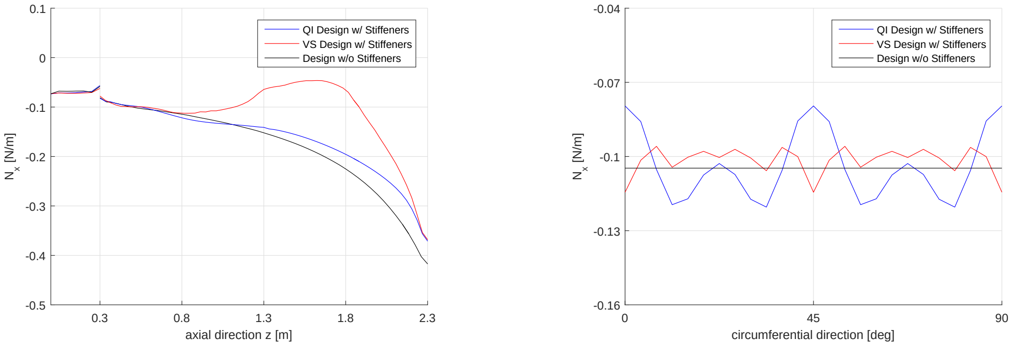

Figure 6.29: Mechanical induced axial stress resultant (N_x) distributions in axial and circumferential direction due to thrust load P for a stiffened tapered thickness design optimized for $\Delta T = 0$K. The stress resultants are normalized by N_x=N_x/P.

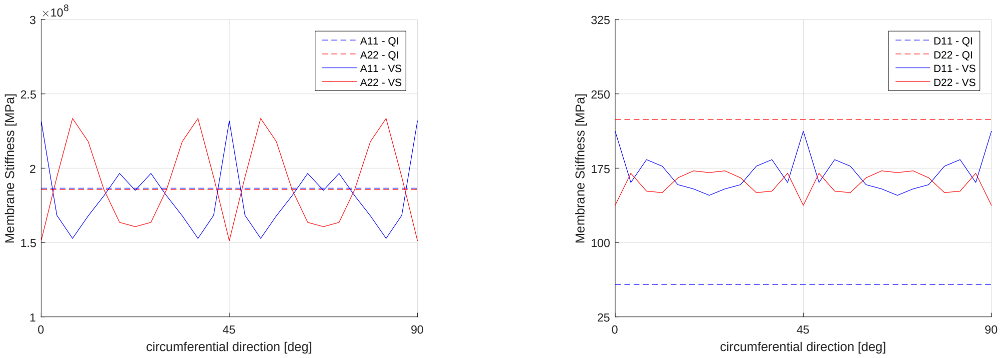

Figure 6.30: The axial $(_{11})$ and hoop $(_{22})$ membrane (left) and bending stiffness distributions (right) in circumferential direction for a tapered thickness stiffened design optimized for $\Delta T = 0$K.

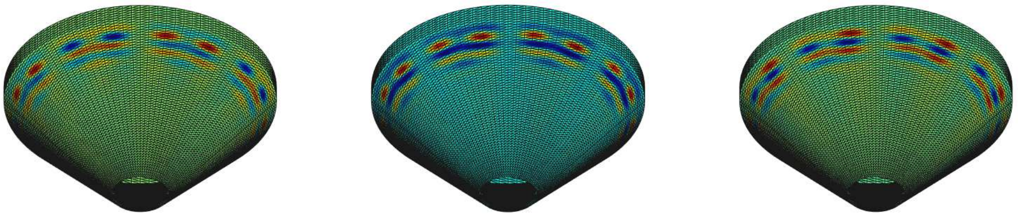

Figure 6.31: First three bucking modes ($\lambda_{cr-1,2,3}$ = 2.3489, 2.3511, 2.5555) for an optimized tapered thickness stiffened VS-design for $\Delta T = 0$K.

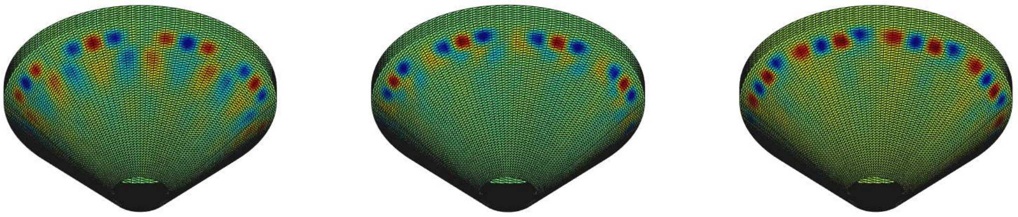

Figure 6.32: First three bucking modes ($\lambda_{cr-1,2,3}$ = 3.3829, 3.4500,3.5055) for an optimized tapered thickness stiffened VS-design for $\Delta T = 0$K.

6.3.2. Stiffened Tapered Thickness Design – ΔT = -205/+5K

For the final design the real thermal load is applied, a linear temperature difference of −205K at the top of the ring to +5K at the bottom of the cone. The VS-design yields a 43.2% improvement over the QI-design. Similar to the previous load case both axial and circumferential variations are studied.

Deformation

Figure 6.33 - The contraction of the aluminum ring is also apparent for this thermomechanical load case. The stiffeners of the VS-design carry more compression load and start to bend slightly outwards, hence the positive displacements.

Stress resultants

Figure 6.34 - The axial stress resultant distribution N_x is similar to the plots given for the pure mechanical load case. Especially at the constrained bottom the compressive axial stress resultant is reduced. However, compression is slightly higher at the bay region than at the stiffened area for $z = 0.6$m, whereas the pure mechanical load case showed a distribution of compression towards the stiffened area.

Figure 6.35 - The axial N_x distribution at the center of a bay is given. In the previous thermal load cases the axial induced stress resultants were negligible due to free thermal expansion. The stiffeners are primarily build from 0 degree oriented fibers and contract less in axial direction than the skin does. Due to this mismatch a stabilizing tension is induced in the bay region and compression in the stiffened area. The optimal VS-design uses this effect to its advantage to improve the buckling performance.

Figure 6.36 - The optimal VS-design lowers the peak stress resultant in hoop direction at the ring-cone interface similar to the previous thermomechanical load cases. Furthermore compressive stresses are distributed towards the stiffened areas to relieve the susceptible bay region.

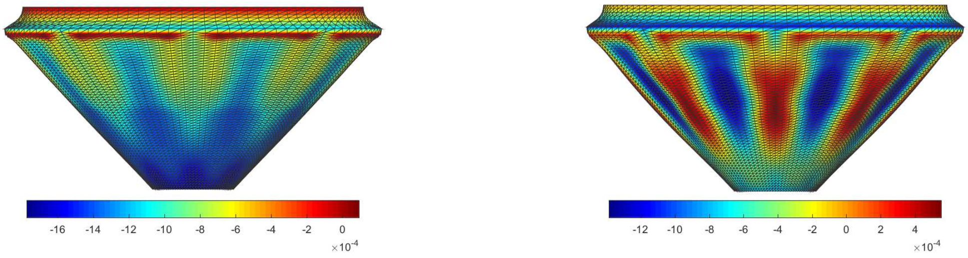

Figure 6.33: Displacement for a stiffened tapered thickness design for $\Delta T = -205/+5$K, scale = 30. Left: Axial displacement displayed on the total deformed structure. Right: Displacement profile in radial direction.

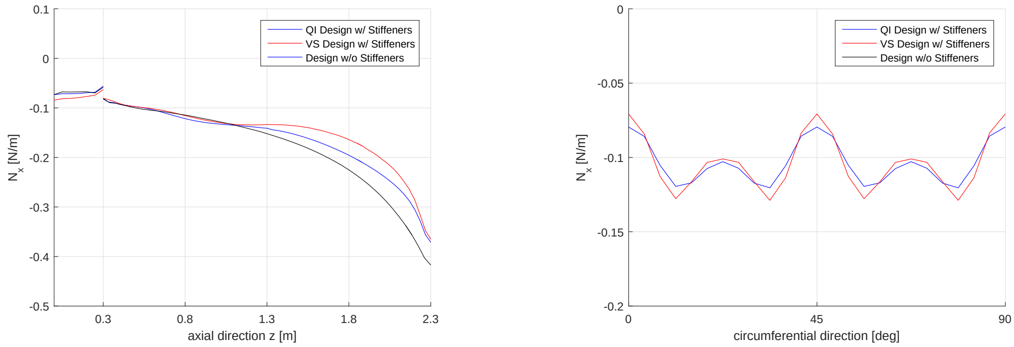

Figure 6.34: Mechanical induced axial stress resultant (N_x) distributions in axial and circumferential direction due to thrust load P for a stiffened tapered thickness design optimized for $\Delta T = -205/+5$K. The stress resultants are normalized by N_x=N_x/P.

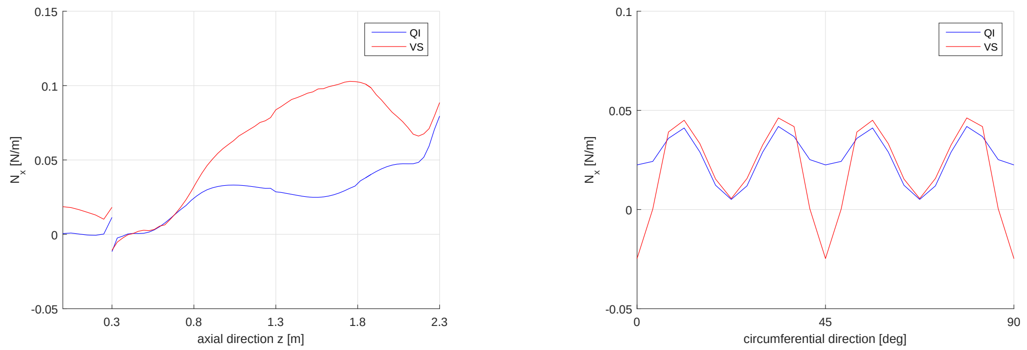

Figure 6.35: Thermal induced axial stress resultant (N_x) distributions in axial and circumferential direction due to a temperature difference of -200K for a tapered thickness design optimized for $\Delta T = -205/+5$K. The stress resultants are normalized by N_x=N_x/P to make a comparison with the mechanical induced stress resultant distribution.

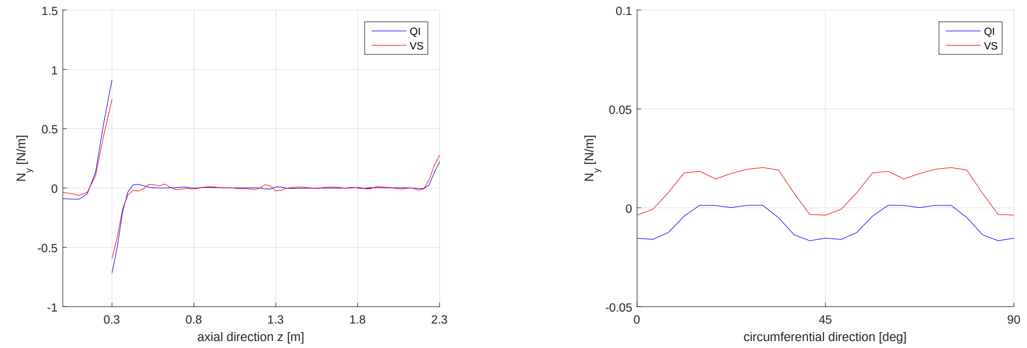

Figure 6.36: Thermal induced axial stress resultant (N_y) distributions in axial and circumferential direction due to a temperature difference of -200K for a tapered thickness design optimized for $\Delta T = -205/+5$K. The stress resultants are normalized by N_x=N_x/P to make a comparison with the mechanical induced stress resultant distribution.

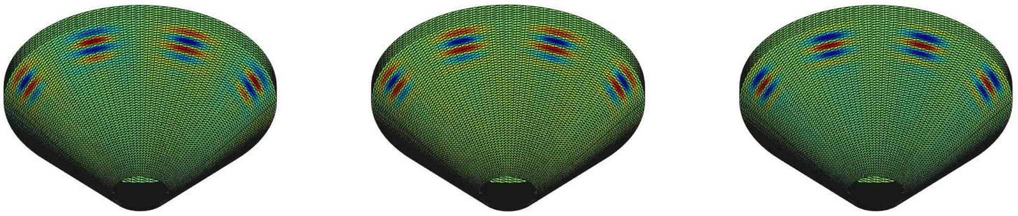

Figure 6.37: First three bucking modes ($\lambda_{cr-1,2,3}$ = 2.7404, 2.7408, 2.7532) for an optimized stiffened tapered thickness VS-design for $\Delta T = -205/+5$K.

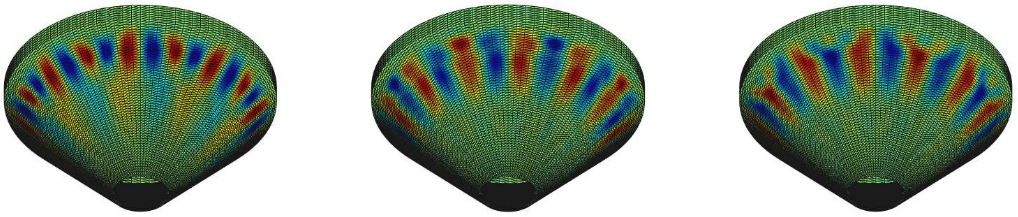

Figure 6.38: First three bucking modes ($\lambda_{cr-1,2,3}$ = 3.9239, 3.9834, 4.0102) for an optimized stiffened tapered thickness VS-design for $\Delta T = -205/+5$K.

Stiffness

Figure 6.39 - At the center of the bay the hoop membrane stiffness increases and the axial membrane stress decreases. This leads to a larger difference in the CTE between the stiffened area and the bay region, causing the induced tension in the bay. The QI-design has high hoop bending stiffness, therefore the critical buckling modes given in Figure 6.37 are in axial direction. Compared to the QI-design the bending stiffness in axial direction is increased and in hoop direction decreased for the VS-design. This leads to the critical hoop buckling modes given in Figure 6.38.

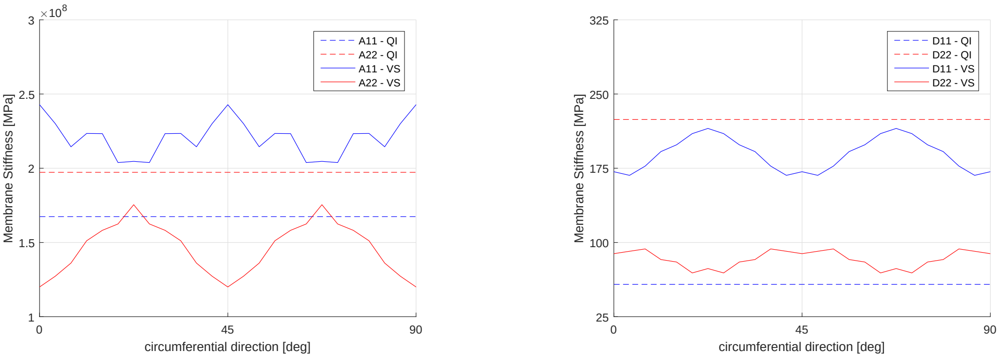

Figure 6.39: The axial $(_{11})$ and hoop $(_{22})$ membrane (left) and bending stiffness distributions (right) in circumferential direction for a stiffened tapered thickness design optimized for $\Delta T = -205/+5$K.

Corresponding Fiber Paths

The results show that the optimization process is a balance between distributing the mechanical and thermal loads and optimizing the local stiffness to increase buckling resistance. To indicate the fiber angle variation the third step of the multi-step framework is applied to construct the corresponding fiber paths by the streamline analogy.

The closed structure of the ETF doesn ot provide sufficient inflow and outflow boundaries to perform the streamline analogy. To circumvent this problem a cut is made over the length of the mesh-model. At this cut the nodes and properties are duplicated and the element connectivity matrix is adjusted to create an open structure. Based on the open structure the in- and outflow boundaries are determined. The difference between the closed and open structure is illustrated in Figure 6.40. The elements adjacent to the boundaries are indicated yellow, and the in- and outflow corner elements are indicated blue.

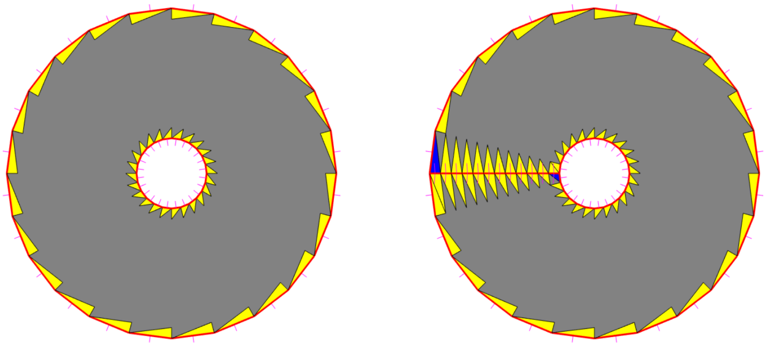

Figure 6.40: Closed structure (left): Only two in- and outflow boundaries are present. Open structure (right): By making a cut over the length four in- and outflow boundaries are present.

With the additional boundaries the fiber paths are constructed. In Figure 6.41 to Figure 6.44 the fiber paths are given for plies 3, 4, 6 and 7 respectively. The fiber paths of the other plies are similar and omitted for the sake of brevity. Note that ply 7 is smaller due to a ply-drop in the first thickness section. The cut over the length of the structure is visible and some minor deterioration is present. The symmetric design due to the stiffeners is clearly visible as well.

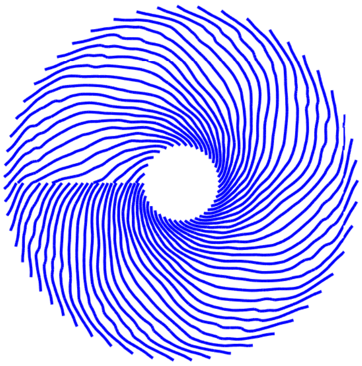

Figure 6.41: Fiber Paths of ply 3.

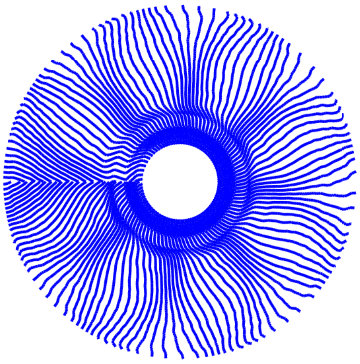

Figure 6.42: Fiber Paths of ply 4.

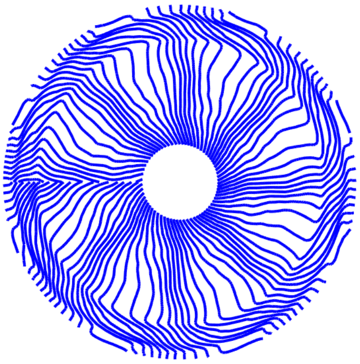

Figure 6.43: Fiber Paths of ply 6.

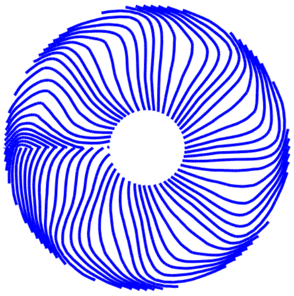

Figure 6.44: Fiber Paths of ply 7.

Manufacturing
The automated fiber placement machines cannot use the given fiber paths directly. A post-processing step is required to determine the actual tow placement which does not yield an unique relation. This is considered an optimization problem in itself, since tow-drop and overlap placement techniques influence the properties of the laminate.

Final Remarks
The focus of the conceptual design study presented in this chapter is to research the potential of a variable-stiffness laminate design for the engine thrust frame, therefore significant simplifications are made to the design problem.

One of the main simplifications is the implemented stiffener composition. In reality more stiffeners will be present leading to smaller bay regions. This will limit the amount of steering and corresponding load re-distribution in circumferential direction. Additional simplifications are related to the load conditions and geometry. For example manholes, actuator loads and imposed forces by equipment are ignored. Furthermore the ring-cone interface is not accurately modeled and strength is not assessed.

The obtained results show great potential with significant performance gains. However, creating a more accurate representation could strongly influence the design result. Consequently the obtained results should be interpreted with care.

7

Conclusion

The first research objective is the implementation of thermal loads in the laminate analysis and optimization framework. The second research objective is to apply the updated framework to perform conceptual design optimization of the engine thrust frame under thermomechanical loads. Conclusions are drawn related to these objectives in sections 7.1 and 7.2 respectively.

7.1. Thermomechanical Optimization Framework

Thermal load is implemented successfully in the composite laminate, finite element and buckling analysis. Implementation of thermal load is verified by a simply supported rectangular plate under uniform end shortening subject to thermomechanical loads. Buckling analysis of constant stiffness laminates and a variable-stiffness laminate with linearly varying fiber paths yield the correct critical buckling loads.

Sequential local approximations of structural responses are used in the optimization routine. These response approximations are updated to include the influence of thermal loads. Based on the thermomechanical governing equations a new set of sensitivities are derived for strength and buckling responses to build the updated local approximations. The sensitivities of the buckling response are implemented in the optimization framework and verified by the second order central finite difference approximation to yield correct results.

The same rectangular plate is used to demonstrate the optimization behavior of the updated framework. Similar trends to improve buckling resistance as the reference study are found. The optimized variable-stiffness laminate design distributes the applied loads towards the constrained edges to increase the buckling performance. A negative temperature difference leads to stabilizing tensile stress resultants in the prone to buckling center area, hence for negative temperature differences a better buckling performance is obtained than for pure mechanical load conditions.

Although the optimization trend is similar the critical mechanical buckling load differs from the reference study. The optimization in the reference study is performed in the lamination parameter space and is not converted to fiber angles, whereas the optimization in this works is performed in the fiber angle design space with a steering constraint. Relaxing the minimum steering radius from 500mm to 250mm yields closer resemblance with the reference report, reducing the difference from -41% to -18% respectively.

7.2. Engine Thrust Frame Application

The results of the conceptual design optimization of a constant thickness, tapered thickness and stiffened tapered thickness design are repeated in Table 7.1 for a minimum steering radius of 333mm. For all designs tensile peak loads are present at the ring-cone interface due to geometry induced kick load. Additionally thermal induced compressive stress resultants are present due to the mismatch in the coefficient of thermal expansion between the aluminum ring and CFRP cone. The tensile and compression stress resultants counteract each other, thereby the peaks in thermal induced compressive stress resultants are reduced for all thermomechanical optimization cases.

Table 7.1: Results for a constant thickness (CT), tapered thickness (TT) and stiffened tapered thickness (STT) designs for different thermomechanical load cases.

Design	ΔT [K]	λ_{cr} - QI	λ_{cr} - VS	Difference in λ_{cr} [%]
CT	0	6.31	6.83	8.2
CT	-200	6.31	7.12	12.8
TT	0	3.14	3.56	13.1
TT	-200	3.28	3.91	19.2
STT	0	2.35	3.42	45.4
STT	-205/+5	2.74	3.92	43.2

The constant and tapered thickness designs are axisymmetric designs and load redistribution is not possible. Since the stiffness in circumferential direction is constant most of the structure exhibits free thermal expansion, hence the influence of thermal load is limited. The laminate stiffness in axial direction is varied to increase resistance to the critical buckling modes. Due to this behavior other buckling modes become more dominant until one of these modes becomes critical. This process continues until two or more buckling modes are dominant and changing the design will only cause one of the buckling modes to initiate at a lower load.

For constant thickness laminates increments around 10% are found for an optimized variable-stiffness laminate. For tapered thickness laminates the thinner upper section of the cone is critical and improvements around 15% are obtained.

The stiffened design has stiffened areas and load can be redistributed in circumferential direction, this adds more freedom to tailor the design. For the pure mechanical load case the optimal variable-stiffness laminate distributes the compressive stresses towards the stiffened areas. The optimal variable-stiffened design of the thermomechanical load case uses a mismatch in thermal expansion between the bay and stiffened regions. The bay region contracts more than the stiffened areas by a negative thermal load, thus stabilizing tensile stress resultants are induced in the prone to buckling bay regions. With the additional tailoring freedom by influencing the load distributions larger improvements around 45% are obtained for the optimized variable-stiffness laminates.

Albeit the improvements are significant the given results should be interpreted with care. A simplified model of the engine thrust frame is applied. For example a simplified stiffened design is used, manholes are not present and loads exerted by actuators and equipment are not evaluated. Furthermore fiber paths are obtained, but these are not related to actual tow placement. Therefore manufacturing influences like local gaps and overlaps are not included. Recommendations how to improve the engine thrust frame model and optimization framework for future research are given in the next chapter.

8

Recommendations

In this work the existing framework is expanded to incorporate thermomechanical load conditions. In section 8.1 general recommendations about the thermomechanical optimization framework are suggested for future work. With the updated framework a conceptual design optimization of the ETF was executed. Recommendations for future research are stated in section 8.2 for this specific load case.

8.1. Thermomechanical Optimization Framework

Several recommendations to improve the thermomechanical optimization framework for future research are given:

Thickness Optimization

It is mentioned before that ply densities are implemented in the thermal analysis to prepare for thickness optimization. Furthermore the density approximation is updated in the framework to incorporate influences of thermal loads, however it is not yet verified. To increase design flexibility the density approximation should be verified and thickness optimization and ply angle optimization can be combined by the integrated coordinate descent algorithm.

Strength Implementation

The thermomechanical sensitivity analysis of strength response is performed, but not yet implemented within the optimization framework. To use strength as a constraint or objective for future applications subject to thermomechanical load conditions the optimization framework should be updated and verified.

Run Time

For geometrically complicated designs such as the ETF long run times become evident, especially for refined meshes. If complex geometries have to be modeled for future research it is advised to investigate the bottlenecks of the analysis and optimization algorithm and to investigate if more efficient code structures can be programmed to reduce computational cost.

8.2. Engine Thrust Frame Application

To stay within the research scope several model simplifications are made to the ETF. Some recommendations are given to improve the resemblance with reality in future work. Other suggestions are given to improve the optimization design problem of the ETF application.

Thickness Optimization

Variable thickness is important in the engine thrust frame application and a tapered thickness is applied to reduce weight. To further tailor the design thickness optimization could be applied in future work.

Strength Constraints

It is known that peak stress resultants are present at the ring-cone interface. In this work a stiffness constraint is applied to limit excessive deformation and corresponding stresses to some extend. As mentioned before this does not guarantee that first ply failure does not occur. Strength constraints are not implemented in this work due to high computational cost. Applying strength constraints only at critical regions could limit the computational cost and ensure first ply failure does not occur.

Ring-Cone Interface

For both thermal and mechanical loads peak stress resultants occur at the ring-cone interface. It is known that the modeled aluminum ring is simplified from a more complex design that reduces the peak loads at the interface. To improve the model the ring should be modeled more accurately. Thereby shape optimization of ring-cone interface could be applied to improve load transfer. Together with the optimization of the variable-stiffness laminate design this should be an integral optimization process, since the shape and variable-stiffness laminate design are interdependent.

Stiffeners

A simplified stiffened design is used to limit the required mesh density. Thereby the stiffeners are doubled in height and thickness to increase the influence on the laminate optimization. To increase the accuracy of the model the correct stiffened design should be implemented. Fiber steering in radial direction will be limited by the smaller inter-stiffener bays. Ideally the stiffened design is an integral part of the optimization process, since the stiffened design strongly influences the optimal variable-stiffness laminate design.

Additional Details

To improve the ETF model additional details should be modeled to better represent reality. Multiple manholes are present in the conical part and adding these will improve the geometric representation. Load conditions are represented more accurate if loads exerted by equipment and actuators are included. Adding such details will add asymmetries to the model and this will influence the optimal design.

Design Rules

At last it is recommended to apply additional design rules in future work. Based on experience design rules are applied by designers to improve certain properties of laminates. For example minimal and maximal angle variation between adjacent plies are often applied to non-conventional laminate designs.

Bibliography

[1] U.S. Department of Transportation - Bureau of Transportation Statistics. 2014 airline financial data. `http://www.rita.dot.gov`, 2015. Accessed: 13-08-2016.

[2] J.J. Lee, S.P. Lukachko, I.A. Waitz, and A. Schafer. Historical and future trends in aircraft performance, cost and emissions. *Annual Reviews, Energy and Environment*, 2001.

[3] S. Viguet-Carrin, P. Garnero, and P.D. Delmas. The role of collagen in bone strength. *Osteoporosis International*, 17, Issue 3:319–336, 2006.

[4] A. J. Stamm. *Wood and cellulose science.* Ronald Press Co., 1964.

[5] A.K. Kaw. *Mechanics of Composite Materials*, chapter Introduction to Composite Materials, pages 1–16. Taylor and Francis Group, 2nd edition, 2006.

[6] C. Kassapoglou. *Design and Analysis of Composite Structures - With Applications to Aerospace Structures.* John Wiley and Sons, Ltd., 1st edition, 2010.

[7] R.M. Jones. *Mechanics of Composite Materials.* McGraw-Hill Book Company, 1st edition, 1975.

[8] M.W. Hyer and R.F. Charette. Use of curvilinear fiber format in composite structure design. *Composite Structures*, 29, Issue 6: 1011–1015, 1989.

[9] M.W. Hyer and H.H. Lee. The use of curvilinear fiber format to improve buckling resistance of composite plates with central circular holes. *Composite Structures*, 18:239–261, 1991.

[10] C.G. Grant. *Bridging the Centuries with SAMPE's Materials and Processes Technoglogy*, chapter Fiber Placement Process Utilization within the Worldwide Aerospace Industry, pages 709–720. Taylor and Francis Group, 2nd edition, 2000.

[11] K.C. Wu, B.F. Tatting, and Z. Gurdal. Structural response of compression-loaded, tow-placed, variable stiffness panels. *American Institute of Aeronautics and Astronautics, Inc.*, 43th Structures, Structural Dynamics and Materials Conference. Denver, Colorado, 2002.

[12] D.C. Jegley, B.F. Tatting, and Z. Gurdal. Optimization of elastically tailored tow-placed plates with holes. *American Institute of Aeronautics and Astronautics, Inc.*, 44th Structures, Structural Dynamics and Materials Conference, 2003.

[13] D.C. Jegley, B.F. Tatting, and Z. Gurdal. Tow-steered panels with holes subjected to compression or shear loading. *American Institute of Aeronautics and Astronautics, Inc.*, 2005.

[14] Z. Gurdal and R. Olmedo. Composite laminates with spatially varying fiber orientations: "variable stiffness panel concept". *33rd Structures, Structural Dynamics and Materials Conference - Dallas Texas*, 1992.

[15] Z. Gurdal and R. Olmedo. In-plane response of laminates with spatially varying fiber orientations: Variable stiffness concept. *American Institute of Aeronautics and Astronautics, Inc.*, 31, No. 4:751–758, 1993.

[16] Z. Gurdal, B.F. Tatting, and C.K. Wu. Variable stiffness composite panels - effect of stiffness variation on the in-plane and buckling response. *Composites Part A, Applied Science and Manufacturing*, 39, Issue 5:911–922, 2007.

[17] Z. Gurdal and R. Olmedo. Buckling response of laminates with spatially varying fiber orientations. *34th Structures, Structural Dynamics and Materials Conference - La Jolla California*, 1993.

[18] S.T. IJsselmuiden. *Optimal Design of Variable Stiffness Composite Structures Using Lamination Parameters.* PhD thesis, Delft University of Technology, 2011.

[19] D.O. Evans. *Handbook of Composites*, chapter Fiber Placement. Chapman and Hall, 2nd edition, 1998.

[20] C.S. Lopes, Z. Gurdal, and P.P. Camanho. Variable-stiffness composite panels: Buckling and first-ply failure improvements over straight-fibre laminates. *Computer and Structures*, 86, Issue 9:897–907, 2008.

[21] Coriolis Composites. Fiber placement robots. `http://www.coriolis-composites.com`, 2016. Accessed: 20-05-2016.

[22] B.C. Kim, P.M., P. Weaver, and K. Potter. Continuous tow shearing for manufacturing variable angle tow composites. *Composites Part A: Applied Science and Manufacturing*, 43, Issue 8:1347–1356, 2012.

[23] B.C. Kim, K. Hazra, P. Weaver, and K. Potter. Limitations of fibre placement techniques for variable angle tow composites and their process-induced defects. *Proceedings of the 18th International Conference on Composite Materials*, 2011.

[24] S. Nagendra, S. Kodyalam, and J.E. Davis. Optimization of tow fiber paths for composite design. *American Institute of Aeronautics and Astronautics, Inc.*, 36th Structures, Structural Dynamics and Materials Conference, 1995.

[25] Z. August, G. Ostrander, J. Michasiow, and D. Hauber. Recent developments in automated fiber placement of thermoplastic composites. *Society for the Advancement of Material and Process Engineering Journal*, 50, Issue 2, 2014.

[26] A.B. Strong. *Fundamentals of Composites Manufacturing: Materials, Methods, and Applications*, volume 1st. Society of Manufacturing Engineers, 2008.

[27] J. Mondo and K. Parfrey. Performance of in-situ consolidated thermoplastic composite structures. *Proceedings of the 27th International SAMPE Technical Conference*, pages 361–370, 1995.

[28] J. Tierney and J.W. Gillespie. Modeling of heat transfer and void dynamics for the thermoplastic composite tow-placement process. *Journal of Composite Materials*, 37, Issue 19:1745–1768, 2003.

[29] M.A. Lamontia, M.B. Gruber, J. Tierney, J.W. Gillespie, B.J. Jensen, and R.J. Cano. Modeling the accudyne thermoplastic in situ atp process. *Proceedings of The Society for the Advancement of Material and Process Engineering Conference*, 2009.

[30] M.B. Gruber, I.Z. Lockwood, L.T. Dolan, S.B. Fucnk, J. Tierney, J.W. Gillespie, P. Simacek, S.G. Advani, B.J. Jensen, R.J. Cano, and Grimsley B.W. Thermoplastic in situ placement requires better impregnated tapes and tows. *Proceedings of The Society for the Advancement of Material and Process Engineering Conference*, pages 2164–2178, 2012.

[31] M.A. Lamontia, M.B. Gruber, J. Tierney, J.W. Gillespie, B.J. Jensen, and R.J. Cano. In situ thermoplastic atp needs flat tapes and tows with few voids. *Proceedings of The Society for the Advancement of Material and Process Engineering Conference*, 2009.

[32] Z. Gurdal and B.F. Tatting. Automated finite element analysis of elastically-tailored plates. Technical report, National Aeronautics and Space Administration - Langley Research Center, 2003.

[33] Z. Gurdal, B.F. Tatting, and K.C. Wu. Tow-placement technology and fabrication issues for laminated composite structures. *American Institute of Aeronautics and Astronautics, Inc.*, 46th Structures, Structural Dynamics and Materials Conference, 2001.

[34] K. Croft, L. Lessard, D. Pasini, M. Hojjati, J. Chen, and A. Yousefpour. Experimental study of the effect of automated fiber placement induced defects on performance of composite laminates. *Composites: Part A*, 42:484–491, 2011.

[35] S. Nagendra, S. Kodiyalam, J.E. Davis, and V. Parthasarathy. Optimization of tow fiber paths for composite design. *American Institute of Aeronautics and Astronautics, Inc.*, 36th Structures, Structural Dynamics and Materials Conference, 1995.

[36] P. Pedersen. On thickness and orientational design with orthotropic materials. *Structural Optimization*, 3:69–78, 1991.

[37] P. Pedersen. Examples of density, orientation, and shape-optimal 2d-design for stiffness and/or strength with orthotropic materials. *Structural Multidisciplinary Optimization*, 26:37–49, 2004.

[38] S. Setoodeh and Z. Gurdal. Design of composite layers with curvilinear fiber paths using cellular automata. *American Institute of Aeronautics and Astronautics, Inc.*, 44th Structures, Structural Dynamics and Materials Conference. Norfolk, Virginia, 2003.

[39] M.M. Abdalla and Z. Gurdal. Structural design using optimality based cellular automata. *American Institute of Aeronautics and Astronautics, Inc.*, 43th Structures, Structural Dynamics and Materials Conference. Denver, Colorado, 2002.

[40] S. Setoodeh, M.M. Abdalla, and Z. Gurdal. Combined topology and fiber path design of composite layers using cellular automata. *Structural Multidisciplinary Optimization*, 30:413–421, 2005.

[41] S. Venkataraman and R.T. Haftka. Optimization of composite panels - a review. *American Society of Composites*, 14th International Conference Proceedings:479–488, 1999.

[42] M. Bruyneel. Optimization of laminated composite structures: Problems, solution procedures and applications. *Composite Materials Research Progress*, pages 51–107, 2008.

[43] C. Waldhard, Z. Gurdal, and C. Ribbens. Analysis of tow placed, parallel fiber, variable stiffness laminates. *37th Structures, Structural Dynamics and Materials Conference - Salt Lake City Utah*, pages 2210–2220, 1996.

[44] C.S. Lopes, Z. Gurdal, and P.P. Camanho. Tailoring for strength of composite steered-fibre panels with cutouts. *Composites: Part A*, pages 1760–1767, 2010.

[45] S.T. Pinho, C.G. Davila, P.P. Camanho, L. Iannucci, and P. Robinson. Failure models for frp under in-plane or three-dimensional stress states including shear non-linearity. Technical report, National Aeronautics and Space Administration - Langley Research Center, 2005.

[46] A.W. BLOM, C.S. Lopes, P.J. Kromwijk, Z. Gurdal, and P.P. Camanho. A theoretical model to study the influence of tow-drop areas on the stiffness and strength of variable-stiffness laminates. *Journal of Composite Materials*, 43, Issue 5:484–491, 2009.

[47] Z. Gurdal and B.F. Tatting. Design and manufacture of elastically tailored tow placed plates. Technical report, National Aeronautics and Space Administration - Langley Research Center, 2005.

[48] M.W. Weaver, H. Kalyan, M.A.R. Saverymuthapulle, and M.T. Hawthorne. Buckling of variable angle tow plates: from concept to experiment. *American Institute of Aeronautics and Astronautics, Inc.*, 50th Structures, Structural Dynamics and Materials Conference. Palm Springs, California, 2009.

[49] A.W. Blom, B.F. Tatting, M.A.M. Hol, and Z. Gurdal. Path definitions for elastically tailored conical shells. *American Institute of Aeronautics and Astronautics, Inc.*, 47th Structures, Structural Dynamics and Materials Conference. Newport, Rhode Island, 2006.

[50] A.W. Blom, B.F. Tatting, M.A.M. Hol, and Z. Gurdal. Fiber path definitions for elastically tailored conical shells. *Composites: Part B*, 40:77–84, 2009.

[51] A.W. Blom, S. Setoodeh, M.A.M. Hol, and Z. Gurdal. Design of variable-stiffness concial shells for maximum fundamental eigenfrequency. *Computer and Structures*, 86:870–878, 2008.

[52] A.W. Blom, Z. Gurdal, and P.B. Stickler. Optimization of a composite cylinder under bending by tailoring stiffness properties in circumferential direction. *Composites: Part B*, 41:157–165, 2010.

[53] A. Alhajahmad, M.M. Abdalla, and Z. Gurdal. Design tailoring for pressure pillowing using tow-placed steered fibers. *Journal of Aircraft*, 45, Issue 2:630–640, 2008.

[54] S.W. Tsai and N.J. Pagano. *Composite Materials Workshop*, chapter Invariant Properties of Composite Materials, pages 233–253. Technomic Publishing Company, Inc., 1968.

[55] K. Svanberg. On local and global minima in structural optimization. *New Directions in Optimum Structural Design*, pages 327–341, 1984.

[56] J.L. Grenestedt and P. Gudmundson. *Layup Optimization of Composite Materials Structures*, pages 311–336. Elsevier Science Ltd., 1993.

[57] S. Setdoodeh, M.M. Abdalla, and Z. Gurdal. Approximate feasible regions for lamination parameters. *American Institute of Aeronautics and Astronautics, Inc.*, 11th Multidisciplinary Analysis and Optimization Conference, 2006.

[58] S. Setdoodeh, M.M. Abdalla, and Z. Gurdal. Design of variable-stiffness laminates using lamination parameters. *Composites Part B: Engineering*, 37, Issues 4,5:301–309, 2006.

[59] M.M. Abdalla, S. Setoodeh, and Z. Gurdal. Design of variable stiffness composite panels for maximum fundamental frequency using lamination parameters. *Composite Structures*, 21:283–291, 2007.

[60] S.T. IJsselmuiden, S. Setdoodeh, M.M. Abdalla, and Z. Gurdal. Design of variable-stiffness panels for maximum buckling load using lamination parameters. *Composites Part B: Engineering*, 49th Structures, Structural Dynamics and Materials Conference, 2008.

[61] K. Svanberg. A class of globally convergent optimization methods based on conservative convex separable approximations. *SIAM Journal of Optimization*, 12, Issue 2:555–573, 2002.

[62] S.T. IJsselmuiden, M.M. Abdalla, and Z. Gurdal. Implementation of strength-based failure criteria in the lamination parameter design space. *American Institute of Aeronautics and Astronautics, Inc.*, 46, Issue 7:1826–1834, 2008.

[63] S.T. IJsselmuiden, M.M. Abdalla, and Z. Gurdal. Maximising buckling loads of variable stiffness shells using lamination parameters. *American Institute of Aeronautics and Astronautics, Inc.*, 50th Structures, Structural Dynamics and Materials Conference, 2009.

[64] S.T. IJsselmuiden, M.M. Abdalla, and Z. Gurdal. Optimization of variable-stiffness panels for maximum buckling load using lamination parameters. *American Institute of Aeronautics and Astronautics, Inc.*, 48, Issue 1:134–143, 2010.

[65] V.B. Hammer, M.P. Bendsoe, R. Lipton, and P. Pedersen. Parametrization in laminate design for optimal compliance. *International Journal of Solids and Structures*, 34, Issue 4:415–434, 1997.

[66] A. Khani, S.T. IJsselmuiden, M.M. Abdalla, and Z. Gurdal. Design of variable stiffnees panels for maximum strength using lamination parameters. *Composites Part B: Engineering*, 42, Issue 3:546–552, 2011.

[67] A. Khani, M.M. Abdalla, and Z. Gurdal. Circumferential stiffness tailoring of general cross section cylinders for maximum buckling load with strength constraints. *Composite Structures*, 94:2851–2860, 2012.

[68] A. Khani, M.M. Abdalla, and Z. Gurdal. Optimum tailoring of fibre-steered longitudinally stiffend cylinders. *Composite Structures*, 122:343–351, 2015.

[69] D.M.J. Peeters and M.M. Abdalla. Structural approximations for composite optimisation. *11th World Congress on Structural and Multidisciplinary Optimization - Sydney Australia*, 2015.

[70] D.M.J. Peeters, S. Hesse, and M.M. Abdalla. Stacking sequence optimisation of variable stiffness laminates with manufacturing constraints. *Composite Structures*, 125:596–604, 2015.

[71] S. Setdoodeh, S.T. IJsselmuiden, M.M. Abdalla, and Z. Gurdal. Design of variable-stiffness panels for maximum buckling load. *Composites Structures*, 87:109–117, 2009.

[72] D.M.J. Peeter, D. van Baalen, and M.M. Abdalla. Combining topology and lamination parameter optimization. *Structural Multidisciplinary Optimization*, 52:105–120, 2015.

[73] F.X. Irisarri, D.M.J. Peeters, and M.M. Abdalla. Optimization of ply drop in variable stiffened laminates. *Composite Structures*, 2016.

[74] D.M.J. Peeters and M.M. Abdalla. Optimization of ply drop locations in variable thickness composites. *American Institute of Aeronautics and Astronautics Journal*, 5:1760–1768, 2016.

[75] D.M.J. Peeters and M.M. Abdalla. Design guidelines in nonconventional composite laminate optimization. *Journal of Aircraft*, 2016.

[76] S.W. Tsai and H.T. Hahn. *Introduction to Composite Materials*. Technomic Publishing Company, Inc., 1st edition, 1980.

[77] D.M.J. Peeters. *Design Optimisation of Practial Variable Stiffness and Thickness Laminates*. PhD thesis, Delft University of Technology, 2016.

[78] W.C. Cui, M.R. Wisnom, and M. Jones. A comparison of failure criteria to predict delamination of unidirectional glass/epoxy specimens waisted through the thickness. *Composites Part A: Applied Science and Manufacturing*, Vol. 23:158–166, 1991.

[79] S.W. Tsai and E.M. Wu. A general theory of strength for anisotropic materials. *Journal of Composite Materials*, Vol. 5:58–80, 1971.

[80] Z. Gurdal, R.T. Haftka, and P. Hajela. *Design and optimization of Laminated composite materials*. John Wiley and Sons, Inc., 1999.

[81] G.H. Staab. *Laminar Composites*. Elsevier Inc., 2nd edition, 2015.

[82] A. Felippa. Recent advances in finite element templates. *Technical Report CAS-00-14, University of Colorado*, 2000.

[83] A. Felippa. A study of optimal membrane triangles with drilling freedoms. *Computer methods in applied mechanics and engineering*, 192:2125–2168, 2003.

[84] C. Militello and A. Felippa. The first andes elements: 9-dof plate bending triangles. *Computer methods in applied mechanics and engineering*, 93, Issue 2:217–246, 1991.

[85] R.T. Haftka and Z. Gurdal. *Solid Mechanics and its Applications - Elements of Structural Optimization*. Kluwer Acadamic Publishers, 3d edition, 1992.

[86] H. Chickermane and H.C. Gea. Structural optimization using a new local approximation method. *International Journal for Numerical Methods in Engineering*, 3:829–846, 1996.

[87] U. Kirsch. *Design-Oriented Analysis of Structures: A Unified Approach.* Kluwer Academic Publishers, 3d edition, 2014.

[88] N. Olhoff. Multicriterion structural optimization via bound formulation and mathematical programming. *Structural Optimization*, 1:11–17, 1989.

[89] C.G. Diaconu, H. Sekine, and M. Sato. Buckling characteristics and layup optimization of long laminated composite cylindrical shells subjected to combined loads using lamination parameters. *Composite Structures*, 58:423–433, 2002.

[90] M. Sato and H. Sekine. Vibration characteristics and layup design of cfrp laminates with embedded shape memory alloy fibers. *13th International Conference on Composite Materials - Beijing China*, 2001.

[91] S. Setdoodeh and A.W. Blom. Generating curvilinear fiber paths from lamination parameter distribution. *47th Structures, Structural Dynamics and Matericals Conference - Newport Rhode Island*, pages 109–117, 2006.

[92] A. Todoroki and R. Haftka. Lamination parameters for efficient genetic optimization of the stacking sequences of composite panels. *American Institute of Aeronautics and Astronautics, Inc.*, Symposium on Multidisciplinary Analysis and Optimization. Reston, VA.:870–879, 1998.

[93] M. Autio. Determining the real lay-up of a laminate corresponding to optimal lamination parameter by genetic search. *Structural Multidisciplinary Optimization*, 20:301–310, 2000.

[94] J.M.J.F. van Campen, C. Kassapoglou, and Z. Gurdal. Design of fiber-steered variable-stiffness laminates based on a given lamination parameter distribution. *52nd Structures, Structural Dynamics and Materials Conference - Denver Colorado*, 2011.

[95] J.M.J.F. van Campen, C. Kassapoglou, and Z. Gurdal. Generating realistic laminate fiber angle distribuitons for optimal variable stiffness laminates. *Composite Part B: Engineering*, pages 354–360, 2012.

[96] F.X. Irisarri, M.M. Abdalla, and Z. Gurdal. Improved shepard's method for the optimization of composite structures. *American Institute of Aeronautics and Astronautics, Inc.*, 49, Issue 12, 2011.

[97] A.W. Blom, M.M. Abdalla, and Z. Gurdal. Optimization of course locations in fiber-placed panels for general fiber angle distributions. *Composites Science and Technology*, 70:564–570, 2010.

[98] A. Groenwold and R.T. Haftka. Optimization with non-homogeneous failure criteria like tsai-wu for composite laminates. *Structural Multidisciplinary Optimization*, 32:183–190, 2006.

[99] M.M. Abdalla, Z. Gurdal, and F. Abdelal. Thermomechanical response of variable stiffness composite panels. *Journal of Thermal Stresses*, 32, Issue 2:187–208, 2008.

[100] S.T. IJsselmuiden, M.M. Abdalla, Z. Gurdal, and F. Abdelal. Thermomechanical design optimization of variable stiffness composite panels for buckling. *Journal of Thermal Stresses*, 33, Issue 10:1977–992, 2010.

[101] R.M. Jones. Buckling of circular cylindrical shells with multiple orthotropic layers and eccentric stiffeners. *American Institute of Aeronautics and Astronautics, Inc.*, 6, No. 12:2301–2305, 1968.

[102] M. Miki. Material design of composite laminates with required in-plane elastic properties. *Progress in Science and Engineering of Composites - ICCM IV*, 1:1725–1731, 1982.

[103] M. Miki. Design of laminated fibrous composite plates with required flexural stiffness. *Recent Advances in Composites in the United States and Japan*, 864:387–400, 1985.

[104] H. Fukunaga. Netting theory and its application to optimum design of laminated composite shells and plates. *American Institute of Aeronautics and Astronautics, Inc.*, 29th Structures, Structural Dynamics and Materials Conference:983–991, 1988.

[105] H. Fukunaga and H. Sekine. Stiffness design method of symmetric laminates using lamination parameters. *American Institute of Aeronautics and Astronautics, Inc.*, 30, Issue 11:2791–2793, 1992.

[106] H. Fukunaga, H. Sekine, and M. Sato. Optimal design of symmetric laminated plates for fundamental frequency. *Journal of Sound and Vibration*, 171, Issue 2:219–229, 1994.

[107] C.G. Diaconu, H. Sekine, and M. Sato. Feasible region in general design space of lamination parameters for laminated composites. *American Institute of Aeronautics and Astronautics, Inc.*, 40, Issue 3:559–565, 2002.

[108] C.G. Diaconu, H. Sekine, and M. Sato. Layup optimization of symmetrically laminated thick plates for fundamental frequencies using lamination parameters. *Structural and Multidisciplinary Optimization*, 24, Issue 4:302–311, 2002.

[109] C.G. Diaconu. Layup optimization for buckling of laminated composite shells with restricted layer angles. *American Institute of Aeronautics and Astronautics, Inc.*, 42, Issue 10:2153–2163, 2004.

[110] M.W. Bloomfield, C.G. Diaconu, and P.M. Weaver. On feasible regions of lamination parameters for lay-up optimization of laminated composites. *International Journal of Solids and Structures*, 465, Issue 2104:1123 – 1143, 2009.

A

Feasible Design Region of LP

In this Appendix the feasible design region of lamination parameters is discussed. Lamination parameters are interdependent since they are based on the same variation of ply orientation through the thickness. Although for every lamination parameter $V_i^{A,B,D} \in [-1,1]$ holds this explains why the design domain is not simply given by the full unit cube $[-1,1]^{12}$ in $\mathbb{R}^{12}$ [65]. There exist a feasible design region where values of lamination parameters are limited by others. For the general case with 12 lamination parameters this feasible region is still unknown and has yet to be determined. Although this feasible region is unknown, Grenestedt and Gudmundson were able to prove that the feasible design region for the 12 lamination parameters in $\mathbb{R}^{12}$ is convex [56]. The feasible region for different types of laminates will be discussed.

A.1. Orthotropic Laminates

Fortunately it is possible to reduce the amount of lamination parameters as design variables. Besides some special applications laminate extension-bending coupling is undesirable [6]. This coupling can be avoided by applying symmetry conditions on the stacking sequence. For symmetric laminates it is known that the B-matrix is zero and therefore parameters V_i^B become known and equal to zero. Balanced conditions preclude extension-shear coupling and put lamination parameters $V_{2,4}^A$ to zero. Miki was the first to establish the feasible region for orthotropic laminates separately for in-plane stiffness in $\mathbb{R}^2$ [102]. The convex hull H representing the feasible design region is described by Equation A.1. The feasible region is typically presented by Miki's diagram illustrate in Figure A.1 for $V_{1,3}^A$. Although parameters $V_{2,4}^D$ are not zero for orthotropic laminates it is known that these values are close to zero if the laminate is configured of many plies. Therefore the convex hull relation given by Equation A.1 is useful for thick laminates and is assumed to hold for pure flexural loads [103].

A coupled design region in $\mathbb{R}^4$ for both in-plane and flexural behavior was first approximated by Fukunaga to obtain the optimum configuration for buckling and vibration [104]. Later Gredestedt and Gudmunson used a variational approach to show that this approximation resulted in a region too small and implicitly determined the true feasible design space for $V_{1,3}^{A,D}$ [56].

$$H = \left\{ V_{1,3}^j \in \mathbb{R}^2 \;\middle|\; \begin{array}{c} V_3^j \geq 2\left(V_1^j\right)^2 - 1 \\ -1 \leq V_{1,3}^j \leq 1 \end{array} \right\} \quad \text{for} \quad j = A, D \tag{A.1}$$

From Miki's diagram physical meaning of the laminate can be derived. The boundary parabola represents uni-directional laminates of ±θ, represented in Figure A.1 (left) by points B, C, D, E and F for 0^o, $\pm 30^o$, $\pm 45^o$, $\pm 60^o$ and 90^o respectively. Midpoint A represents a quasi-isotropic laminates since all lamination parameters equal zero. If a certain design point is known a straight line can be drawn through this point that intersects the boundary of the feasible region at two points. For design point A this results in line BE. The ply orientations corresponding to the two boundary points can be used to compose a stacking sequence that represents the stiffness of the design point. The ratio of fiber orientations corresponding to points B and E are equal to the inverse ratio of the lengths of line segments AB and AE. For example point A can be represented by applying twice as many ±60 degree plies as 0 plies. The thinnest possible symmetric stack becomes $[-60/60/0]_s$, which

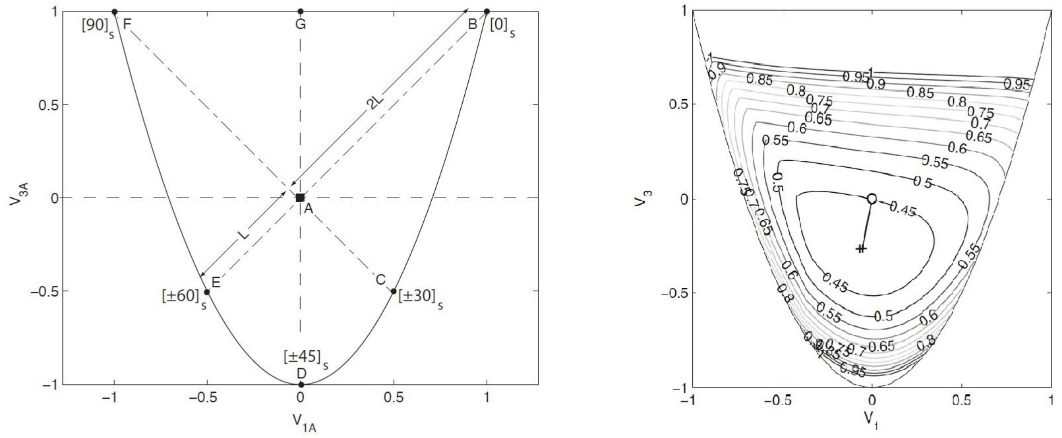

Figure A.1: Left: The feasible design region for in-plane design is given by the enclosed area of line BCDEFB. The parabola represents laminates with ±θ uni-directional laminates. From IJsselmuiden (2011) [18]. Right: The feasible design region for in-plane design with iso-lines respresenting the corresponding square-root of the failure index for compression/shear load. From IJsselmuiden *et al* (2008) [62].

is indeed quasi-isotropic. Similarly point G consist of a laminate with equal number of 0 and 90 degree fiber orientation. Alternatively point A can now be represented by equal contribution of points D and G which is a $[\pm45/0/90]_s$ degree laminate resulting in the conventional quasi-isotropic laminate.

Since the line intersecting the parabola can be drawn in infinite many ways there is not a unique stacking sequence corresponding to a design point represented in the lamination parameter domain. An inverse optimization problem arises and constraints on the maximum thickness and variation of fiber orientation within the plies and between consequetive plies can be introduced [65]. The retrieval of the stacking sequence is further discussed in section 4.2.

Miki's diagram is also useful to show the convexity of the objective function of global structural responses related to the in-plane and flexural stiffness. Many responses are proven to behave convex in the feasible design space. E.g. IJsselmuiden *et al* showed that the square root of the failure index used for strength optimization behaves conves, this is ilustrated with iso-lines in Figure A.1 (right) [62].

A.2. Symmetric Laminates

For symmetric laminates there are four lamination parameters V_i^A to describe the in-plane stiffness and four lamination parameters V_i^D to describe the flexural stiffness of the laminate. Fukunaga and Sekine were able to extend Miki's diagram and derived the feasibe design domain for the pure membrane and bending case separately in $\mathbb{R}^4$ [105]. Reformulated by Hammer *et al* the convex hull representing the feasible design region of these four parameters is determined by Equation A.2 where the equations holds for either pure membrane (V_i^A) or pure flexural (V_i^D) loads [65]. This is illustrated in Figure A.2 for specific points $P_{1,2,3}$ in the $V_{1,3}^D$ plane. Based on the chosen point the dependent feasible region in the $V_{2,4}^D$ plane can be determined.

$$H = \left\{ V_{1,2,3,4}^j \in \mathbb{R}^4 \;\middle|\; \begin{array}{r} 2\left(V_1^j\right)^2\left(1-V_3^j\right)+2\left(V_2^j\right)^2\left(1+V_3^j\right)+\left(V_3^j\right)^2+\left(V_4^j\right)^2-4V_1^jV_2^jV_4^j \leq 1 \\ \left(V_1^j\right)^2+\left(V_2^j\right)^2 \leq 1 \\ -1 \leq V_{1,2,3,4}^j \leq 1 \end{array} \right\} \quad \text{for} \quad j = A, D \tag{A.2}$$

A.3. Other Relations

Although there is not an explicit expression for the feasible design region of the 12 lamination parameters other relations are derived other than the special cases of orthotropic and symmetric laminates. Diaconu *et al* implicitly determined the feasible design region for the 12 lamination parameters by generalizing the variational approach used by Grenestedt and Gudmunson [107]. In a follow up study they showed the importance to gain knowledge of the feasible design region of the 12 lamination parameters [89]. Optimizing for

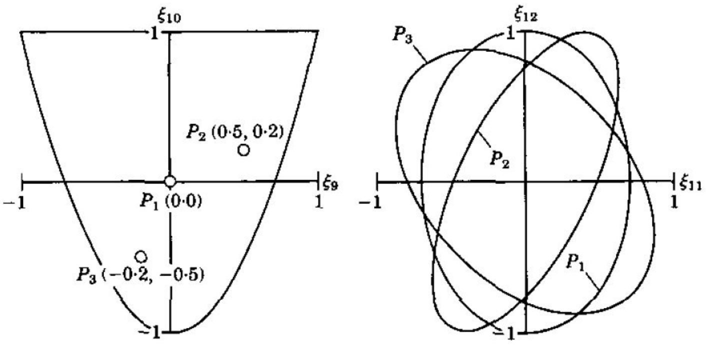

Figure A.2: Miki's Diagram of the V_1^D-V_3^D plane where points p_1 to p_3 are defined (left). These points determine the feasible region of the V_2^D-V_4^D plane (right). From Fukunaga *et al* (1994) [106]

combined compressive axial and torsional loads resulted in an unbalanced asymmetric laminate which can only be obtained in the design space given by all lamination parameters. During this study they were able to derive a new explicit expression to relate $V_i^{A,B,D}$, given by Equation A.3. In another study they optimized a thick symmetric laminature for fundamental frequency including transverse shear [108]. The same variational approach was used to implicitly obtain the true convex hull of orthotropic laminates given by the six lamination parameters $V_{1,3}^A$ and $V_{1,2,3,4}^D$.

$$H = \left\{ V_i^{A,B,D} \in \mathbb{R}^3 \;\middle|\; \begin{array}{r} 4\left(V_i^A+1\right)\left(V_i^D+1\right) \geq \left(V_i^A+1\right)^4 + 3\left(V_i^B\right)^2 \\ 4\left(V_i^A-1\right)\left(V_i^D-1\right) \geq \left(V_i^A-1\right)^4 + 3\left(V_i^B\right)^2 \\ -1 \leq V_i^{A,B,D} \leq 1 \end{array} \right\} \quad \text{for} \quad i = 1,2,3,4 \tag{A.3}$$

Although deriving an implicit method to obtain the feasible design region of any set of lamination parameters Diaconu and Sekine performed a follow up study to research explicit relations since the implicit method is labor intensive and therefore unpractical [109]. Allowing the orientations to vary over 0, ±45 and 90 degrees only nine parameters are required since $V_4^{A,B,D} = 0$. They were able to derive explicit relations for the corresponding feasible design region. Bloomfield *et al* extended this work with a method to obtain the feasible design region for any finite set of orientation angles [110]. They showed that the nature of the feasible design region of all lamination parameters is the interlinking of three interdependent convex subspaces given by V_i^A, V_i^B and V_i^D. The interlinking is based on the linear, quadratic and cubic ply orientation volume fractions.

Setoodeh *et al* introduced another method to approximate the feasible design region [57]. For a variation of layups the corresponding lamination parameters are calculated. Based on these lamination parameters the convex hull is determined. New layups are added until the volume of the convex hull converges. Thereafter 12 linear equations for the 12 lamination parameters were assumed to completely describe the approximated convex hull.

B

Tsai-Wu Failure Envelope

In this Appendix the Tsai-Wu failure envelope in stress and strain space is given. The Tsai-Wu formula is probably the best known failure criterion and has acceptable predictions compared with test results, except for biaxial compression [6]. For 2-dimensional planer stress state the failure index is given by:

$$f = F_{11}\sigma_1^2 + F_{22}\sigma_2^2 + F_{66}\tau_{12}^2 + F_1\sigma_1 + F_2\sigma_2 + 2F_{12}\sigma_1\sigma_2 \tag{B.1}$$

Strength values X_t, X_c, Y_t, Y_t and S are extracted from uni-axial material tests and are given in the material ply axes. Subscript t stands for tension and c for compression coupon tests. The strength values are used to determine the F-values:

$$F_1 = \frac{1}{X_t} - \frac{1}{X_c} \tag{B.2}$$

$$F_2 = \frac{1}{Y_t} - \frac{1}{Y_c} \tag{B.3}$$

$$F_{11} = \frac{1}{X_t X_c} \tag{B.4}$$

$$F_{22} = \frac{1}{Y_t Y_c} \tag{B.5}$$

$$F_{12} = \frac{-1}{2\sqrt{X_t X_c Y_t Y_c}} \tag{B.6}$$

$$F_{66} = \frac{1}{S^2} \tag{B.7}$$

This criteria was first introduced by Tsai and Wu in 1971 and is more of a curve fit rather than a physics based theory [6, 79]. The failure index is useful to assess first ply failure. First ply failure is predicted to occur within a laminate if the following relation is violated:

$$f \leq 1 \tag{B.8}$$

B.1. Lamination Parameters

To address first ply failure the stress state of the individual plies are required, which are based on the fiber orientations. Lamination parameters represent the integrated laminate properties over the thickness. Assessing failure criteria is not straight forward since orientations are unknown. It would be inefficient to apply failure criteria after retrieval of the orientations. Therefore IJsselmuiden *et al* proposed to apply a conservative Tsai-Wu failure envelope in strain space [62]. Using the constitutive relation $\sigma = Q\epsilon$ the Tsai-Wu criterion given by Equation B.9 can be expressed in strain space, given by Equation B.10. Note that the equations are expressed in the material coordinate axes.

$$F_{11}\sigma_1^2 + F_{22}\sigma_2^2 + F_{66}\tau_{12}^2 + F_1\sigma_1 + F_2\sigma_2 + 2F_{12}\sigma_1\sigma_2 \geq 1 \tag{B.9}$$

$$G_{11}\epsilon_1^2 + G_{22}\epsilon_2^2 + G_{66}\epsilon_{12}^2 + G_1\epsilon_1 + G_2\epsilon_2 + 2G_{12}\epsilon_1\epsilon_2 \geq 1 \tag{B.10}$$

in which,

$$\begin{aligned}
G_{11} &= Q_{11}^2 F_{11} + Q_{12}^2 F_{22} + 2F_{12} Q_{11} Q_{12} & \qquad G_1 &= Q_{11} F_1 + Q_{12} F_2 \\
G_{22} &= Q_{12}^2 F_{11} + Q_{22}^2 F_{22} + 2F_{12} Q_{12} Q_{22} & \qquad G_2 &= Q_{12} F_1 + Q_{22} F_2 \\
G_{12} &= Q_{11} Q_{12} F_{11} + Q_{12} Q_{22} F_{22} + F_{12} Q_{12}^2 + F_{12} Q_{11} Q_{22} & & \\
G_{66} &= 4Q_{66}^2 F_{66} & &
\end{aligned} \tag{B.11}$$

Equation B.10 still depends on the stacking sequence, therefore it cannot be used in conjunction with lamination parameters optimization. However, it is possible to determine a region in strain space that is safe regardless of the stacking sequence. The boundary of this conservative region in strain space is given by the failure envelope and every point that lays within the enclosed area will fulfill the Tsai-Wu failure criteria. This envelope is derived by IJsselmuiden *et al* and later simplified by the same authors [62, 66]. For the simplified derivation the Tsai Wu strain space is given in three strain invariants:

$$I_1 = \epsilon_I + \epsilon_{II} \tag{B.12}$$

$$I_2 = \epsilon_I^2 + \epsilon_{II}^2 \tag{B.13}$$

$$I_4 = \epsilon_I n_1^2 + \epsilon_{II} n_2^2 \tag{B.14}$$

in which $n_1 = \cos\theta$, $n_2 = \sin\theta$ and $\epsilon_{I,II}$ are the principal strains. The failure criteria is now given by:

$$f = \frac{1}{2} u_1 I_1^2 + u_2 I_1 I_4 + \frac{1}{2} u_3 I_4^2 + u_4 I_2 + u_5 I_1 + u_6 I_4 \tag{B.15}$$

where u_1 to u_6 can be obtained by comparing the Tsai-Wu equation in strain space with the three strain invariants:

$$\begin{aligned}
u_1 &= G_{22} - \tfrac{G_{66}}{2} & \qquad u_4 &= G_{11} - 2G_{12} + G_{22} - G_{66} \\
u_2 &= \tfrac{G_{66}}{2} & \qquad u_5 &= G_2 \\
u_3 &= 2G_{12} - 2\left(G_{22} - \tfrac{G_{66}}{2}\right) & \qquad u_6 &= G_1 - G_2
\end{aligned} \tag{B.16}$$

The failure envelope is given by the most critical fiber angle where the failure criteria equals one. Since only the strain invariant I_4 is a function of θ this can be expressed as:

$$\max_{\theta} f = 1 \tag{B.17}$$

$$\max_{I_4} f = 1,\ \epsilon_{II} \leq I_4 \leq \epsilon_I \tag{B.18}$$

There are two possible envelopes, the first is one smooth envelope described by quadratic conditions on strains. The second is a non smooth self intersecting envelope by quartic conditions on strains which can be resolved into two quadratic envelopes. In both cases the conservative failure envelope becomes an elliptical form described by Equation B.19,

$$C_{ij} \epsilon_i \epsilon_j + C_i \epsilon_i + C_0 = 0,\ i = I, II \tag{B.19}$$

where for quadratic conditions on strain the failure envelope is described by one ellipse,

$$\begin{aligned}
C_0 &= -\tfrac{1}{4} \tfrac{u_6^2}{u_4} - 1 & \qquad C_{I,I} &= -\tfrac{1}{4} \tfrac{u_3^2}{u_4} + u_2 + u_1 \\
C_I &= -\tfrac{1}{2} \tfrac{u_3 u_6}{u_4} + u_5 & \qquad C_{I,II} &= u_1 - \tfrac{1}{4} \tfrac{u_3^2}{u_4} \\
C_{II} &= -\tfrac{1}{2} \tfrac{u_3 u_6}{u_4} + u_5 & \qquad C_{II,II} &= -\tfrac{1}{4} \tfrac{u_3^2}{u_4} + u2 + u_1
\end{aligned} \tag{B.20}$$

and for quartic conditions on strain the failure envelope is described by two intersecting ellipses,

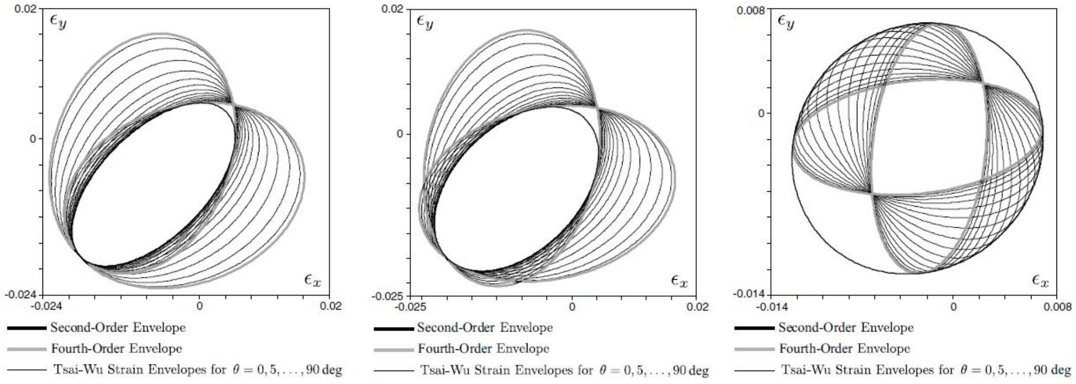

a) Carbon - PEEK(AS4) **b) Carbon - Epoxy(IM6)** **c) Boron - Epoxy(B5.6)**

Figure B.1: Failure envelope for three different materials for $\varepsilon_{xy} = 0$. From IJsselmuiden *et al* (2008) [62]

$$\begin{array}{llllll} C_0\,(1) & = C_0\,(2) & = -1 & C_{I,I}\,(1) & = C_{II,II}\,(2) & = u_2 + u_1 \\ C_I\,(1) & = C_{II}\,(2) & = u_5 & C_{I,II}\,(1) & = C_{I,II}\,(2) & = \frac{1}{2} u_3 + u_1 \\ C_{II}\,(1) & = C_I\,(2) & = u_6 + u_5 & C_{II,II}\,(1) & = C_{II}\,(2) & = u_1 + u_2 + u_3 + u_4 \end{array} \tag{B.21}$$

Note that it is material dependent whether there will be a second or fourth order failure envelope. This is illustrated by IJsselmuiden *et al* in Figure B.1 where the failure envelopes are given for three different materials. For materials presented in figures *a* and *b* the failure envelope is given by quadratic conditions. For the material presented in figure *c* the failure envelop is given by quartic conditions and is the enclosed area by two intersecting ellipses.

C

Sensitivity Analysis

In this Appendix the sensitivities are given for the response approximations given in chapter 4. The first section derives the sensitivities for compliance, the second section for strength and the last section for buckling.

C.1. Compliance Sensitivities

The sensitivities for compliance are derived by IJsselmuiden *et al* [64]. The derivation is reproduced here, and starts from the compliance formulation based on linear finite element analysis:

$$C = \frac{1}{2}\mathbf{F}^t \cdot \mathbf{u} \tag{C.1}$$

Assuming the external mechanical load to be constant the derivative of the compliance equation with respect to an arbitrary parameter b is:

$$\frac{dC}{db} = \frac{1}{2}\mathbf{F}^t \cdot \frac{d\mathbf{u}}{db} \tag{C.2}$$

Taking the derivative of the linear finite element problem:

$$\frac{d\mathbf{K}_m}{db} \cdot \mathbf{u} + \mathbf{K}_m \cdot \frac{d\mathbf{u}}{db} = 0 \quad \rightarrow \quad \frac{d\mathbf{u}}{db} = -\mathbf{K}_m^{-1} \cdot \frac{d\mathbf{K}_m}{db} \cdot \mathbf{u} \tag{C.3}$$

Therefore the derivative of the compliance equation can be written as:

$$\frac{dC}{db} = -\frac{1}{2}\mathbf{F}^t \cdot \mathbf{K}_m^{-1} \cdot \frac{d\mathbf{K}_m}{db} \cdot \mathbf{u} \quad \rightarrow \quad \frac{dC}{db} = -\frac{1}{2}\mathbf{u}^t \cdot \frac{d\mathbf{K}_m}{db} \cdot \mathbf{u} \tag{C.4}$$

Now using the following relation:

$$\frac{\partial f}{\partial \mathbf{A}^{-1}} = -\mathbf{A} \cdot \frac{\partial f}{\partial \mathbf{A}} \cdot \mathbf{A} \tag{C.5}$$

From $C = \frac{1}{2}\mathbf{N}^t\mathbf{A}^{-1}\mathbf{N}$ it is known that compliance depends on $\mathbf{A}^{-1}$. This results in the following sensitivities for element e to be implemented in the compliance response approximation:

$$\phi^{m,e}_{\alpha\beta} = \frac{\partial C}{\partial A^{-1}_{\alpha\beta}} = \frac{1}{2}\sum_{\sigma\rho}^{N} A_{\beta\sigma} A_{\rho\alpha} \left(\mathbf{u}_e^t \cdot \frac{d\mathbf{K}_{m,e}}{dA_{\rho\sigma}} \cdot \mathbf{u}_e\right) \tag{C.6}$$

$$\phi^{b,e}_{\alpha\beta} = \frac{\partial C}{\partial D^{-1}_{\alpha\beta}} = \frac{1}{2}\sum_{\sigma\rho}^{N} D_{\beta\sigma} D_{\rho\alpha} \left(\mathbf{u}_e^t \cdot \frac{d\mathbf{K}_{m,e}}{dD_{\rho\sigma}} \cdot \mathbf{u}_e\right) \tag{C.7}$$

C.2. Strength Sensitivities

In this section the sensitivities for the strength response are derived. The strength formulation is given by [62, 66]:

$$r = \boldsymbol{\varepsilon}^t \cdot \mathbf{g} \tag{C.8}$$

Taking the derivative of the strength equation with respect to an arbitrary parameter b yields:

$$\frac{dr}{db} = \underbrace{\mathbf{N}^t \cdot \frac{d\mathbf{A}^{-1}}{db} \cdot \mathbf{g}}_{T_{\text{local}}} + \underbrace{\frac{d\mathbf{N}^t}{db} \cdot \mathbf{A}^{-1} \cdot \mathbf{g}}_{T_{\text{global}}} \tag{C.9}$$

Local Term:
The local term assumes constant stress resultants and can be evaluated at element level by:

$$T_{\text{local}} = \mathbf{N}^t \cdot \frac{d\mathbf{A}^{-1}}{db} \cdot \mathbf{g} = \mathbf{N}_i^t \cdot \frac{d\mathbf{A}_i^{-1}}{db} \cdot \mathbf{g}_i \tag{C.10}$$

Global Term:
The global term takes the load redistribution into account. This term is summed over all elements to incorporate the contribution of all elements and is given by:

$$T_{\text{glocal}} = \frac{d\mathbf{N}^t}{db} \cdot \mathbf{A}^{-1} \cdot \mathbf{g} = \sum_e \frac{d\mathbf{N}_e^t}{db} \cdot \mathbf{A}_e^{-1} \cdot \mathbf{g}_e \tag{C.11}$$

The derivative of the stress resultants can be written as:

$$\frac{d\mathbf{N}_e}{db} = \frac{d\mathbf{A}_e}{db} \cdot \boldsymbol{\varepsilon}_e + \mathbf{A}_e \cdot \frac{d\boldsymbol{\varepsilon}_e}{db} = \frac{d\mathbf{A}_e}{db} \cdot \boldsymbol{\varepsilon}_e + \mathbf{A}_e \cdot \bar{\mathbf{B}}_e \cdot \frac{d\mathbf{u}_e}{db} \tag{C.12}$$

The first part of the stress resultant derivative can be evaluated at local element level i. Hence the sum for the first part is dropped. However, the second term depends on the displacement which can change for all elements if the stacking sequence of a single element is updated, therefore the summation over all elements is still required. Using $\mathbf{s}_e = \mathbf{A}_e^{-1} \cdot \mathbf{g}_e$ the global term is given as:

$$T_{\text{glocal}} = \mathbf{s}_i^t \cdot \frac{d\mathbf{A}_i}{db} \cdot \boldsymbol{\varepsilon}_i + \sum_e \mathbf{s}_e^t \cdot \mathbf{A}_e \cdot \bar{\mathbf{B}}_e \cdot \frac{d\mathbf{u}_e}{db} \tag{C.13}$$

Introducing a new term:

$$\mathbf{f}_e = \bar{\mathbf{B}}_e^t \cdot \mathbf{A}_e \cdot \mathbf{s}_e \tag{C.14}$$

Now the global term is written as:

$$T_{\text{glocal}} = \mathbf{s}_i^t \cdot \frac{d\mathbf{A}_i}{db} \cdot \boldsymbol{\varepsilon}_i + \sum_e \mathbf{f}_e \cdot \frac{d\mathbf{u}_e}{db} \tag{C.15}$$

Joint-Displacement vector:
To determine the derivative of the displacement vector the adjoint displacement vector $\mathbf{v}$ is introduced by solving the following linear force-displacement relation:

$$\mathbf{K}_m \cdot \mathbf{v} = \mathbf{f} \tag{C.16}$$

Taking the derivative of the linear finite element problem yields:

$$\frac{d\mathbf{K}_m}{db}\cdot\mathbf{u}+\mathbf{K}_m\cdot\frac{d\mathbf{u}}{db}=0 \quad\rightarrow\quad \mathbf{K}_m\cdot\frac{d\mathbf{u}}{db}=-\frac{d\mathbf{K}_m}{db}\cdot\mathbf{u} \tag{C.17}$$

Multiplying both sides by the adjoint displacment vector **v** results in:

$$\mathbf{v}^t\cdot\mathbf{K}_m\cdot\frac{d\mathbf{u}}{db}=-\mathbf{v}^t\cdot\frac{d\mathbf{K}_m}{db}\cdot\mathbf{u} \quad\rightarrow\quad \mathbf{f}\cdot\frac{d\mathbf{u}}{db}=-\mathbf{v}^t\cdot\frac{d\mathbf{K}_m}{db}\cdot\mathbf{u} \tag{C.18}$$

This term can also be evaluated at the ith local element level, since all global redistribution of load is embedded in the adjoint displacement vector **v**. Therefore the sum in the global term is dropped and the global term is written as:

$$T_{\text{glocal}}=\mathbf{s}_i^t\cdot\frac{d\mathbf{A}_i}{db}\cdot\boldsymbol{\varepsilon}_i-\mathbf{v}_i^t\cdot\frac{d\mathbf{K}_{m,i}}{db}\cdot\mathbf{u}_i \tag{C.19}$$

Total Derivative:
Combining the local and global terms the total derivative is given by:

$$\frac{dr}{db}=\underbrace{\mathbf{N}_i^t\cdot\frac{d\mathbf{A}_i^{-1}}{db}\cdot\mathbf{g}_i}_{T_{\text{local}}}+\underbrace{\mathbf{s}_i^t\cdot\frac{d\mathbf{A}_i}{db}\cdot\boldsymbol{\varepsilon}_i-\mathbf{v}_i^t\cdot\frac{d\mathbf{K}_{m,i}}{db}\cdot\mathbf{u}_i}_{T_{\text{glocal}}} \tag{C.20}$$

The local term depends on $\mathbf{A}^{-1}$ and the global term on **A**. Therefore the sensitivities for element e is given by:

$$\phi^{m,e}_{\alpha\beta}=\frac{\partial r}{\partial A^{-1}_{\alpha\beta}}=\sum_{\sigma\rho}^{N}\mathbf{N}_e^t\cdot\frac{d\mathbf{A}_e^{-1}}{dA_{\rho\sigma}}\cdot\mathbf{g}_e \tag{C.21}$$

$$\psi^{m,e}_{\alpha\beta}=\frac{\partial r}{\partial A_{\alpha\beta}}=\sum_{\sigma\rho}^{N}\left(\mathbf{s}_e^t\cdot\frac{d\mathbf{A}_e}{dA_{\rho\sigma}}\cdot\boldsymbol{\varepsilon}_e-\mathbf{v}_e^t\cdot\frac{d\mathbf{K}_{m,e}}{dA_{\rho\sigma}}\cdot\mathbf{u}_e\right) \tag{C.22}$$

C.3. Buckling Sensitivities

The sensitivities for buckling are derived by IJsselmuiden *et al* [63, 64]. The buckling equation is given as:

$$\left(\mathbf{K}_m-\lambda\mathbf{K}_g\right)\cdot\mathbf{a}=0 \tag{C.23}$$

Taking the derivative to an arbitrary variable b of the buckling equation yields:

$$\left(\frac{d\mathbf{K}_m}{db}-\frac{d\lambda}{db}\mathbf{K}_g-\lambda\frac{d\mathbf{K}_g}{db}\right)\cdot\mathbf{a}+\left(\mathbf{K}_m-\lambda\mathbf{K}_g\right)\cdot\frac{d\mathbf{a}}{db}=0 \tag{C.24}$$

The second term is zero due to the buckling formulation. Note that the material stiffness is a function of membrane and bending stiffness for shells. Multiply all terms by $-\lambda\mathbf{a}^t$.

$$-\lambda\mathbf{a}^t\cdot\frac{d\mathbf{K}_m}{db}\cdot\mathbf{a}+\lambda\frac{d\lambda}{db}\mathbf{a}^t\cdot\mathbf{K}_g\cdot\mathbf{a}+\lambda^2\mathbf{a}^t\cdot\frac{d\mathbf{K}_g}{db}\cdot\mathbf{a}=0 \tag{C.25}$$

Using the following relation:

$$\mathbf{a}^t\cdot\left(\mathbf{K}_m-\lambda\mathbf{K}_g\right)\cdot\mathbf{a}=0 \quad\rightarrow\quad \mathbf{a}^t\cdot\mathbf{K}_m\cdot\mathbf{a}=\lambda\mathbf{a}^t\cdot\mathbf{K}_g\cdot\mathbf{a}=1 \tag{C.26}$$

Results in the following derivative for the load multiplier:

$$\frac{d\lambda}{db} = \lambda \mathbf{a}^t \cdot \frac{d\mathbf{K}_m}{db} \cdot \mathbf{a} - \lambda^2 \cdot \mathbf{a}^t \frac{d\mathbf{K}_g}{db} \cdot \mathbf{a} \quad \rightarrow \quad \frac{d\lambda}{db} = \lambda \mathbf{a}^t \cdot \left(\frac{d\mathbf{K}_m}{db} - \lambda \frac{d\mathbf{K}_g}{db} \right) \cdot \mathbf{a} \tag{C.27}$$

Local Term - Material Stiffness
The first term can be evaluated at the local ith element level:

$$T_{\text{local}} = \mathbf{a}^t \cdot \frac{d\mathbf{K}_m}{db} \cdot \mathbf{a} = \mathbf{a}_i^t \cdot \frac{d\mathbf{K}_{m,i}}{db} \cdot \mathbf{a}_i \tag{C.28}$$

Global Term - Geometric Stiffness
The second term has to be evaluated at the global level. If a stacking sequence of an element changes the load distribution throughout the structure changes accordingly. Therefore the geometric stiffness matrix changes on a global level and the derivative of all elements are summed. Using:

$$\mathbf{K}_g = -n_{x,e}\mathbf{K}_x - n_{y,e}\mathbf{K}_y - n_{xy,e}\mathbf{K}_{xy} \qquad \text{and} \qquad \mathbf{s}_e = \left[\mathbf{a}_e^t \cdot \mathbf{K}_x \cdot \mathbf{a}_e; \quad \mathbf{a}_e^t \cdot \mathbf{K}_y \cdot \mathbf{a}_e; \quad \mathbf{a}_e^t \cdot \mathbf{K}_{xy} \cdot \mathbf{a}_e\right]^t \tag{C.29}$$

The global term is written as:

$$T_{\text{global}} = \mathbf{a}^t \frac{d\mathbf{K}_g}{db} \mathbf{a} = -\sum_e \mathbf{s}_e^t \cdot \frac{d\mathbf{N}_e}{db} \tag{C.30}$$

The derivative of the in-plane stress resultant can be written as:

$$\frac{d\mathbf{N}_e}{db} = \frac{d\mathbf{A}_e}{db} \cdot \boldsymbol{\varepsilon}_e + \mathbf{A}_e \cdot \frac{d\boldsymbol{\varepsilon}_e}{db} = \frac{d\mathbf{A}_e}{db} \cdot \boldsymbol{\varepsilon}_e + \mathbf{A}_e \cdot \bar{\mathbf{B}}_e \cdot \frac{d\mathbf{u}_e}{db} \tag{C.31}$$

The first part of this derivative can be evaluated at the local ith element level. However, the second term depends on the displacement which can change for all elements if the stacking sequence of a single element is updated, hence the summations is still required:

$$T_{\text{global}} = -\mathbf{s}_i^t \cdot \frac{d\mathbf{A}_i}{db} \cdot \boldsymbol{\varepsilon}_i - \sum_e \mathbf{s}_e^t \cdot \mathbf{A}_e \cdot \bar{\mathbf{B}}_e \cdot \frac{d\mathbf{u}_e}{db} \tag{C.32}$$

Introducing a new term:

$$\mathbf{f}_e = \bar{\mathbf{B}}_e^t \cdot \mathbf{A}_e \cdot \mathbf{s}_e \tag{C.33}$$

Now the global term is given by:

$$T_{\text{global}} = -\mathbf{s}_i^t \cdot \frac{d\mathbf{A}_i}{db} \cdot \boldsymbol{\varepsilon}_i - \sum_e \mathbf{f}_e^t \cdot \frac{d\mathbf{u}_e}{db} \tag{C.34}$$

Joint-Displacement vector:
To determine the derivative of the displacement vector the adjoint displacement vector **v** is introduced by solving the linear force-displacement equation:

$$\mathbf{K}_m \cdot \mathbf{v} = \mathbf{f} \tag{C.35}$$

Taking the derivative of the linear finite element formulation $K_m \cdot u = F$:

$$\frac{d\mathbf{K}_m}{db} \cdot \mathbf{u} + \mathbf{K}_m \cdot \frac{d\mathbf{u}}{db} = 0 \quad \rightarrow \quad \mathbf{K}_m \cdot \frac{d\mathbf{u}}{db} = -\frac{d\mathbf{K}_m}{db} \cdot \mathbf{u} \tag{C.36}$$

Multiplying both sides by the adjoint displacment vector **v**:

$$\mathbf{v}^t \cdot \mathbf{K}_m \cdot \frac{d\mathbf{u}}{db} = -\mathbf{v}^t \cdot \frac{d\mathbf{K}_m}{db} \cdot \mathbf{u} \quad \rightarrow \quad \mathbf{f} \cdot \frac{d\mathbf{u}}{db} = -\mathbf{v}^t \cdot \frac{d\mathbf{K}_m}{db} \cdot \mathbf{u} \tag{C.37}$$

This term can also be evaluated at the local ith element level, since all global redistribution of load is embedded in the adjoint displacement vector.

$$T_{\text{global}} = -\mathbf{s}_i^t \cdot \frac{d\mathbf{A}_i}{db} \cdot \boldsymbol{\varepsilon}_i + \mathbf{v}_i^t \cdot \frac{d\mathbf{K}_{m,i}}{db} \cdot \mathbf{u}_i \tag{C.38}$$

Total derivative:
Substituting both local and global terms back into the total derivative for the ith element yields:

$$\frac{d\lambda}{db} = \underbrace{\lambda \left(\mathbf{a}_i^t \cdot \frac{d\mathbf{K}_{m,i}}{db} \cdot \mathbf{a}_i \right)}_{\text{material stiffness}} + \underbrace{\lambda^2 \left(\mathbf{s}_i^t \cdot \frac{d\mathbf{A}_i}{db} \cdot \mathbf{e}_i - \mathbf{v}_i^t \cdot \frac{d\mathbf{K}_{m,i}}{db} \cdot \mathbf{u}_i \right)}_{\text{geometric stiffness}} \tag{C.39}$$

The general response formulation is given. The linear terms are based on the geometric stiffness, and the reciprocal terms depend on the material stiffness.

$$r \approx \sum_{i=1}^{N} \underbrace{\boldsymbol{\Psi}_{\boldsymbol{i}}^{\boldsymbol{m}} : \mathbf{A} + \boldsymbol{\Psi}_{\boldsymbol{i}}^{\boldsymbol{b}} : \mathbf{D}}_{\text{geometric stiffness}} + \underbrace{\boldsymbol{\Phi}_{\boldsymbol{i}}^{\boldsymbol{m}} : \mathbf{A}^{-1} + \boldsymbol{\Phi}_{\boldsymbol{i}}^{\boldsymbol{b}} : \mathbf{D}^{-1}}_{\text{material stiffness}} \tag{C.40}$$

Combining the following expressions:

$$\frac{\partial f}{\partial \mathbf{A}} = -\mathbf{A}^{-1} \cdot \frac{\partial f}{\partial \mathbf{A}^{-1}} \cdot \mathbf{A}^{-1} \quad \text{and} \quad \frac{\partial f}{\partial \mathbf{A}^{-1}} = -\mathbf{A} \cdot \frac{\partial f}{\partial \mathbf{A}} \cdot \mathbf{A} \tag{C.41}$$

And using the chain-rule to obtain the actual response derivative:

$$\frac{\partial r}{\partial b} = \frac{\partial r}{\partial \lambda} \frac{\partial \lambda}{\partial b} \quad \rightarrow \quad \frac{\partial r}{\partial b} = -\frac{1}{\lambda^2} \frac{\partial \lambda}{\partial b} \tag{C.42}$$

Results in the following sensitivities for material stiffness at element level e:

$$\phi_{\alpha\beta}^{m,e} = \frac{\partial r}{\partial A_{\alpha\beta}^{-1}} = \frac{1}{\lambda} \sum_{\sigma\rho}^{N} A_{\beta\sigma} A_{\rho\alpha} \left(\mathbf{a}_e^t \cdot \frac{d\mathbf{K}_{m,e}}{dA_{\rho\sigma}} \cdot \mathbf{a}_e \right) \tag{C.43}$$

$$\phi_{\alpha\beta}^{b,e} = \frac{\partial r}{\partial D_{\alpha\beta}^{-1}} = \frac{1}{\lambda} \sum_{\sigma\rho}^{N} D_{\beta\sigma} D_{\rho\alpha} \left(\mathbf{a}_e^t \cdot \frac{d\mathbf{K}_{m,e}}{dD_{\rho\sigma}} \cdot \mathbf{a}_e \right) \tag{C.44}$$

And in the following sensitivities for geometric stiffness at element level e:

$$\psi_{\alpha\beta}^{m,e} = \frac{\partial r}{\partial A_{\alpha\beta}} = \sum_{\sigma\rho}^{N} \left(-\mathbf{s}_e^t \cdot \frac{d\mathbf{A}_e}{dA_{\rho\sigma}} \cdot \boldsymbol{\varepsilon}_e + \mathbf{v}_e^t \cdot \frac{d\mathbf{K}_{m,e}}{dA_{\rho\sigma}} \cdot \mathbf{u}_e \right) \tag{C.45}$$

$$\psi_{\alpha\beta}^{b,e} = \frac{\partial r}{\partial D_{\alpha\beta}} = \sum_{\sigma\rho}^{N} \left(\mathbf{v}_e^t \cdot \frac{d\mathbf{K}_{m,e}}{dD_{\rho\sigma}} \cdot \mathbf{u}_e \right) \tag{C.46}$$